LASER HOLOGRAPHIC FABRICATION OF THREE-DIMENSIONAL PHOTONIC CRYSTAL TEMPLATES USING ADVANCED PHASE MASK TECHNIQUES

by

Di Xu

B.S., Wuhan University, 2001

M.S., Wuhan University, 2004

Submitted to the Graduate Faculty of

The Swanson School of Engineering in partial fulfillment

of the requirements for the degree of

Doctor of Philosophy

University of Pittsburgh

2010

UNIVERSITY OF PITTSBURGH

SWANSON SCHOOL OF ENGINEERING

This dissertation was presented

by

Di Xu

It was defended on

October 29, 2010

and approved by

Joel Falk, PhD, Professor
Department of Electrical and Computer Engineering

Minhee Yun, PhD, Associate Professor
Department of Electrical and Computer Engineering

William Stanchina, PhD, Professor
Department of Electrical and Computer Engineering

Qing-Ming Wang, PhD, Associate Professor
Department of Mechanical Engineering and Materials Science

Dissertation Director: Kevin P. Chen, PhD, Associate Professor
Department of Electrical and Computer Engineering

LASER HOLOGRAPHIC FABRICATION OF THREE-DIMENSIONAL PHOTONIC CRYSTAL TEMPLATES USING ADVANCED PHASE MASK TECHNIQUES

Di Xu, PhD

University of Pittsburgh, 2010

ABSTRACT: Three dimensional (3D) photonic crystal has attracted enormous interest in the last decade in both science and technology communities. Its unique capability to trap photons offers an interesting scientific perspective and can be useful for optical communication and sensing. However, the fabrication of large-scale 3D photonic structures at sub-micron scale with optimal photonic bandgap (PBG) remains a great challenge. Considerable efforts have been dedicated to develop fabrication techniques to produce large area defect-free 3D photonic structures toward device applications. This part of research need to develop a CMOS-compatible, laser interference lithography technique to produce 3D photonic structure on-chip using single- or multiple- layer diffractive optical elements (DOE). The DOEs can be incorporated into phase/amplitude masks used in optoelectronic circuit fabrications to enable a full integration of 3D photonic structures on-chip.

Presented in this dissertation is the study of novel fabrication approaches of 3D photonic crystal. Compare to others, our studies utilize phase masks to fabricate 3D diamond-like photonic crystal templates in SU8 photoresist. 3D woodpile structures were fabricated by a double-exposure of SU8 to a three-beam or five-beam interference pattern generated by phase masks. Lattice structures and the PBG can be controlled by the rotational angles and relative displacement of the phase mask between exposures. Also, by using a single optical element such as special designed prism or phase mask, we demonstrate the phase tunability in the laser holographic patterning of 3D photonic crystal and quasi-crystal lattice structures. Photonic band gap computation predicts the existence and optimization of a full band gap in fabricated structures. The current studies demonstrate a simple and flexible approach to fabricate 3D

photonic crystals with complex structures. It also lays solid ground work toward integrated fabrication of

3D photonic crystal structures on other optoelectronic components.

TABLE OF CONTENTS

LIST OF TABLES

LIST OF FIGURES

LIST OF ACRONYMS

1D: one dimensional

2D: two dimensional

3D: three dimensional

EM: electromagnetic

HL: holographic lithography

DOE: diffractive optical element

PBG: photonic bandgap

EBL: E-beam lithography

TPL: two-photon lithography

SEM: scanning electron microscope

AFM: atomic force microscope

FTIR: Fourier transform infrared spectroscopy

RIE: reactive ion etching

CVD: chemical vapor deposition

FCC: face centered cubic

FCT: face centered tetragonal

PWE: plane wave expansion

FDTD: finite difference time domain

CW: continuous wave

UV: ultraviolet

IR: Infrared

IC: integrated circuit

PDMS: polydimethylsiloxane

SU8: negative photoresist

DPHPA: dipentaerythritol penta/hexaacrylate, negative photoresist

PGMEA: propylene-glycol-methyl-ether-acetate

H-Nu470: 5,7-diiodo-3-butoxy-6-fluorone

OPPI: iodonium salt co-initiator

TMPTA: trimethylol propane triacrylate

ACKNOWLEDGEMENT

1.0   MOTIVATION

As the telecommunication and computing industries are currently facing increasing challenges to transfer data at a faster rate[1], researchers believe that it might be possible to engineer a device operate at optical, i.e. gigahertz or terahertz, frequencies. Photonic technology using light instead of electrons as a vehicle for information transfer paves the way for a new technological revolution in this field. Photons used for communication has several advantages over electrons which are currently being used in electronic circuits. Photonic devices made of a specific material can provide a greater bandwidth than the conventional copper wires and can also carry large amount of information per second without interference.

   Photonic crystals are such kind of material. They are periodic structures that allow us to control the flow of photons [2, 3]. To some extent it is similar to the way in which semiconductors control the flow of electrons. Electrons move in a piece of crystalline silicon (periodic arrangement of Si atoms in diamond-lattice), and interact with the nuclei through the Coulomb force. Consequently they see a periodic potential which brings forth allowed and forbidden electronic energy bands. The careful control of this behavior allowed the realization of the first transistor. Now, imagine a slab of dielectric material in which periodic arrays of air cylinders are placed. Photons propagating in this material will see a periodic change in the index of refraction. To a photon this looks like a periodic potential analogous to the way it did to an electron. The

1

size of the index difference between the cylinders and the background material can be made such that it confines light and, allowed and forbidden regions for photon energies are formed[4].

So it is critical to find a proper fabrication approach of photonic crystal with desired photonic band structure. Nowadays, the fabrication of photonic crystals is quite a hot topic. Intrigued by their vast potential in photonics engineering, tremendous efforts have been invested into the fabrication of 3D photonic crystal structures. However, the fabrication of those photonic crystals with a complete PBG, i.e. can exhibit bandgaps for the incident lights from all directions, still proves to be a challenge[5]. On the other way, the location of bandgap center is also important and a burning question to determine a useful communication region. Considerable efforts have been dedicated to develop fabrication techniques to produce large area defect-free 3D photonic structures toward device applications. This part of research needs to develop a CMOS-compatible, fast and repeatable technique to produce 3D photonic crystal structures with complete bandgaps around the visible and near infrared (IR) telecommunication windows[5]. Our lab in collaboration with Dr. Yuankun Lin, from the University of Texas Pan-American, proposes the fabrication approaches of complex photonic crystal templates by using different kinds of optical elements[6-8]. These elements simplify the laborious fabrication of photonic crystals and are amendable for massive production and chip-scale integration of 3D photonic structures.

1.1   OUTLINE
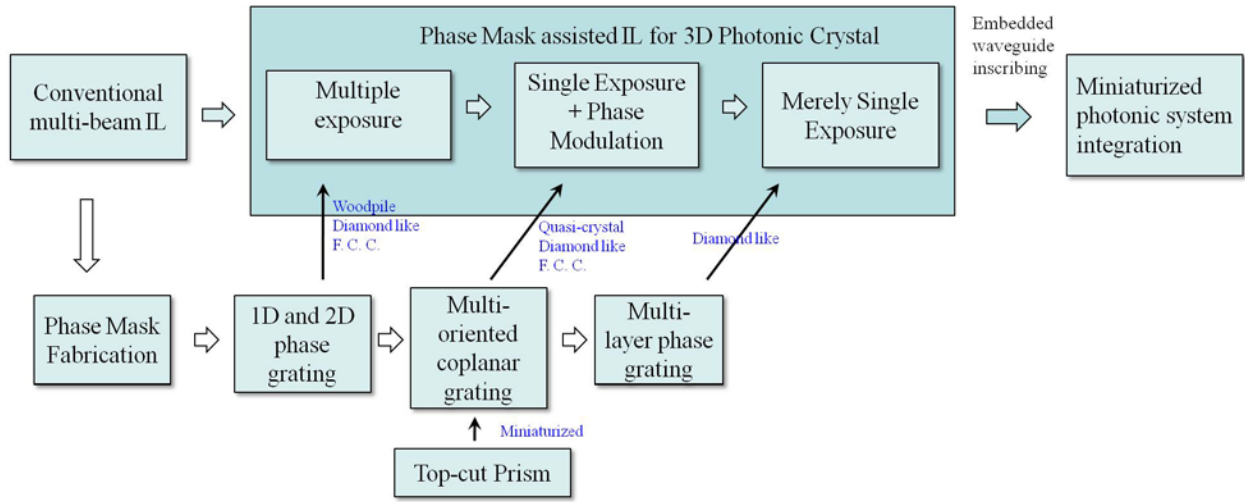
Figure 1.1 Flowchart of this dissertation.

The paper is structured in a way to describe my PhD research directions to the goal for easy and optimal fabrication processes of 3D photonic crystal template. We start from the traditional multi-beam interference lithography[9], also namely holographic lithography (HL) [10], and design various advanced phase gratings as masks to assist the HL process[11]. The process has been improved from multiple exposures to merely single exposure. At same time, by introducing phase-tuning capability, the phase mask lithography technique can be developed into single exposure to have 3D interconnected, large bandgap width photonic structures[8]. The ultimate goal is to miniaturize the phase mask integrate the mask and 3D structure with other optical components and introduce defects inside the 3D structure as waveguide.

Chapter 1 in this paper starts from the theoretical description of photonic crystals, alternatively namely as PBG materials. It also covers the principle for the occurrence of PBG,

the simulation methods for photonic band structure, the optical properties, the application and the state-of-arts fabrication approaches of the photonic crystal.

Chapter 2 first briefly introduces the HL methods, and then focuses on the DOE introduction, as a tool in HL. It will be used to fabricate 3D photonic crystal template throughout this paper. At the end, it describes the purpose of using DOEs, which is used to simplify the optical alignment and enhance the integrated system.

From chapter 4 we will begin to present our experimental work consequently. This whole chapter describes the approach of phase mask assisted 3D photonic crystal fabrication. We introduce a one dimensional (1D) commercial phase mask, lab-made coplanar two dimensional (2D) and two-layer integrated phase mask as the novel DOE, respectively. Complex 3D photonic crystal structures are formed by exposure(s) to multi-beam interference patterns via DOEs.

Chapter 5 demonstrates another approach to fabricate diamond-like structure with only one single exposure and with phase tuning ability. Both bulk reflective optical element, such as a top-cut prism, and thin film DOE, such as a specially designed planar phase mask, are employed to generate multiple coherent beams for HL process.

Chapter 6 shows a 3D photonic quasi-crystal structure fabricated by specially designed coplanar phase masks. Chapter 7 shows the HL technique combined with two-photon direct laser writing technique to fabricate the 3D structure with line defect as waveguide.

Chapter 8 concludes the paper.

2.0   PHOTONIC CYRSTAL FUNDMENTALS

Photonic crystals are classified primarily into three categories, which are, 1D, 2D and 3D crystals according to the dimensionality of the stack[4]. Depending on the refractive index contrast ratio, structure geometry and the lattice periodicity, the PBGs of photonic crystal are determined for specific frequency ranges in electromagnetic (EM) spectra. No EM waves can propagate inside the corresponding bandgap ranges except for totally reflected. Using this property we can manipulate, guide and confine photons, which in turn makes it possible to produce optical integrated circuits.

2.1   THEORY OF PHOTONIC CRYSTAL

2.1.1   Mathematical expression

First we will start from the theoretical deviation for this mysterious material. The mathematic expression of the EM wave propagation in a photonic crystal is derived from classic Maxwell's equations [12]. The periodic structure of photonic crystal will turn the equations into a linear Hermitian eigenvalue problem. According to Maxwell's equation, when an EM wave is travelling in a medium, the equation to describe the propagation can be written in S.I. unit as follows,

$$\nabla \cdot D(r,t) = 0 \tag{2.1a}$$

$$\nabla \cdot B(r,t) = 0 \tag{2.1b}$$

$$\nabla \times E(r,t) + \frac{\partial B(r,t)}{\partial t} = 0 \tag{2.1c}$$

$$\nabla \times H(r,t) - \frac{\partial D(r,t)}{\partial t} = 0 \tag{2.1d}$$

here we assume that no free charges or current applied; E and H are macroscopic electric and magnetic field, D and B are the displacement and magnetic induction fields. Now considering a lossless, isotropic, dielectric medium, the relationships for the fields can be written as;

$$D(r) = \varepsilon_0 \varepsilon(r) E(r), \; B(r) = \mu_0 H(r)$$

by substituting these equations into the places in Eq. (2.1c,d) , we obtain;

$$\begin{cases} \nabla \times E(r,t) + \mu_0 \dfrac{\partial H(r,t)}{\partial t} = 0 \\ \nabla \times H(r,t) - \varepsilon_0 \varepsilon(r) \dfrac{\partial E(r,t)}{\partial t} = 0 \end{cases} \tag{2.2}$$

Assuming that the fields are changing harmonically in time and using the linearity of Maxwell equations, we can separate the variables r and t and rewrite E and H as:

$$\begin{cases} E(r,t) = E(r)e^{-i\omega t} \\ H(r,t) = H(r)e^{-i\omega t} \end{cases} \tag{2.3}$$

Hence by substituting Eq. (2.3) into equations in Eq. (2.2), spatial profile of the fields can be found:

$$\begin{cases} \nabla \times E(r,t) = i\omega\mu_0 H(r,t) \\ \nabla \times H(r,t) = -i\omega\varepsilon_0\varepsilon_r(r)E(r,t) \end{cases} \tag{2.4}$$

Eq. (2.4) can be solved for either H or E, subject to the condition resulting from the transverse fields and assuming $e^{-i\omega t}$ time dependence cancelling;

$$\frac{1}{\varepsilon_0 \varepsilon_r(r)} \nabla \times H(r) = -i\omega E(r)$$

$$\nabla \times \left\{ \frac{1}{\varepsilon_0 \varepsilon_r(r)} \nabla \times H(r) \right\} = -i\omega \cdot (\nabla \times E(r)) = -i\omega \cdot i\omega \cdot \mu_0 H(r) = \omega^2 \mu_0 H(r)$$

recalling that $\frac{1}{c^2} = \mu_0 \varepsilon_0$, c is the speed of light, we obtain the vector Helmholtz equation,

$$\nabla \times \left\{ \frac{1}{\varepsilon_r(r)} \nabla \times H(r) \right\} = \left(\frac{\omega}{c} \right)^2 H(r) \qquad (2.5)$$

Eq. (2.5) is referred to as the master equation for the EM problem in a photonic crystal medium and can be written in a compact form;

$$\Theta_H H(r) = \left(\frac{\omega}{c} \right)^2 H(r) \qquad (2.6)$$

where, $\Theta_H = \nabla \times \left\{ \frac{1}{\varepsilon_r(r)} \nabla \times \right\}$. Eq. (2.6) is classified as eigenvalue problems with eigenvalues

$\left(\frac{\omega}{c} \right)^2$ and eigenfunction H(r). It is preferable to solve the problem for a given photonic crystal

characterized by the dielectric function ε (r), by using Eq. (2.6), which is the standard choice in

general, and then use Eq. (2.4) to find E as $E(r,t) = \left(\frac{1}{-i\omega\varepsilon_0\varepsilon_r(r)} \right) \nabla \times H(r,t)$, because the

operator Θ_H in Eq. (2.6) is proved Hermitian while the operator Θ_E, if we following a similar

procedure for E, is not.

The band structure of a photonic crystal indicates the response of the crystal to certain

wavelengths of the EM spectra for a certain propagation direction. It defines optical properties of

the crystal such as transmission, reflection and their dependence on the direction of propagation

of light. As stated above, photonic crystals are periodic dielectric materials with dielectric

functions of the form $\varepsilon(r) = \varepsilon(r + R)$ for any $R = m \cdot G$, where m is an integer and G is the primitive lattice vector. For a periodic eigenvalue problem as in Eq. (2.5)

$$\nabla \times \left\{ \frac{1}{\varepsilon_r(r)} \nabla \times H(r) \right\} = \left(\frac{\omega(k)}{c} \right)^2 H(r),$$

by using Bloch's theorem, the solutions can be chosen in the form:

$$H(r) = e^{ik \cdot r} u_k(r)$$

where, $u_k(r)$ is a periodic function on the lattice, with

$$u_k(r) = u_k(r + R)$$

for all lattice vectors. Substituting above equation into Eq. (2.5),

$$\nabla \times \left(\frac{1}{\varepsilon_r(r)} \nabla \times e^{ik \cdot r} u_k(r) \right) = \left(\frac{\omega(k)}{c} \right)^2 \left(e^{ik \cdot r} u_k(r) \right),$$

$$(ik + \nabla) \times \left(\frac{1}{\varepsilon_r(r)} (ik + \nabla) \times u_k(r) \right) = \left(\frac{\omega(k)}{c} \right)^2 \left(e^{ik \cdot r} u_k(r) \right)$$

which results in a new Hermitian eigenvalue equation,

$$\Theta_k u_k(r) = \left(\frac{\omega(k)}{c} \right)^2 u_k(r) \tag{2.7}$$

with

$$\Theta_k = (ik + \nabla) \times \left(\frac{1}{\varepsilon_r(r)} (ik + \nabla) \times \right) \tag{2.8}$$

and eigenvalues $(\omega(k)/c)^2$, over the primitive cell of the lattice at each Bloch wave vector k.

2.1.2 Regular crystal *vs* photonic crystal

Table 2.1 Comparison of regular crystal and photonic crystal

	Regular Crystal	Photonic crystal
System Periodicity	periodic potential $$V(r) = V(r + R)$$	periodic dielectric constant $$\varepsilon(r) = \varepsilon(r + R)$$
Time dependent function to separate out into normal mode	scalar wave function $$\Psi(r,t) = \sum_E c_E\, \Psi_E(r)e^{iEt/\hbar}$$	Vector wave function $$H(r,t) = \sum_\omega c_E\, H_\omega(r)e^{i\omega t/\hbar}$$
Master equation	Schrödinger Equation (Quantum Mechanics) $$\left(-\frac{p^2}{2m} + V(r)\right)\Psi_E(r) = E\Psi_E(r)$$	Maxwell Equation (Electrodynamics) $$\left(\frac{p^2}{2m} + V(r)\right)\Psi_E(r) = E\Psi_E(r)$$
Control unit	Electrons' motion	Photons' propagation
Lattice constant	Atom scale	Wavelength scale
In common	Bloch's Law (expanded into Bloch form), Eigen problem, Brillouin zone Bandgap, defects	

The analysis of photon propagation in a photonic crystal is comparable to electron dynamics in regular crystal in quantum mechanics. The mathematic expression as periodic boundary conditions are taken into account, to solve this problem can be regarded to do it in a single unit cell. The Schrödinger equation for an electron with effective mass in a crystal can be written as

$$\left(-\frac{p^2}{2m} + V(r)\right)\Psi_E(r) = E\Psi_E(r)$$

where V(r) is a period potential function with the periodicity of the lattice R, V(r)=V(r+R). The eigenstates of this equation are period functions with period R as well. Table 2.1 shows a complete comparison between photonic crystal and regular crystal, indicating the parallelism between electrons in semiconductors and photons in photonic crystals.

From Table 2.1 we can see that the electron are scalar waves, while photons are vectorial ones, which implies that in the latter case, the polarization must be taken into account. On the contrary, the electron wave equations are not scalable, since an intrinsic length measure is associated with the electron size (de Broglie wavelength) where the potential periodicity can be gauged. This restriction does not apply for photons. The photon wave equations are scalable. Hence if a PBG structure presents a given periodicity length, it will show photonic bands in a certain range of frequency.

2.1.3 PBG formation

Back to Eq. (2.8), if k is given, there will have an infinite set of modes with discretely spaced frequencies, numbered by band index n. However, we can see that the operator Θ_k is restricted by given k. Then we reach the conclusion the frequency of each band will vary continuously as k varies; and the modes of a photonic crystal are a family of continuous function $\omega_n(k)$, indexed in order of increasing frequency by n. The band structure problem for a photonic crystal is to plot ω (k) as a function of wave vector k, as shown in Fig. 2.1. Because the eigensolutions are periodic functions of k, that is the solution at k is the same as the solution at k+G, where G is a primitive reciprocal lattice vector, we only need to consider the k points in the irreducible Brillouin zone.

10

Furthermore, by considering the invariance of the master equation (Eq. (2.5)) under time reversal (ω (k) = ω (-k)) for a photonic crystal, the band structure can be further simplified by only solving the non-negative Bloch vectors [12].
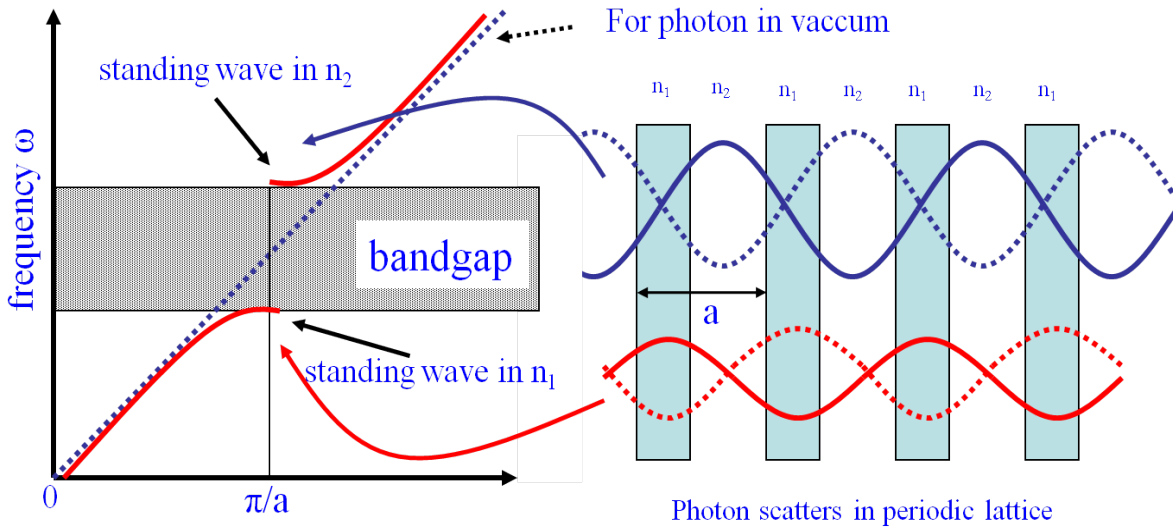
Figure 2.1 (left) Energy dispersion relations for a free photon and a photon in a PBG structure; (right) illustration of two kind of confined modes (standing waves) in a 1D photonic crystal, corresponding to the upper and lower bounds of PBG.

An intuitive explanation for the PBG formation can be seen from Fig. 2.1 (right). The EM wave incidents from one side and reflected at each interface of n_1 and n_2. For certain frequencies, if the reflected waves generated at each interface happen to be in phase, they will be summed up until cancel the incident wave. Thus in dispersion spectrum, a gap (or band, peaks) corresponding to those frequencies lights will show up. The confined modes, i.e. standing waves stored in n_1 and n_2, correspond to the PBG edge frequencies with zero group velocities.

11

Conventionally the relative PBG width is defined by the PBG width $\Delta\omega$ over the central band frequency ω_0 $PBG\ width \equiv \dfrac{\Delta\omega}{\omega_0}$.

From dispersion relationship $\omega = kc/n$, we have

$$\Delta\omega = \omega_2 - \omega_1 = \frac{\pi}{a}c\left(\frac{1}{n_2} - \frac{1}{n_1}\right)$$

$$\text{and} \quad \omega_0 = 1/2(\omega_2 + \omega_1) = \frac{\pi}{2a}c\left(\frac{1}{n_2} + \frac{1}{n_1}\right)$$

then we can conclude the PBG of photonic crystal have properties as follow:

1. PBG width **independent** of light polarization and k vector directions;

2. To have a PBG in communication width (visible or near IR ranges), i.e. the central frequency ω_0 should in that range, the crystal lattice a should be **comparable** to the operating wavelength;

3. $\Delta\omega$ is proportional to the refractive index ratio n_2/n_1;

4. The **filling ratio** of high index material determines the amplitude of the standing waves store, which means it changes upper and lower bound locations of the PBG.

5. In 3D photonic crystal, as shown in Fig.2.2, the absolute and complete PBG is defined as the overlap region in every G direction of the crystal. So A good crystal lattice with **symmetry** as high as possible for the first Brillouin zone in reciprocal space is necessary.
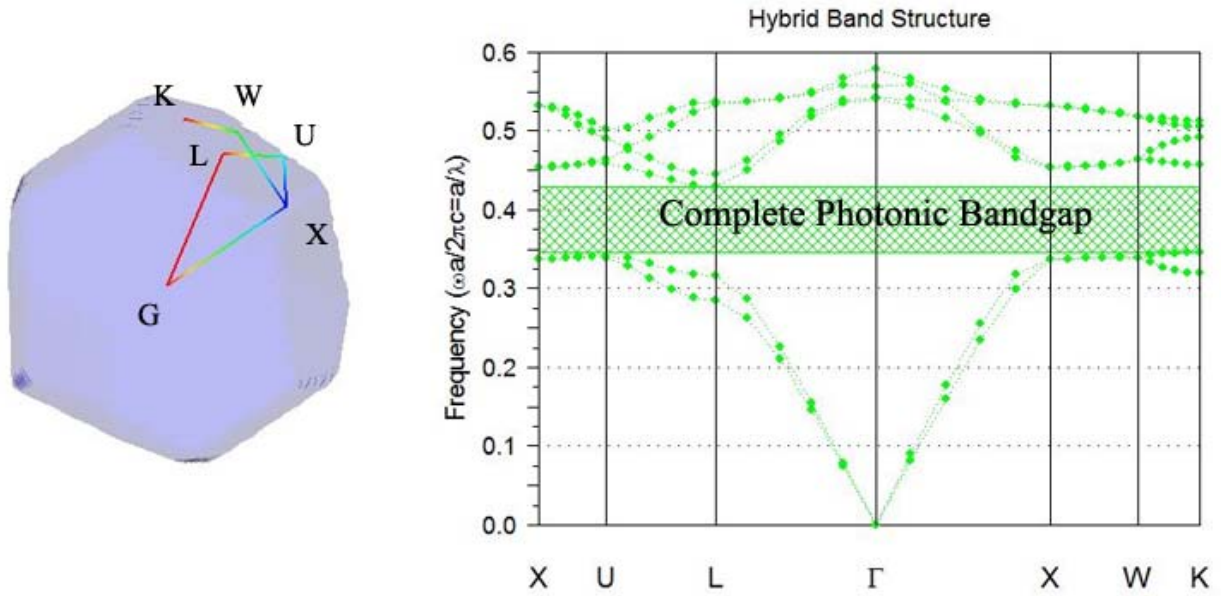
Figure 2.2 (left) First Brillouin zone of a 3D woodpile photonic crystal; (right) a complete PBG shows presents the overlap gap region in every primitive vector (G vector) directions.

Optical measurements are important to photonic crystals. Reflection and transmission spectroscopy is the principle tool used to characterize the PBG structures. It reveals the forbidden bands through increased reflection level or decreased transmission level, which forms a (Bragg reflection) "peak" or "gap" in the wavelength resolved domain, experimentally obtained by an optical spectrometer or Fourier Transform Infrared Spectroscopy (FTIR). If we do the Fourier transform for the time domain spectrum (E(r) or H(r)) into frequency domain, the photonic band structure spectrum (ω(k)) can be distinctly derived [12].

In the presence of structural disorder, transmission/reflection spectra obtained in experiments are affected differently. Reflection peaks tend to become less intense, asymmetric and even spectrally wider. Angle-resolved transmission/reflection spectra are important in PBG structure characterization, especially for 3D PBG structures. Realization of complete PBGs has been a goal for researches on fabrication of 3D PBG structures. The only way to ensure a

13

complete bandgap is to obtain all-angle transmission/reflection spectra and find the corresponding mutual reflection peak or transmission valley for all incident angles.

Also, optical diffraction pattern measurement is the simplest method to measure the long-range order of the PBG structures. Diffraction patterns observed with visible light have been used to analyze the disorder in PBG structures. Studies in polarization properties of PBG structures have also been a concern of many researchers.

Polarization has been an important issue for 2D PBG structures[13]. The transverse electric and transverse magnetic modes, the two linear polarization directions corresponding to the electric field oscillation in the 2D PBG structure plane or perpendicular to that plan respectively, usually contribute to different photonic band structures. The polarization-based transmission devices such as 2D photonic crystal slab waveguides have been widely studied. For 3D PBG structures, the studies of polarization characteristics are still mostly on the fundamental principles. The polarization in 3D PBG structures is presented by s-light and p-light as defined in physical optics when Fresnel law is discussed. The fundamental questions, such as how the eigenmodes could be coupled into certain photonic bands, were solved with the discussion of incident light polarization and structure symmetry.

2.2 NUMERICAL SIMULATION

For a given photonic crystal with periodic distribution of $\varepsilon(r)$, how can we calculated the $\omega_n(k)$? Various theoretical approaches have been proposed to photonic crystals which are based on the rearrangement of Maxwell's equation in form of eigenvalue problem for the electric and magnetic fields. These formulations have been suggested to develop numerical methods to

design different photonic lattice geometries and to predict their band structure which reveals the optical properties of these lattices.

There are many theoretical methods to calculate the band structure of the photonic crystals. Among them, the Plane Wave Expansion (PWE) method [14], the Finite-Difference Time-Domain (FDTD) method [15-18], the transfer matrix method [19, 20], Finite Element Method [21] and Effective Medium Theory [22] are the most popular ones. Depending on the crystal structure to be analyzed, one method may have an advantage over the others. In the following I will put emphasis on the theory of PWE and FDTD methods, which have been frequently used in our research.

2.2.1 Plane wave expansion

PWE method depends on the expansion of the EM field with a plane-wave basis set and using this basis set to solve the master eigenvalue equation, Eq. (2.5), to determine the band structure of the crystal. This approach is very useful for structures with no defects. The strategy is to expand, electric (or magnetic) fields for each field component, in terms of the Fourier series components along the reciprocal lattice vector G; also, the dielectric permittivity $\dfrac{1}{\varepsilon_r(r)}$ (which is periodic along reciprocal lattice vector, for photonic crystals) is also expanded through Fourier series components,

$$\begin{cases} E(r,\omega) = \displaystyle\sum_{n=-\infty}^{+\infty} K_n^E \, e^{-iG\cdot r} e^{-ik\cdot r} \\ \dfrac{1}{\varepsilon_r(r)} = \displaystyle\sum_{m=-\infty}^{+\infty} K_m^{\varepsilon_r(r)} e^{-iG\cdot r} \end{cases},$$

15

where K's are the Fourier series coefficients subscripted by m, n respectively. Using these expansions in the Maxwell's curl equation for E,

$$\frac{1}{\varepsilon_r(r)}\nabla \times [\nabla \times E] = \left(\frac{\omega}{c}\right)^2 E$$

and simplifying under assumptions of a source free, linear, and non-dispersive region we can obtain the eigenvalue relations which can be solved. In this paper we use PWE as our primary simulation method implemented by the Matlab/MIT MPB package [23] for the PBG calculation.

2.2.2   Finite-Difference Time-Domain Method

The FDTD method, proposed by Yee, in 1966 [18], is another numerical method used widely for the solution of EM problems. Its original purpose is to solve a scattering problem in the time domain rather than in the frequency domain. Harmonic solutions are obtained in a second step through a Fourier transformation in time. The method is adapted to the specific case of photonic crystal materials by Joannopoulos in 1995[12]. Considering non-harmonic time-dependent fields, the algorithm is to determine the total field at any time t and at any point of space when the field enters a photonic crystal with finite size. The derivation is starting from the differential form of Maxwell's equation (Eq. (2.1)),

$$\begin{cases} \nabla \times E = -\dfrac{\partial B}{\partial t} \\ \nabla \times H = J + \dfrac{\partial D}{\partial t} \end{cases} \text{and} \begin{cases} \nabla \cdot D = \rho \\ \nabla \cdot B = 0 \end{cases},$$

16

By substituting constitutive relations $D(r) = \varepsilon_0 \varepsilon(r) E(r)$, $B(r) = \mu_0 H(r)$ in, we can rewrite the six scalar equations in matrix from as,

$$
\begin{cases}
\begin{bmatrix} \dfrac{\partial H_z}{\partial y} - \dfrac{\partial H_y}{\partial z} \\[1em] \dfrac{\partial H_x}{\partial z} - \dfrac{\partial H_z}{\partial x} \\[1em] \dfrac{\partial H_y}{\partial x} - \dfrac{\partial H_x}{\partial y} \end{bmatrix} = \varepsilon_0 \begin{bmatrix} \varepsilon_{xx} & 0 & 0 \\ 0 & \varepsilon_{yy} & 0 \\ 0 & 0 & \varepsilon_{zz} \end{bmatrix} \cdot \begin{bmatrix} \dfrac{\partial E_x}{\partial t} \\[1em] \dfrac{\partial E_y}{\partial t} \\[1em] \dfrac{\partial E_z}{\partial t} \end{bmatrix} + \begin{bmatrix} \sigma_{exx} & 0 & 0 \\ 0 & \sigma_{eyy} & 0 \\ 0 & 0 & \sigma_{ezz} \end{bmatrix} \cdot \begin{bmatrix} E_x \\ E_y \\ E_z \end{bmatrix} \\[3em]
\begin{bmatrix} \dfrac{\partial E_y}{\partial z} - \dfrac{\partial E_z}{\partial y} \\[1em] \dfrac{\partial E_z}{\partial x} - \dfrac{\partial E_x}{\partial z} \\[1em] \dfrac{\partial E_x}{\partial y} - \dfrac{\partial E_y}{\partial x} \end{bmatrix} = \mu_0 \begin{bmatrix} \dfrac{\partial H_x}{\partial t} \\[1em] \dfrac{\partial H_y}{\partial t} \\[1em] \dfrac{\partial H_z}{\partial t} \end{bmatrix}
\end{cases}
\tag{2.9}
$$

FDTD employed an algorithm of Yee's lattice to implement the calculation. The computational domain is divided into small unit lattice based on the computation time step Δt. Each lattice centers its E and H fields components in 3D space, thus every E is surrounded by four circulating H components and every H component is surrounded by four circulation E components. The domain is divided into a number of rectangular unit cells and every E and H field components are separated by $\Delta t / 2$ in time.

Assuming any scalar function of space and time at a discrete point in the grid and at a discrete point in time is marked as $u_{i,j,k}^n = u(i\Delta x, j\Delta y, k\Delta z)$. We know that one can discretize a differential equation u into a difference expression,

$$\frac{du}{dx}(i\Delta x, j\Delta y, k\Delta z) = \frac{u_{i+1/2,j,k}^n - u_{i-1/2,j,k}^n}{\Delta x} + O\left((\Delta x)^2\right),$$ then we can solve the Eq. (2.9) for components E and H,

$$
\begin{cases}
E_{x\,i,j,k}^{n+1} = \left(1 - \dfrac{\sigma_{xx}(i,j,k)\Delta t}{\varepsilon_{xx}(i,j,k)}\right) E_{x\,i,j,k}^{n} + \dfrac{\Delta t}{\varepsilon_{xx}(i,j,k)\Delta y}\left(H_{z\,i,j,k}^{n+1/2} - H_{z\,i,j,k}^{n-1/2}\right) - \dfrac{\Delta t}{\varepsilon_{xx}(i,j,k)\Delta z}\left(H_{y\,i,j,k+1}^{n+1/2} - H_{y\,i,j,k+1}^{n-1/2}\right) \\[2em]
E_{y\,i,j,k}^{n+1} = \left(1 - \dfrac{\sigma_{yy}(i,j,k)\Delta t}{\varepsilon_{yy}(i,j,k)}\right) E_{y\,i,j,k}^{n} + \dfrac{\Delta t}{\varepsilon_{yy}(i,j,k)\Delta z}\left(H_{x\,i,j,k}^{n+1/2} - H_{x\,i,j,k}^{n+1/2}\right) - \dfrac{\Delta t}{\varepsilon_{yy}(i,j,k)\Delta x}\left(H_{z\,i+1,j,k}^{n+1/2} - H_{y\,i,j,k}^{n+1/2}\right) \\[2em]
E_{z\,i,j,k}^{n+1} = \left(1 - \dfrac{\sigma_{zz}(i,j,k)\Delta t}{\varepsilon_{zz}(i,j,k)}\right) E_{z\,i,j,k}^{n} + \dfrac{\Delta t}{\varepsilon_{zz}(i,j,k)\Delta x}\left(H_{y\,i,j,k}^{n+1/2} - H_{y\,i,j,k}^{n+1/2}\right) - \dfrac{\Delta t}{\varepsilon_{zz}(i,j,k)\Delta y}\left(H_{x\,i,j+1,k}^{n+1/2} - H_{x\,i,j,k}^{n+1/2}\right)
\end{cases}
$$

$$
\begin{cases}
H_{x\,i,j,k}^{n+1/2} = H_{x\,i,j,k}^{n-1/2} + \dfrac{\Delta t}{\mu_0 \Delta z}\left(E_{y\,i,j,k}^{n} - H_{y\,i,j,k-1}^{n}\right) - \dfrac{\Delta t}{\mu_0 \Delta y}\left(E_{z\,i,j,k}^{n} - E_{z\,i,j-1,k}^{n}\right) \\[2em]
H_{y\,i,j,k}^{n+1/2} = H_{y\,i,j,k}^{n-1/2} + \dfrac{\Delta t}{\mu_0 \Delta x}\left(E_{z\,i,j,k}^{n} - H_{z\,i-1,j,k}^{n}\right) - \dfrac{\Delta t}{\mu_0 \Delta z}\left(E_{x\,i,j,k}^{n} - E_{x\,i,j,k-1}^{n}\right) \\[2em]
H_{z\,i,j,k}^{n+1/2} = H_{z\,i,j,k}^{n-1/2} + \dfrac{\Delta t}{\mu_0 \Delta y}\left(E_{x\,i,j,k}^{n} - H_{x\,i,j-1,k}^{n}\right) - \dfrac{\Delta t}{\mu_0 \Delta x}\left(E_{y\,i,j,k}^{n} - E_{y\,i-1,j,k}^{n}\right)
\end{cases}
$$

Once we know the initial incident E and H values, and we know the periodic dielectric constant distribution $\varepsilon(i,j,k)$ in the computational domain, we can find the next $\Delta t/2$ corresponding field components in above recursion equations. These equations shall be alternately used for calculating the time variation of the components of the electric and magnetic fields.

FDTD is a popular EM modeling technique that is easy to understand and implement in software. Since it is a time-domain technique it can cover a wide frequency range with a single simulation run. Another advantage is that is can be applied to the 3D arbitrary geometries including our 3D photonic crystal model. In this method, we need concern about convergence and perfect absorbing boundary conditions, which means no reflection at the boundary, to achieve the maximum accuracy in the computation.

Our group employs the FDTD based analysis software: the Fullwave, BeamProp and Bandsolver packages from RSoft Design Group, Inc., to perform the PBG and transmission

spectra calculations, and EM field and energy distributions in the optical waveguide and circuits. The numerical computations of a photonic crystal have predicted appropriate directions for our experimental works.

2.3   PHOTONIC CRYSTAL APPLICATIONS

Photonic crystals have been made various optical components using their capabilities to steering the photons. In optical industries, 1D photonic crystal are already in widespread use in the form of thin-film optics [24] with applications ranging from low and high reflection coatings on lenses and mirrors to color changing paints and inks. Higher dimensional photonic crystals are of great interest for both fundamental and applied research, and the 2D ones are beginning to find commercial applications. The first commercial products involving two-dimensionally periodic photonic crystals are already available in the form of photonic crystal fibers [25], which use a micron scale structure to confine light with radically different characteristics compared to conventional optical fiber for applications in nonlinear devices and guiding exotic wavelengths. The 3D counterparts are still far from commercialization but offer additional features possibly leading to new device concepts (e.g. optical computers [26]), when some technological aspects such as manufacturability and principal difficulties such as disorder are under control. Applications of PBG structures are numerous and mainly focused on the fabrication of devices that use photons as information carriers instead of electrons. Some applications rely on the existence of PBG; others rely on the peculiar properties of the bands and their dispersion.

If a line defect is appropriately introduced in a perfect PBG structure, the line defect will work as a light waveguide. There is a wealth of proposed applications relating to this principle of functioning including linear waveguide [27], bendings [28], crossings, splitting [29, 30], junctions, add-drop filters [31], *etc.* All the devices in this category can direct the flow of light as electrons are directed by conductive wires. These waveguides can be made to bend through sharp corners without energy loss since scattering loss is prohibited by the nature of the PBG structures. Waveguides in a 2D PBG structures have been studied extensively. A commercial PBG fiber is basically a 2D PBG waveguide in cylindrical coordinates.

Another application of PBG structures is to make nano-lasers [32]. A laser is made of a medium where population inversion is attained, whereby gain and amplification are achieved though stimulated emission. By introducing a point defect, which is usually at a sub-wavelength scale, in a PBG structure will be a perfect nano-cavity to function as a laser. These significant principles make it possible to make laser-on-chip which will greatly improve the capability of integrated photonic circuits. Recently, the major challenge is how to decrease the lasing threshold and to constitute an all-optical transistor [33] with a PBG laser [34].

Since PBG structures are highly dispersive, the laws of refraction take surprising forms in PBG structures. The light propagation is always normal to the equifrequency surfaces. The region of curvature produces very strong divergence for slight change in incident wave vector and wavelength. The fact that a very slight change in wavelength results in a strong change of shape of the equifrequency surfaces can be applied to design a super-prism [35]. This dispersion property of PBG structure would be extended to an extreme case of negative refraction [36], with which the light could be delivered to an abnormal direction even to the same side of the surface normal with the incident beam. This effect is being studied and experimentally implemented for

20

de-multiplexers, in 2D PBG so far. The applications of 3D PBG structures are still rare due to the difficulties in analyzing and realization of complex refraction situation. Nevertheless, 3D photonic crystal structures have been the main subject of intense scientific and engineering interests since the first introduction. The existence of full and complete, non-polarization dependent PBG in 3D photonic crystals gives rise to a number of peculiar optical properties useful for photonic engineering. Most important, the fabrication of 3D photonic crystals with a complete PBG in visible and near IR regimes remains a great challenge.

2.4   FABRICATION APPROACHES

So how we can fabricate the periodic PBG structures which can steer the flow of light? A 1D PBG structure is a stack of thin dielectric films. The real challenges to fabricate PBG structures began with 2D and 3D periodic microstructures working in microwave range in late 1980s. There are two major categories in micro fabrication process: top-down approach and bottom-up approach. The former is to inscribe micro/nano features from bulk materials. The latter is to build up micro/nano structures from basic units such as atoms and molecules. Both methods were utilized to fabricate PBG structures.

Electro-chemical etching [37] used to be a common top-down method to fabricate 2D periodic structures at the early age of PBG structure development. This method was able to etch porous materials with nano-scale holes with nice order and high aspect ratio, which yield perfect 2D PBG structures: dielectric constant change in the 2D planes and good uniformity along the third direction. An obvious disadvantage is that it is limited to 2D structures. Few reports were devoted to the fabrication of 3D PBG structures with the electro-chemical etching method.

21

Although there are a large variety of materials exhibiting pores, only Si, Alumina are exhibiting the high surface quality required in PBG structure applications. Another improved approach for 2D photonic crystal fabrication is by deep anisotropic dry etching in silicon, which can be integrated with ideal bended waveguide. 2D photonic device in the micron and submicron wavelength region has been greatly intensified when investigations deal with photonic structures in III-V compounds like GaAs, GaAs/AlGaAs [38], AlGaAs [39] and InP [40]. Fabrication is achieved using chlorinated plasmas, either by reactive ion etching or chemically assisted ion beam etching.

Lithography is another top-down method to fabricate PBG structures, using an electron beam, an x-ray, or ultraviolet (UV) light. E-beam lithography combined with layer-by-layer assembly [41] could be used to fabricate 3D woodpile structures in semiconductor materials. However, this method requires expensive equipment and tedious procedures. Multi-photon lithography [42] using a laser is well utilized in this area. This method is usually applied to photoresist polymers. Therefore, it is also called laser direct writing with multi-photon polymerization. Based on the polymerization of photoresist, HL has attracted attention from researchers [9, 10, 43]. HL uses the elegant optical principle of interference, forming a periodic distribution of light intensity, which could be used to interact with photoresist materials to form periodic structures in 1D, 2D and 3D.

Based on the mature techniques to synthesize and self-assemble mono-dispersive silica particles, silica colloidal crystals [44] are ideal for fabricating PBG structures. The colloidal crystals have the face-centered cubic (FCC) structure. Since it possesses the Brillouin zone with the most circular shape, the FCC structure is well accepted to produce large and complete PBGs [45]. There are many advantages in using colloidal crystals. First, colloidal crystals could be

inverted into other materials using chemical vapor deposition processes. Second, the colloidal particles with metallic or semiconductor cores can also be self-assembled into high-quality colloidal crystals. It is possible to adjust the optical properties of colloidal crystals by controlling core materials and core-shell geometries.

A latest top–down technique to fabricate 3D woodpile structure direct in high index material that enables excellent optical performance has been achieved. The 3D periodic structure is created directly by reactive ion etching at angles of 45° with respect to the sample surface by using a 2D binary mask. The resulting structure corresponds to the woodpile 3D structure, rotated by 90° with respect to the conventional configuration [46]. However, the method is also limited by the etching depth and direction control of etchant flow.

We chose the HL method as our primary approach to fabricate 3D PBG materials because of the tradeoff of the cost, time and quality. The goal of our project has been to develop a method which is simple and robust, looking toward the possibility of mass fabrication as a long-term goal. However, the most obvious approach, involves a large, complicated combination of beam splitters, mirrors and analyzers. Such an arrangement would be sensitive to vibration and alignment issues, as well as costly and cumbersome to maintain. Therefore, this approach was to be improved in favor of an integrated approach, which will be addressed in the next chapters.

3.0   HOLOGRAPHIC LITHOGRAPHY APPROACH

Experimental studies of photonic crystals have been addressed to the methods for fabricating complex nano/micro-structures. It is now possible to produce 2D photonic crystal, at high volume and low cost, through use of deep UV photolithography or E-beam lithography (EBL), which is the standard tool of the electronics industry. But a large-scale efficient micro-fabrication of 3D PBG microstructures has been a scientific challenge over the past decade. So far, a number of fabrication techniques such as conventional multilayer stacking of woodpile structures by using semiconductor fabrication processes, colloidal self-assembly, and multi-photon direct laser writing, have been employed to produce sub-micron 3D photonic crystals or templates. Those methods have achieved different levels of success to some extent. However, we still need to find an economical and rapid way to able to produce defect-free nano/micro-scale structure over large area uniform photonic crystal in a simple step fabrication. This mission has been accomplished as the discovery of the HL method.

3.1   PRINCIPLE

HL has recently been employed to fabricate 3D photonic crystals by exposing a photoresist or polymerizable resin to interference patterns of laser beams. This interference technique requires multiple coherent beams converge on the same spatial region, which is also called multi-beam

IL. It is promising because it can create periodic microstructures in polymers without extensive lithography and etching steps. The monochromaticity and spatial volume of laser beam has produced nearly defect-free, submicron scale structures over large substrate areas. Photonic structures are defined in photoresist by iso-intensity surfaces of interference patterns. In the case of negative photoresist, the underexposed material is then dissolved away in the post-exposure processing. The overexposed region forms a periodic network motif and acts as a 3D photonic crystal template. The template can then be infiltrated at room temperature with SiO_2 and burned away, leaving behind a daughter inverse template. Finally, the daughter template is inverted by infiltration with silicon and selective etching of SiO_2[47].

HL allows complete control of the translational symmetry of the photonic crystal and has considerable freedom to design the unit cell. The electrical field of a laser beam can be described by

$$E_i(r,t) = E_i \cos(k_i \cdot r - \omega t + \delta_i)$$

where k and ω are the wave vector and angular frequency of the beam, respectively, E is the constant of electric field strength, and δ is the initial phase of the beam. When two or more coherent laser beams are presented simultaneously in the same region, the waves interfere with each other and generate a periodic spatial modulation of light. The intensity distribution of the interference field for N laser beams can be described by a Fourier superposition,

$$I_{int} = <\sum_{i=1}^{N} E_i^2(r,t)> + \sum_{i<j}^{N} E_i \bullet E_j \cos[(k_i - k_j) \bullet r + (\delta_i - \delta_j)]$$

The structure of the interference pattern can be designed by controlling interfering beam properties such as electric field strength, polarization, wave vector, and phase. The photonic structure formed through HL has the translational periodicity determined by the difference between the wave vectors k_i-k_j of the interfering beams. Therefore, lattice constants of the

photonic structure are proportional to the wavelength of the interfering laser beam. The polarization, represented by the electric field vector, determines the motif placed within the unit cell of the photonic lattice. The initial phase difference shifts the interference pattern and changes the motif within the unit cell. The laser intensity, exposure time, photoresist preparation, and post-exposure development condition will also contribute to the motif of the interference pattern. The photonic structure formed through HL should have good connectivity in both the dielectric and the air component so that the structure is self-supporting and the unwanted photoresist can be dissolved away.

The N coherent laser beams produces an intensity pattern with maximal (N-1) dimensional periodicity if the difference between the wave vectors is non-coplanar [48]. As shown in Fig. 3.1, two interfering beams form a 1D fringe pattern and three crossed beams form a 2D hexagonal log-pile pattern. By using three-beam interference, arrays with hexagonal symmetry can be generated, while with 4 beams, arrays with rectangular symmetry are generated. Hence, by selecting different beam combinations, and even performing some pattern translations, patterns with different lattice symmetries are possible to make.

$$I(r) = I_0 + \Delta I(r) = \left\langle \sum_{i=1}^{N} E_i^2(r,t) \right\rangle$$

$$+ 2\sum_{i<j}^{N} E_i \bullet E_j \cos[(k_i - k_j)\bullet r + (\delta_i - \delta_j)]$$
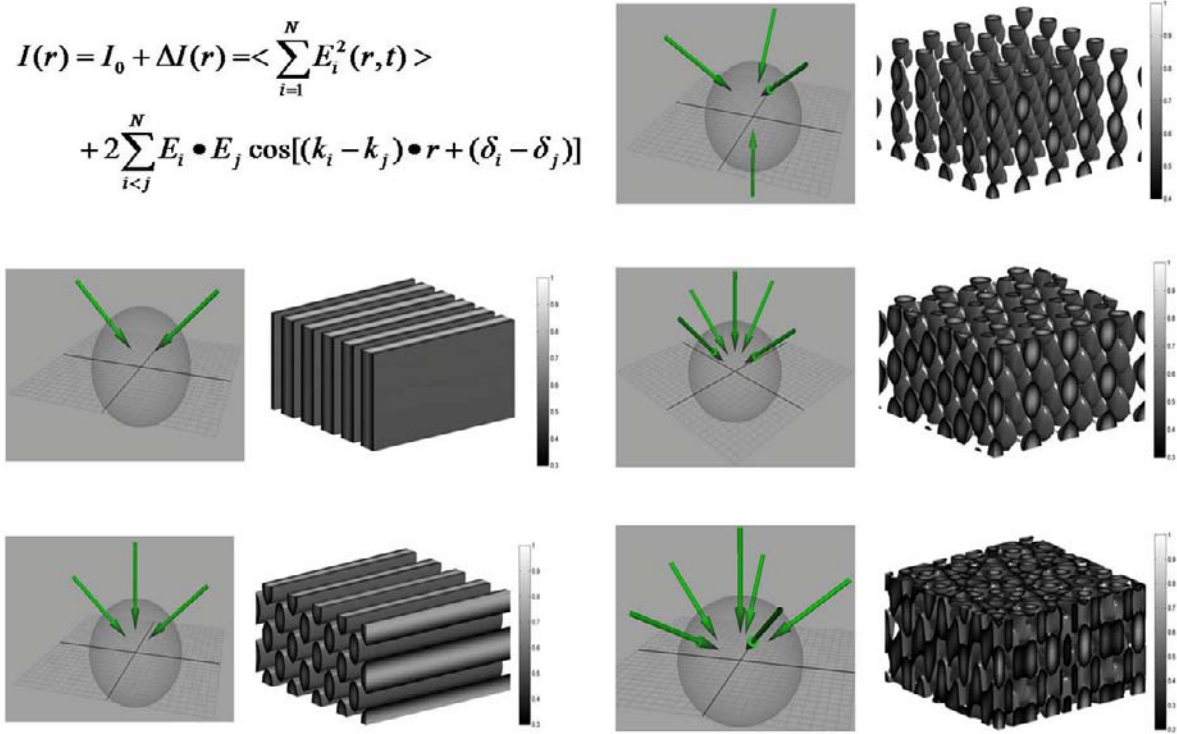
Figure 3.1 Multibeam interference visualized examples. N beams can form maximal (N-1) dimensional periodicities pattern.

For HL to be successful, coherence requirements must be met. It is preferred to use a monochromatic or coherent light source. This is readily achieved with a laser or filtered broadband sources. The monochromatic requirement can be reached if a diffraction element is used as a beam splitter, since different wavelengths would diffract into different angles but eventually recombine anyway. In this case, spatial coherence and normal incidence would still be necessary. The coherent length for our laser system requires that the path difference cannot exceed 10cm.

3.2   BEAM-SPLITTING OPTICAL ELEMENT

Fabrication strategies that rely on interference of multiple independent beams can introduce alignment complexity and inaccuracies due to differences in the optical path length and angles among the interfering beams as well as vibration instabilities in the optical setup. In order to improve the optical setup, DOE or phase masks have been introduced to create the interference pattern for the holographic fabrication of photonic crystals [49, 50]. Other than the traditional bulk optical reflective/refractive elements such as mirrors [51], beam splitters [48] and top-cut prisms [52, 53], a diffraction based optical element is a promising alternative CMOS-compatible choice for 3D HL. It can be incorporated into phase/amplitude masks used in optoelectronic circuit fabrications to enable a full integration of 3D photonic structures on-chip.

3.2.1   Reflective optical element
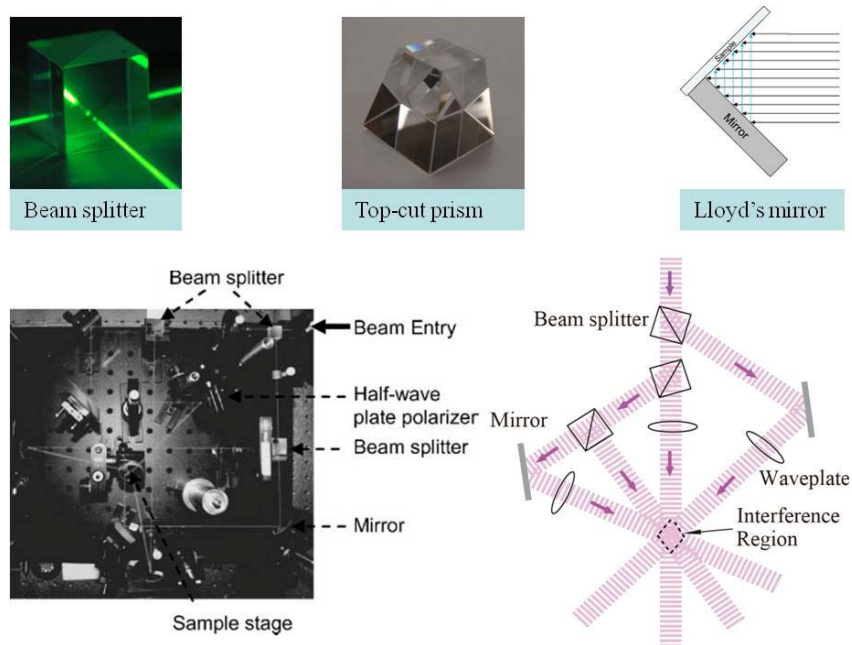
Figure 3.2 Traditional reflective optical elements to provide multiple coherent beams for interference.

An approach for easy fabrication of 2D and 3D photonic crystal microstructures is based on reflective beam splitting and overlapping by mirrors, beam-splitters or a single top-cut prism. By designed the prism properly, the number, angle, and diffracting efficiency of the output diffractive beams can be modulated. This give us the ability to fabrication more complex microstructure with high symmetry, such as FCC or diamond-like lattice [45]. This work is first demonstrated by Y. V. Miklyaev for a four beam interference to generate stable and uniform face-centered hexagonal structure [54]. Those four beam includes 3 three diffractive beams from the lateral surface of the prism and the center beam transmitted from the top surface. If we design more the lateral surface of the prism, more diffractive beams will participate into the interference. Thus we can get FCC structure or some quasi-crystal structures [55]. However, because all the beams are coming from the same half plane, the periodicity in axis direction (vertical direction of pattern) will be relative large than that in other dimension. It is not easy to fabricate a interconnect structure if too many diffractive beams participate in the interference. Otherwise the contrast ratio must be lowered, that is to say to increase the exposure dose. Bandgap simulation prediction the complete bandgap only exists when a structure has a high air filling ratio. Then we need to find an approach to compensate the structure symmetry. We are currently employing a phase retarder to modulate on diffractive beam to less the vertical periodicity or take multiple exposures to superimpose two simple lattices to one high-symmetry lattice. The prism methods show a promising way to fabrication photonic crystal as a complement of phase masks in the integrated DOE design.

3.2.2 Diffractive optical element

A DOE has advantage over reflective optical element due to its thin thickness and small structure feature. Usually only when the element feature reach the scale of optical wavelength, the diffractive will happen. A phase mask, typical a phase grating with periodically index variation in height direction, can create multiple laser beams in various diffraction orders that are inherently phase-locked and stable for reproducible creation of 3D interference patterns from a single laser beam. The 1D phase mask will create stable three in-plane output beams. These coherent beams are then generating a pattern inside the overlap region below the phase mask, in shape of 2D log-pile. The pattern is recorded in a photoresist to form periodic template.
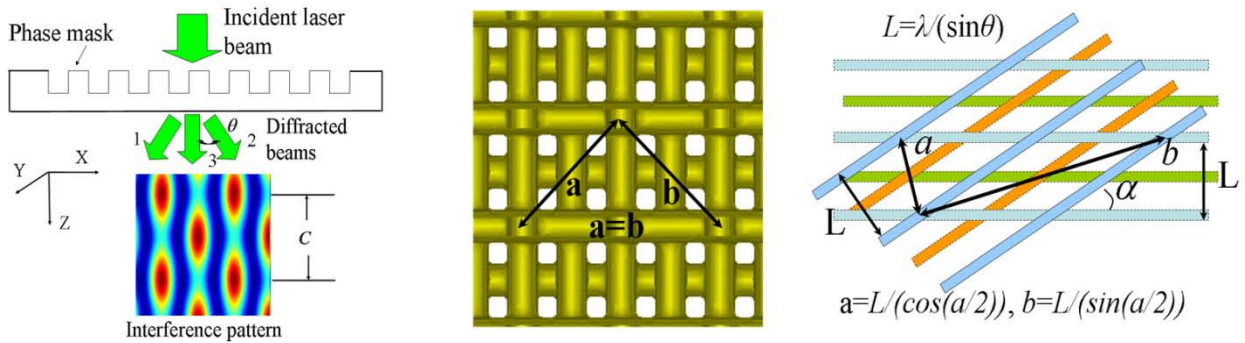
Figure 3.3 (left) phase mask based interference. A phase mask can replace a complex optical setup for a generation of interference pattern; (middle) a simulated woodpile-type photonic structure formed in the doubly-exposed photoresist; (right) a schematic illustration of woodpile-type photonic structure with orthorhombic or tetragonal symmetry and its lattice constants.

Theoretically, when a single beam goes through a 1D phase grating, the beam will be diffracted into three beams as shown in Fig. 3.3 (left). Beams 1 and 2 are from first order

diffraction and beam 3 is from zero order diffraction. Beam 1 or 2 has a diffraction angle θ relative to beam 3. Mathematically these three beams are described by:

$$\bar{E}_1(\bar{r},t) = E_1 \cos[(k\cos\theta)z - (k\sin\theta)x - \omega t + \delta_1]$$

$$\bar{E}_2(\bar{r},t) = E_2 \cos[(k\cos\theta)z + (k\sin\theta)x - \omega t + \delta_2]$$

$$\bar{E}_3(\bar{r},t) = E_3 \cos(kz - \omega t + \delta_3)$$

These three beams will generate a 2D interference pattern. The interference pattern is determined by the laser intensity distribution I in 3D space:

$$I = \frac{1}{2}E_1^2 + \frac{1}{2}E_2^2 + \frac{1}{2}E_3^2 + (E_1 E_2)\cos[(2k\sin\theta)x + (\delta_2 - \delta_1)]$$
$$+ (E_1 E_3)\cos[(2k\sin^2(\frac{\theta}{2}))z + (k\sin\theta)x + (\delta_3 - \delta_1)]$$
$$+ (E_2 E_3)\cos[(2k\sin^2(\frac{\theta}{2}))z - (k\sin\theta)x + (\delta_3 - \delta_2)]$$

The interference pattern generated behind the phase mask is shown in the Fig.3.3 (left), assuming the incident laser beam has a polarization in y direction. The interference pattern is periodic in the z-direction as well as in x-direction. The periodicity of the interference pattern along x direction is $\lambda/(\sin\theta)$ (where λ is the wavelength of laser beam generating the interference pattern). The periodicity c of the interference pattern along z direction is $\lambda/(2\sin^2(\theta/2))$. After the photoresist is exposed to such interference pattern, the sample is rotated by an angle of α along the propagation axis of the incident beam and its position is displaced along the laser propagation direction by 1/4 times $\lambda/(2\sin^2(\theta/2))$. Then the photoresist receives second exposure. The doubly-exposed photoresist is then developed to form a 3D woodpile-type photonic crystal template. Fig. 3.3 (middle) shows a simulated photonic structure formed with the rotation angle α=90° if a negative photoresist is used.   After the photoresist development, the under-exposed area is

dissolved away while the area exposed with above-threshold laser dosage is networked to form periodic structures. We illustrate in Fig. 3.3 (right) how we construct crystal lattices. We set a fundamental length scale $L=\lambda/(\sin\theta)$ for such structure because the three beam interference pattern is determined by the laser wavelength and the interference angle θ. L is actually equal to the grating period of the phase mask. The lattice constants in xy plane depend on the angle.

They are related by $a=L/(\cos(\alpha/2))$ and $b=L/(\sin(\alpha/2))$, respectively. The photonic crystal template has a lattice constant along the z direction $c=\lambda/(2\sin^2(\theta/2))=L(\cot(\theta/2))$. If the sample rotation angle is 90º, we have a=b. Thus the 3D structure has a face-centered-tetragonal (FCT) or FCC symmetry. If the angle α is less than 90º, a face-centered-orthorhombic ($a\neq b\neq c$) or FCT ($a\neq b=c$) structure is formed in the photoresist.

Contrary to an intensity (amplitude) mask, the laser beam travels through a phase mask and accumulates an additional phase relative to light that travels through the air gap. However, a phase mask has much larger diffractive efficiency than an amplitude mask. This property enables those periodic structures have enough contrast ratio to the background in the photoresist polymerization.
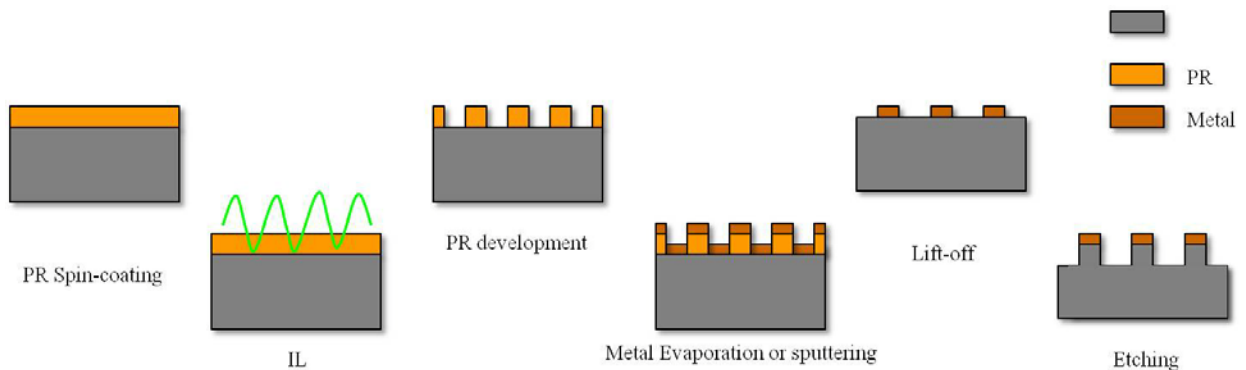
Figure 3.4 Scheme of the semiconductor processes for 1D phase mask fabrication.

The fabrication technique of 1D phase mask has been demonstrated by H. Jiang etc in 1999 [56], as Fig.3.3 shown. EBL technique has been used to pattern fine gratings in Si substrate. Then an inversed elastomeric mask is obtained by casting a layer of silicon-based organic Polydimethylsiloxane (PDMS) on the substrate. After curing and peeled off from the master mold, the elastomeric mold is used as a mask again in the photolithography process to reproduce a photoresist phase grating on glass substrate. The phase grating has high quality surface and profile but the semiconductor processes it required are costly, laborious and time-consuming. Furthermore, it needs a prototype mask with high resolution in EBL process for the parent mold fabrication.

3.2.3 Phase mask: thickness modulated DOE
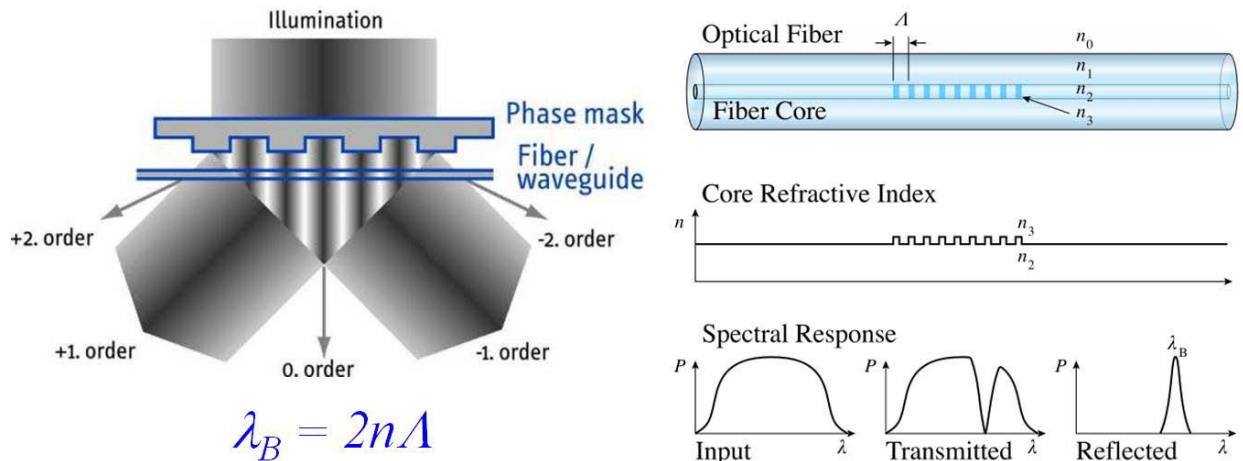
Figure 3.5 Phase mask lithography for fiber Bragg grating inscription. (Courtesy by Wikipedia [57])

One of the most effective methods for inscribing Bragg gratings in photosensitive fiber is the phase masks technique [58, 59]. This method employs a DOE to spatially modulate the UV writing beam.

Generally, phase masks may be formed either holographically or by EBL. One of the advantages of the EBL over the holographic technique is that complicated patterns can be written into the mask's structure such as quadratic chirps and patterns. The phase mask technique for writing fiber gratings has the advantages over the traditional holographic method because of its simpler writing setup and more reproducible characteristics. Specifically, the utilization of phase mask relaxes the strict requirement on the coherence of a UV source.

3.2.4 Lab made multi-dimensional phase grating
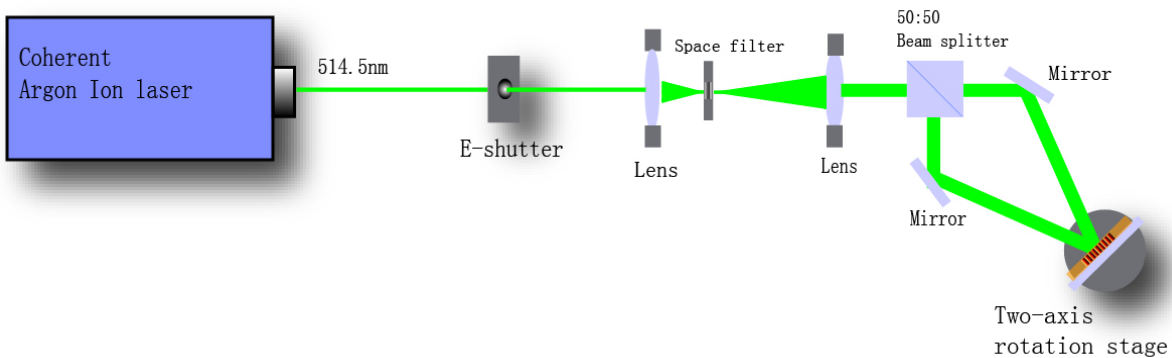
Figure 3.6 Experimental setup for phase masks holographic fabrication.

Here we demonstrate the holographic fabrication of a phase mask. The experiment setup is based on the principle of a Mach-Zehnder interferometer. As shown in Fig.3.6, two coherent beams were cleaned, collimated, separated and focused back into the same photoresist region to produce interference patterns directly. The pattern recorded is a series of parallel fringes with sinusoidal profiles. Thus we obtain the phase grating made of photoresist. This phase grating has refractive index difference between photoresist (n=1.67 at 514.5nm) and air gap, which can produce coherent three beams output when is used as a mask. This approach simplified the previous process and can

be applied into more complicated fabrication. If we do multiple exposures and rotate the receiving photoresist between each exposure, we can get phase mask with higher dimension. In next three chapters we will describe some concrete experiment steps to holographic fabricate those phase masks and use them for the HL fabrication of complex photonic crystal templates.

Overall, the optical diffractive elements are designed to avoid the alignment complexity and inaccuracies due to differences in the optical path length and angles among the interfering beams as well as vibration instabilities in the optical setup. They provide great convenience in the HL. Meanwhile, the current DOEs, such as beam splitter, mirrors, prisms and phase masks, can be used to generate pattern with all fourteen Bravais lattice in the space groups [43]. Clearly, there is a need to establish a better understanding of the relationship between the resulting symmetries and the beam parameters.

4.0   PHASE MASK LITHOGRAPHY TECHNIQUES IN 3D PHOTONIC CRYSTAL FABRICATION

4.1   DIFFRACTION PATTERN OF PHASE GRATING

It is well known that a 1D phase mask can generate three beam interference patterns, which has a 2D log-pile structure. The structure is polarization dependent of the incident EM wave thus lacks completeness of bandgap required for photonic communication. Previous researchers have proposed a method of building a 3D structure using two orthogonal 1D phase masks. The beams that propagate through two phase masks will have two log-pile patterns recorded inside the photoresist. If well controlled, a 3D woodpile structure may be piled up by the log-pile structure. However, addition diffractions occur. The distance between two phase masks can also bring unwanted phase delay, which is difficult to adjust in practice. Our solution consists of multiple exposures through one 1D phase mask, which is spatially shifted between exposures, demonstrating a new approach for controllable 3D woodpile structure fabrication.

36
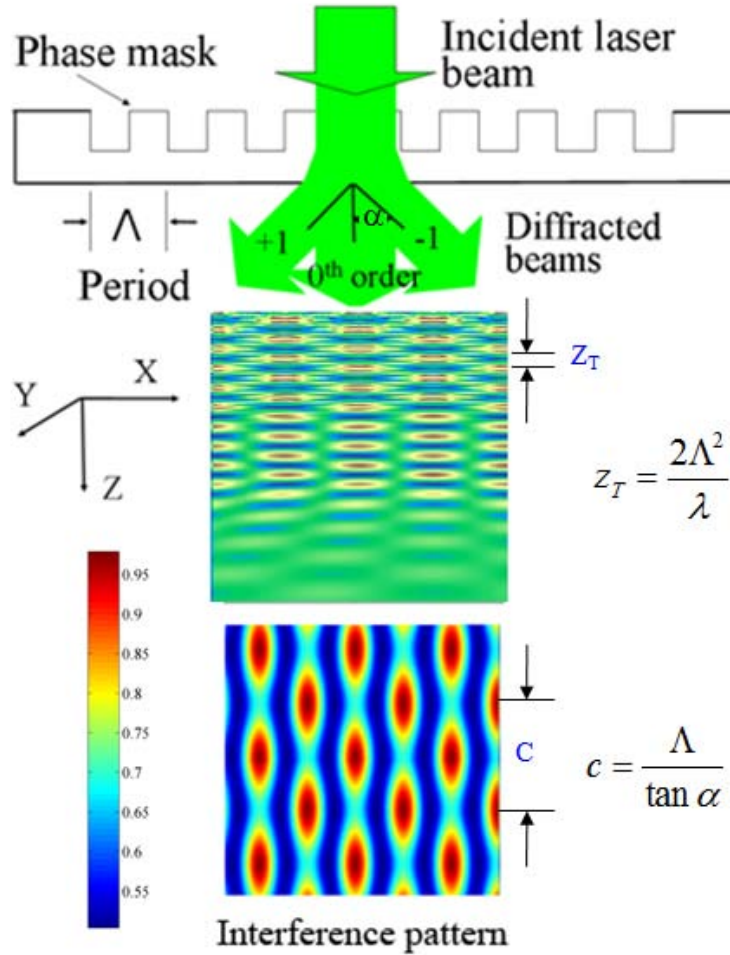
Figure 4.1 Diffraction patterns of normal incident beam through a 1D phase grating. Talbot effect exists at near field and interference pattern generates at far field. All HL in this paper record the diffraction pattern at far field.

When a plane wave is transmitted through a grating or other periodic structure, the resulting wave front propagates in such a way that it replicates the structure at multiples of a certain defined distance, known as the Talbot length. The Talbot effect is a near field diffraction effect that has been observed both with light and with atom optics [60]. An existing periodic structure can be used in conjunction with light waves or atom waves to create a replica of the structure a Talbot length away. However, the details of the Talbot effect bring out the most

interesting possible applications. Exactly halfway between these locations, the Talbot effect reproduces the structures with half the spatial period of the original structure. The Talbot effect will produce smaller fractional revivals under perfect conditions.

4.2   1D PHASE MASK - WOODPILE 3D STRUCTURE

4.2.1   Pattern transformation

Here we demonstrate the fabrication process of 3D woodpile photonic crystals template, which can have orthorhombic or tetragonal structure depending on the rotational angle. Furthermore, the elongation in the z-direction can be compensated by rotating phase mask by an appropriate angle, which increases the lattice constant in the other direction. Theory predicts that the optimized rotation angle of a phase mask can achieve up to a 50% increase in PBG compared with those formed by two orthogonally oriented phase masks.
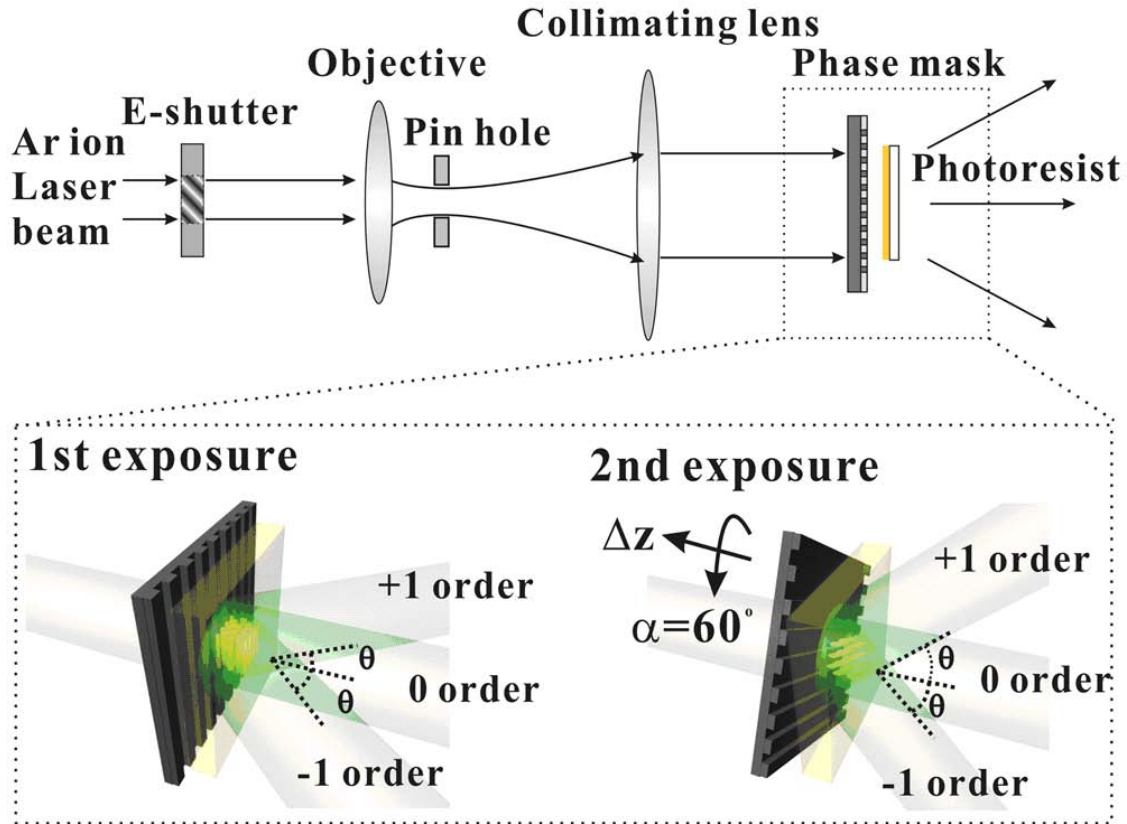
Figure 4.2 Experimental setup for 3D photonic crystal template fabrication. Zoom in view is the schematic sketch of the double exposures procedure.

In next step we describe how to construct an interconnected photonic crystal with woodpile symmetry. The interference pattern for a single exposure through a phase mask is a 2D log-pile structure, which is periodic in the z direction as well as in the x (or y) direction, as shown in Fig. 4.2. If we do a second exposure to record another log-pile structure on the same region, with appropriate relative rotation and shifting, we can have a 3D woodpile structure, which has periodic structure in all x, y and z directions, as shown in Fig. 4.3 It demonstrates a simulated structure from the dual-exposure procedure. Similar to how the photoresist reacts to illumination, the structure represents the receiving laser intensity distribution, i.e. the interference region, in the negative photoresist. The boundary of the 3D pattern is defined by

setting a threshold value. The regions with intensity lower than the threshold value are removed and the regions with intensity equal and greater than the threshold value are sustained. Thus the photoresist records the interference pattern and can be visualized after development.
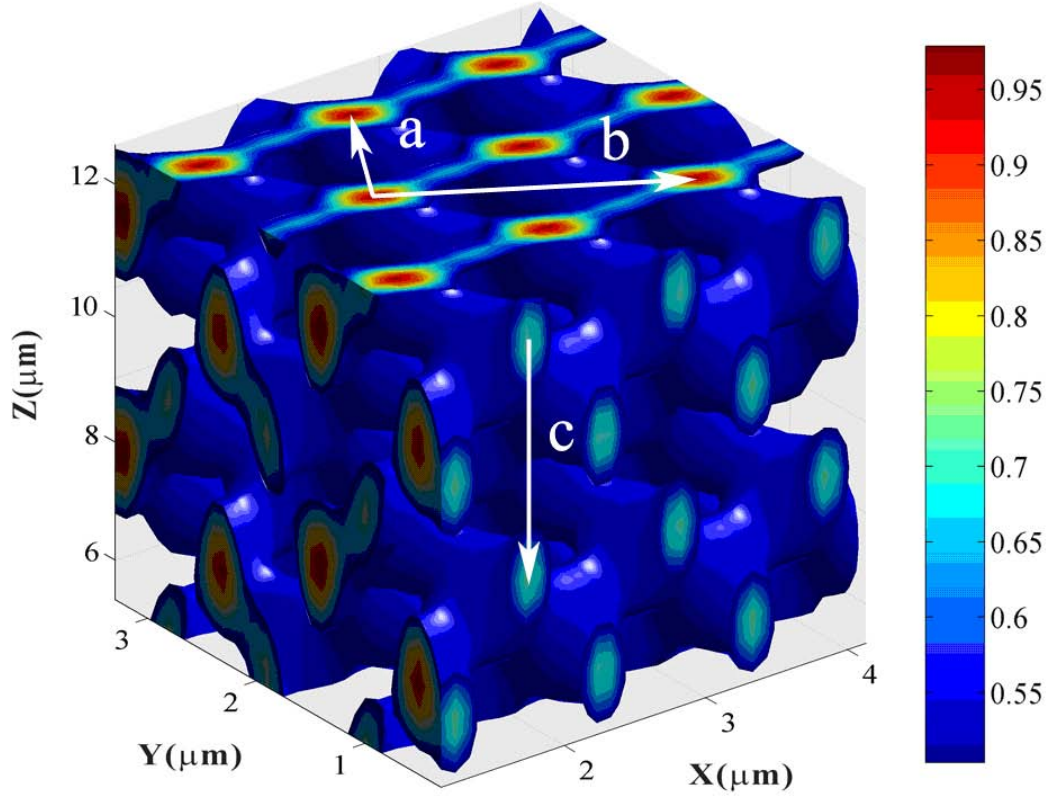
Figure 4.3 Simulated 3D woodpile structure generated by double exposures. The rotational angle of phase mask is 60°. The scale bar shows the accumulated laser energy density upon two exposures.

Theoretically, the rotation of the interference pattern can be regarded as replacing the wave vector k of the diffractive beams, by a coordinate transform with rotation angle α;

$$\vec{k}_1 = (k\cos\theta)z - [(k\sin\theta)\cos\alpha]x - [(k\sin\theta)\sin\alpha]y \qquad (4.1a)$$

$$\vec{k}_2 = (k\cos\theta)z - [(k\sin\theta)\cos\alpha]x + [(k\sin\theta)\sin\alpha]y \qquad (4.1b)$$

$$\vec{k}_3 = (k\cos\theta)z \qquad (4.1c)$$

while the spatial movement of the pattern can be induced through the phase shift of interfering beams. When a phase difference (ρ_i-ρ_j) is introduced between interference beams, the interfering term I_{int} in Eq.(4.2) becomes

$$I_{int} = \sum_{i<j}^{3} \vec{E}_i \bullet \vec{E}_j \cos[(\vec{k}_i - \vec{k}_j) \bullet \vec{r} + (\rho_i - \rho_j) + (\delta_i - \delta_j)] \tag{4.2}$$

Such a phase difference between laser beams will translate the interference pattern by r_s as described by,

$$I_{int} = \sum_{i<j}^{3} \vec{E}_i \bullet \vec{E}_j \cos[(\vec{k}_i - \vec{k}_j) \bullet (\vec{r} + \vec{r}_s) + (\delta_i - \delta_j)] \tag{4.3}$$

where the translation r_s is determined by $(k_i-k_j)\cdot r_s=(\rho_i-\rho_j)$. In general, the initial phase difference δ_i -δ_j is a constant if the laser beams are mutually coherent. It will shift the interference pattern relative to the one generated with (δ_i-δ_j)=0. But the initial phase difference will be the same for two exposures. The interference pattern generated by the second exposure needs to be shifted relative to the first one to fabricate the woodpile photonic crystal. The shifting is produced through the extra phase shift of (ρ_i-ρ_j). Specifically, the initial phase difference is zero if all diffracted beams are generated through a single DOE. Then the final 3D structure can be expressed by adding up the interfering terms I_{int} for two exposures, normalizing and setting proper threshold isosurface values.

Experimentally, the basic approach utilized to fabricate an interconnected periodic polymeric structure is the double exposure of photosensitive material to three interfering laser beams generated by a 1D phase mask as shown in Fig. 4.2. A linearly polarized beam from an argon ion laser at 514.5nm is expanded, collimated, and passed through a phase mask to produce two 1st order and one 0th order diffracted beams (intensity ratio 1:5). A layer of photoresist on a silicon wafer is first exposed to the interference of the three laser beams. Thus, a spatially

41

modulated chemical change in the photoresist is produced. A second rotated and translated phase mask is then used to induce a second set of spatially modulated chemical changes in the photoresist. The orientation of the second interference pattern is controlled by the orientation angle α of the second phase mask with respect to the first one. To form an interconnected 3D woodpile structure, the phase mask was shifted along the z direction (c-axis) by a distance $r_s=(0, 0, \Delta z)$ for the second exposure. This shift has a significant impact on the size of overlap between the two interference patterns and consequently on the size of the bandgap formed in the final structure. A translation of $\Delta z= 0.25c$ of the second interference pattern along the c-axis yields an optimized fully-interconnected woodpile structure as shown in Fig. 4.3. High-precision motion stages were used to control the movements of the phase masks with ±100nm accuracy. By controlling the rotational angle and the relative shift of the phase mask along the optic axis, both orthorhombic and tetragonal photonic crystal structures were formed. Fig.4.3 shows a simulated face-centered orthorhombic photonic crystal structure formed by rotating the phase mask by $\alpha=60^o$ between two exposures. The lattice constants (a, b, c) labeled in Fig. 4.3 are determined by the angle of diffraction θ of the 1st order beams in the photoresist and by the angular rotation of the phase mask α as $(L/(\cos(\alpha/2)), L/(\sin(\alpha/2)), $ and $L(\cot(\theta/2))$, respectively, where L is the grating period given by $L= \lambda/\sin\theta$, and λ is the laser wavelength in the photoresist material.

4.2.2   Band diagram of woodpile photonic crystal

The woodpile-type photonic crystal template will be converted into high refractive index materials using the approach of CVD infiltration in order to achieve a full bandgap photonic crystal [47]. We calculated the PBG for converted silicon structures where 'logs' are in air while

the background is silicon. The calculation has been performed for photonic structures formed with various interference angle θ and rotation angle α. Fig. 4.4 (left) shows the first Brillouin surface of the face-centered-orthorhombic lattice. Coordinates of high symmetric points on the Brillouin surface varies with different structures. MIT Photonic-Bands Package was used to calculate the PBG of the converted silicon structure. Fig. 4.4 (right) shows the photonic band structure for the converted silicon woodpile-type structure with c/L=2.4 and α=51° (the dielectric constant of 11.9 was used for silicon in the calculation. We would like to clarify that the λ_{photon} in the y-axis label of the Fig. 4.4 (right) is the wavelength of photons in the photonic band, not the wavelength of the exposure laser. The band structure shows that a photonic full bandgap exists between the 2nd and 3rd bands with a bandgap size of 8.7 % of the gap central frequency.
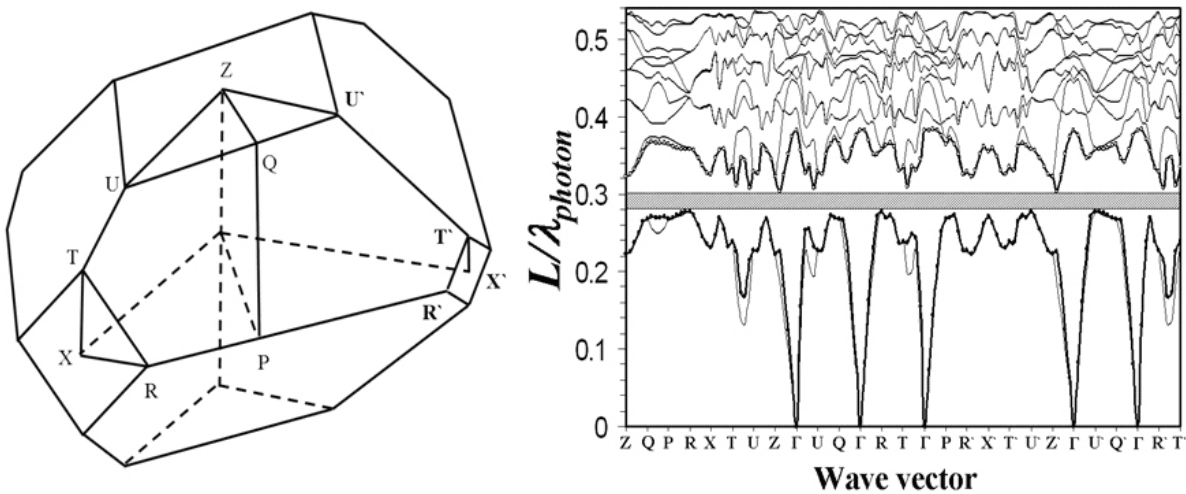
Figure 4.4 (left) First Brillouin surface of face-centered-orthorhombic lattice; (right) photonic band structure for an orthorhombic photonic crystal. λ_{photon} is the wavelength of photons in the photonic band.

4.2.3 PBG width modulation with crystal parameters
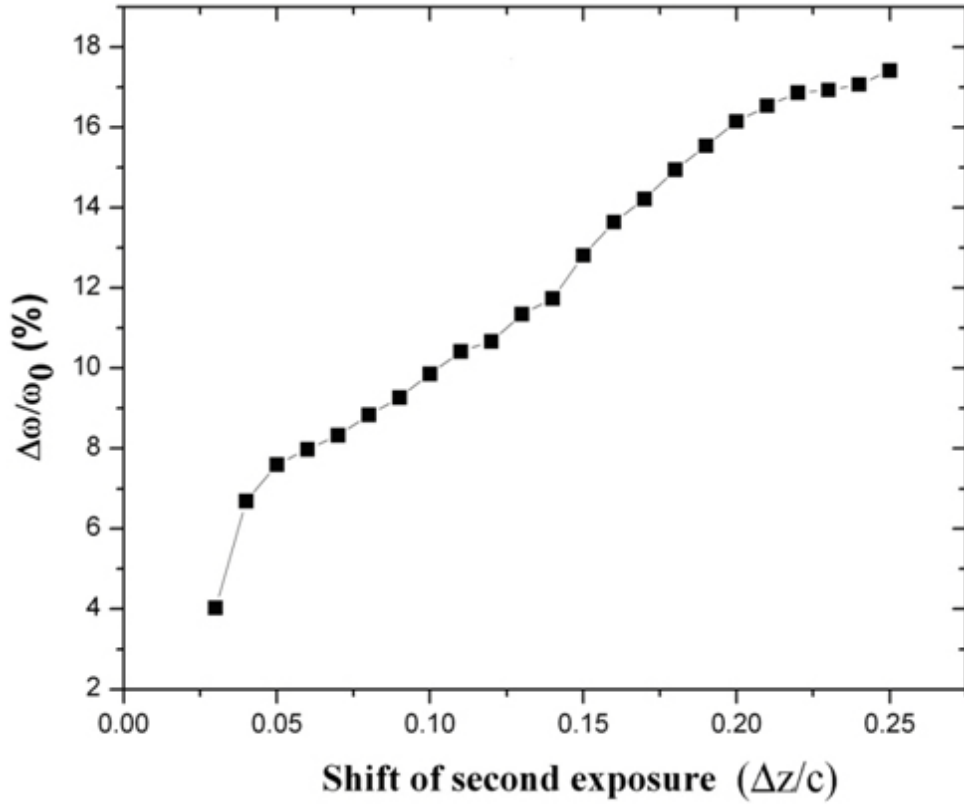
Figure 4.5 PBG as function of the phase mask displacement Δz between two exposures. The phase mask rotational angle α is 60°. Insets are the first Brillouin surface and photonic band diagram for the face-centered-orthorhombic structure.

The significance of the overlap between the two alternating high-intensity stacks controlled by the translation Δz of the second phase mask along the optical axis is depicted in Fig. 4.5. The relative bandgap size is measured from the bandgap diagram from Fig. 4.4 and defined by the ratio of central frequency and the frequency range of the bandgap. From Fig. 4.5 we can see that a global bandgap of 4% exists in structures with α=60° and Δz=0.03c. The maximum PBG appears at Δz=0.25c, where the 2nd log-pile pattern moves to a location closest to the 1st log-pile

pattern, symmetrizing the whole 3D woodpile structure. In structures where $\Delta z \leq 0.03c$, the width of the bandgap reduces rapidly and eventually vanishes. A maximum bandgap of 17% was achieved at a shift $\Delta z = 0.25c$.

To study the dependence of the size of the bandgap on α, PBG calculations were performed with various c/L ratios as shown in Fig. 4.6. Since all the laser beams come from the same half-space, the interference pattern generated will be elongated along the c-axis due to relatively small interference angles. This elongation, along with a rotational angle of 90°, causes the lattice constant c to be larger than a and b, yielding a FCT structure. When the phase mask's rotational angle decreases from 90°, the lattice constant b increases, while a decreases; in effect reducing the photonic crystal structure to a lattice with orthorhombic symmetry. A small phase mask rotational angle α can transfer the lattice back into tetragonal again when the lattice constant b is equal to c. When the value of b approaches that of c, the structure becomes more symmetric and the bandgap increases. From simulation, we found that the maximum bandgap occurs when the structure has the highest possible symmetry. For relatively small c/L ratios, where c approaches a and b, and $\alpha = 90°$, the widest bandgap is produced. For larger c/L ratios, the maximum bandgap occurs at a rotational angle $\alpha \neq 90°$. Fig. 4.6 also illustrates the rotation angles α that maximize the bandgap for structures with a large c/L values. When c is larger than 1.9L, a small rotational angle of the phase mask is required to maximize the bandgap. For c/L=2.0, a 60° rotational angle maximizes the PBG. Maximizing the bandgap for structures with c/L ratios larger than 2 requires less than 60° angular displacements. For this c/L ratio, varying the rotation angle from 90° initially results in a drop in the width of the gap followed by an increase. This is consistent with the symmetry transformation of the photonic structure, changing from tetragonal symmetry to orthorhombic symmetry then back to tetragonal symmetry.

45
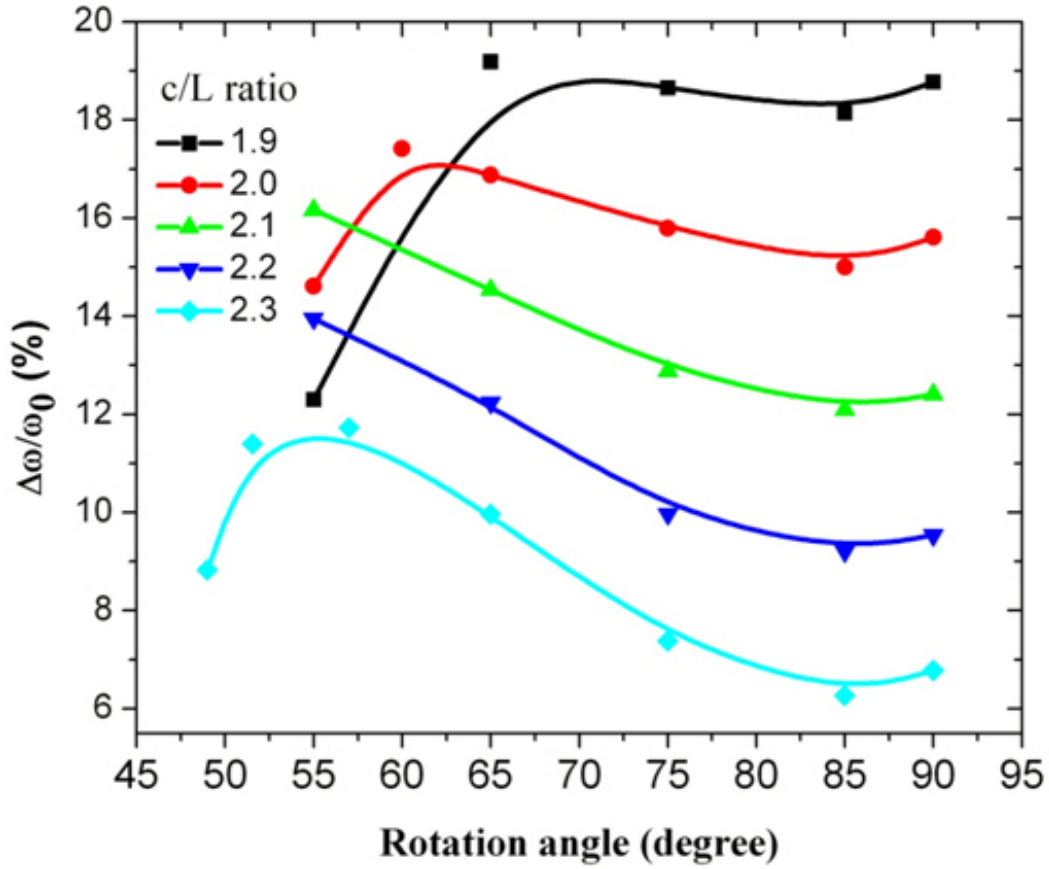
Figure 4.6 PBG as a function of the phase mask rotational angle α.

Fig. 4.7 shows the optimum bandgap size in FCT photonic structures which is formed with the rotation angle α=90º and in face-centered-orthorhombic structure where α≠ 90º, under different beam interference geometries. When c/L is small (beams have a larger interference angle), a rotation angle of 90º is preferred in order to have a larger bandgap. However if c/L is larger than 2.0, then the face-centered-orthorhombic structure is preferred for a larger bandgap. At c/L=2.3, the optimum bandgap size is 11.7% of the gap central frequency for a face-centered-orthorhombic structure formed with a rotation angle near 55º. While the FCT structure formed with α=90º has a gap size of 6.7%.
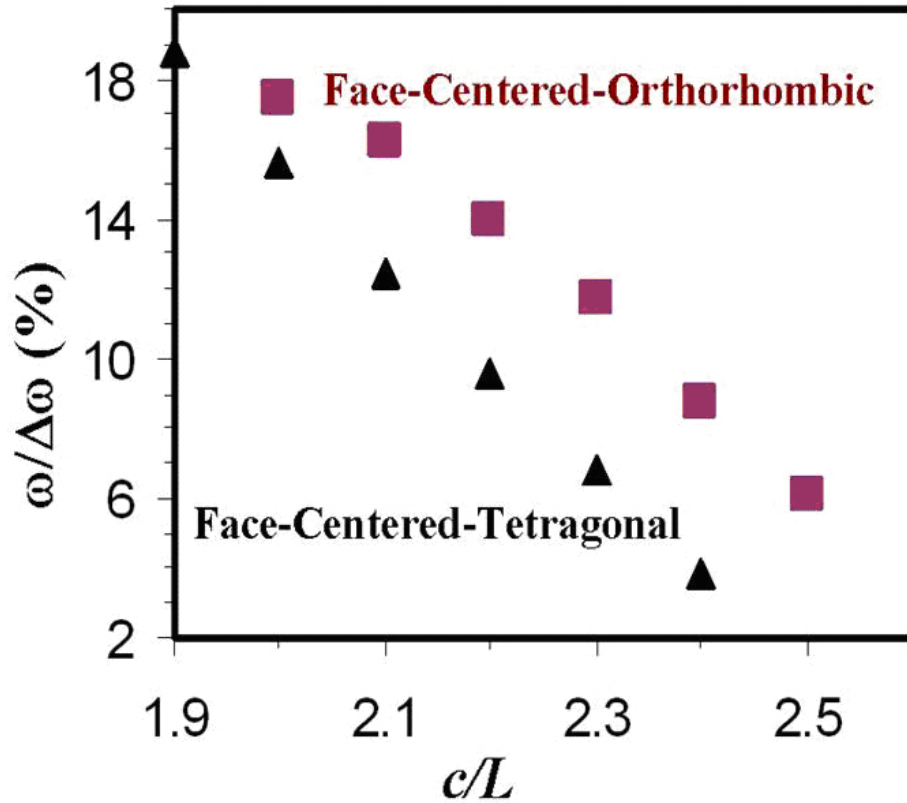
Figure 4.7 PBG size in FCT structures (=90º) and in face-centered-orthorhombic structures (< 90º) for various structures with a different c/L value.

To demonstrate the feasibility of the proposed fabrication technique, both orthorhombic and tetragonal structures were recorded into a modified SU8 photoresist. Utilizing the phase mask method a number of photonic structures can be generated; however there are some practical issues in realizing a photonic structure with a full PBG. Fig. 4.7 shows that a PBG exists in structures with smaller c/L values. Because c/L=cot(θ/2), a bigger interference angle is required in order to generate an interference pattern for a structure with a full bandgap. When the photoresist is exposed into an interference pattern, the interference pattern recorded inside the photoresist will be different from that in air. In the case of c/L=2.5, an interference angle θ=43.6º is required, which is greater than the critical angle of most of photoresist.

4.2.4 3D structure in photoresist

In order to expose the photoresist to an interference pattern formed under a bigger interference angle, a special setup is arranged for the phase mask and the photoresist as shown in Fig. 4.8 (left). The photoresist is placed on the backside of the phase mask with the contact surface wetted with an index-match mineral oil. The design of the phase mask is modified correspondently. As a proof-of-principle, we show in Fig. 4.8 (right) Scanning Electron Microscope (SEM) of woodpile-type structures in SU8 photoresist formed through the phase mask based HL. An Ar ion laser was used for the exposure of 10 μm thick SU8 photoresist spin-coated on the glass slide substrate. The photoresist and phase mask were both mounted on high-precision Newport stages. Both the phase mask and photoresist were kept perpendicular to the propagation axis of the incident Ar laser beam.
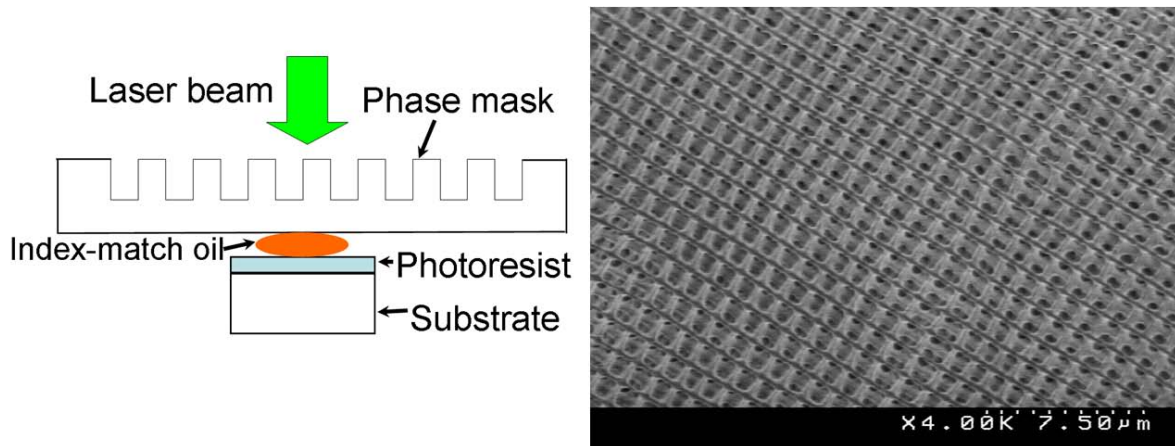
Figure 4.8 (left) an arrangement of the phase mask and the photoresist. The interface between the backside of the phase mask and the photoresist is wetted with an index-match fluid; (right) SEM top-view of an orthogonal woodpile-type structure in SU8 photoresist formed through the phase mask based HL.

The photoresist solution was prepared by mixing 40 gram SU8 with 0.5 wt % (relative to SU8) of 5,7-diiodo-3-butoxy-6-fluorone (H-Nu470), 2.5 wt% of iodonium salt co-initiator (OPPI), and 10 ml Propylene Carbonate to assist the dissolution [6]. Due to the large background energy presented in the generated interference pattern (53% of 0th order), the photoresist solution was further modified by the addition of 20 mol percent Triethylamine [61]. Subsequent exposure to light generates Lewis acids that are vital in the crosslinking process during post exposure bake. The addition of Triethylamine, acting as an acid scavenger, allowed the formation of an energy gap which prevented the polymerization process in locations exposed below the energy threshold. The substrates utilized for crystal fabrication were polished glass slides cleaned with Piranha solution and dehumidified by baking on a hot plate at 200 ºC for 20 min. Each substrate was pre-coated with 1µm layer of Omnicoat to enhance adhesion. The SU8 mixture was spin-coated onto the pre-treated substrate at speeds between 700 and 1500 rpm; resulting in a range of thicknesses from 25 to 5 µm. Pre-bake of SU8 films was performed at a temperature of 65 ºC for about 30 min. The prepared samples were first exposed under 500mw illumination for 0.9 s using the first phase mask. A second phase mask, which was rotated by α about the optic axis and translated by Δz with respect to the first one, was then used for an additional 0.9 s exposure. The samples were post-baked at 65 ºC for 10 min and 95 ºC for 5 min and immersed in SU8-developer for 5 min.
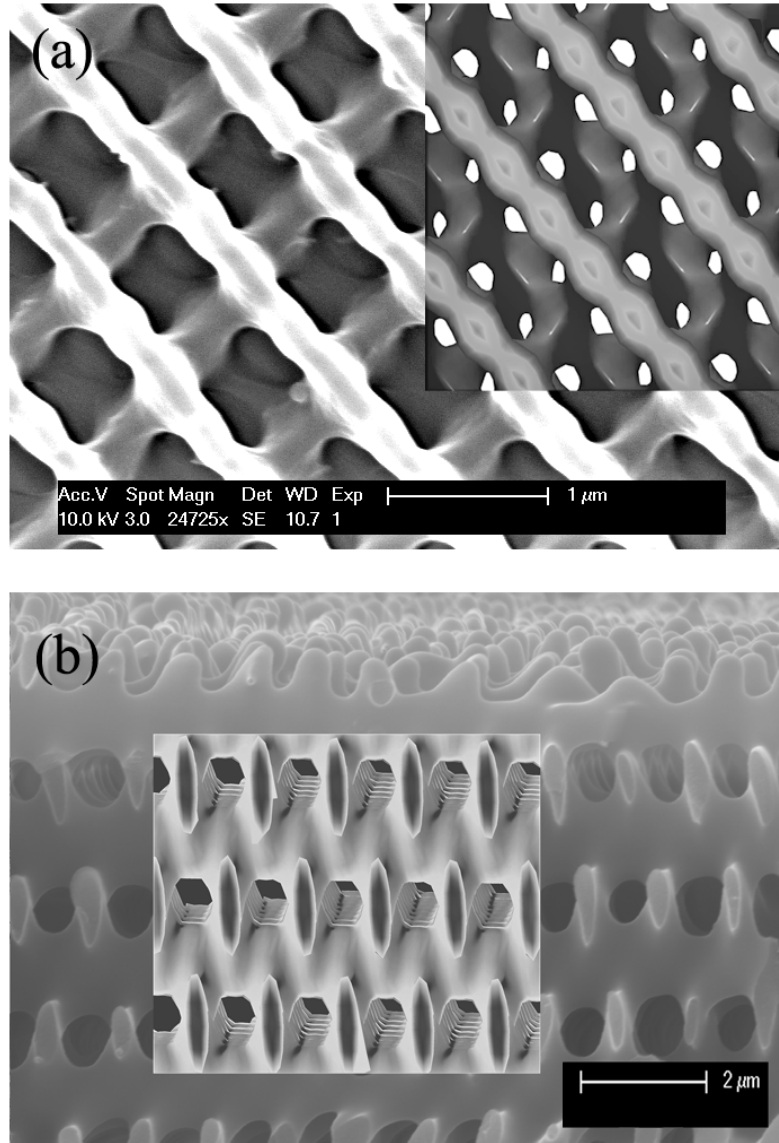
Figure 4.9 (a) A SEM top view picture; and (b) a SEM side view picture of a woodpile orthorhombic structure recorded in SU8 with α=60º. Simulated structures are inserted.

Fig. 4.9(a) shows an SEM top view picture of a woodpile orthorhombic structure recorded in SU8 with an α of 60º. The inset of the same figure details the predicted structure from simulation. The 3D span of the structure visible in Fig. 4.9(b) was also imaged by SEM. The layer-by-layer, woodpile nature of the structure is clearly demonstrated. The overlapping

and cross-connection of neighboring layers ensures a stable formation of 3D structures for further processing. From Fig. 4.9 (a) and (b), we measured in the SEM the lattice constants to be b=1.3 μm and c=3.4 μm. The elongation in the z-direction was thus compensated by the 60º rotation, compared with b=1.06 μm and c=6.13 μm in the structure generated by two orthogonally-oriented phase masks with similar period used in this work.

In summary, we demonstrate the fabrication of 3D photonic crystal templates in SU8 using phase mask based HL technique. Both face-centered-orthorhombic and FCT woodpile-type photonic crystals have been fabricated. The usage of phase mask dramatically simplified the optical setup and improved the sample quality. The structure and symmetry of the photonic crystals have been demonstrated by controlling the rotational angle of a phase mask to compensate the structural elongation in z-direction in order to enlarge the PBG. PBG computations have been preformed optimally on those woodpile structures with α between 50º to 70º as well as traditional 90º rotation. Our simulation predicts that a full bandgap exists in both orthorhombic and tetragonal structures. The study not only leads to a possible fabrication of photonic crystals through HL for structures beyond intensively-studied cubic symmetry but also provides a blueprint defining the lattice parameter for an optimum bandgap in these orthorhombic or tetragonal structures.

4.3   2D PHASE MASK – DIAMOND-LIKE 3D STRUCTURE

In this section we will demonstrate our work to extend the phase-mask approach for holographic 3D structure fabrication from 1D phase mask to 2D phase mask. We used the holographic

method introduced in Chapter 3 to fabricate the photoresist 2D phase mask. The flexibility of 2D phase mask design enables the construction of multiple-beam interference patterns for the fabrication of complex 3D periodic structure such as diamond-like structures [45]. As we all know, diamond-like photonic crystal structures possess the largest PBG among all possible photonic crystal but hard to synthesize. This flexibility is demonstrated by fabricating the diamond-like structures in SU8 photoresist using a lab-made 2D phase masks as the DOEs.

4.3.1　2D phase mask holographic fabrication

The 2D phase masks used in this experiment were fabricated in a thin negative-tone SU8-2035 photoresist. The photoresist was spin-coated on a glass substrate with a thickness of 2 μm. After spin-coating, the sample was prebaked at 65 ^{0}C for 5 min and 95 ^{0}C for 3 min before receiving the laser exposure. The source beam from an Argon Ion laser was collimated and split into two coherent linearly polarized beams with equal intensity using a beam splitter. Two laser beams were recombined by a pair of mirrors and overlapped across the photoresist with a certain angle to produce an interference pattern. The polarizations of two interference beams are parallel to the surface of the photoresist. The photoresist solution was sensitized for 514.5 nm laser wavelength by adding 0.25 wt% H-Nu470 and 2.5 wt% OPPI photo-initiators. After the first exposure, the sample stage was rotated along the normal direction of the sample by angle α and received a second exposure. Then the samples were post-baked at 65 ^{0}C for 10 min and 95 ^{0}C for 5 min followed by photoresist development for 5 min. After that, the phase mask was hardened by baking at 120 ^{0}C for 10 min. Figures 4.10 (a) and (b) show the SEM and simulated surface topography in SU8 resulting from double laser exposures with 90° rotation angle between

exposures. Figure 4.10(c) shows the diffraction pattern produced by the phase mask. The diffraction efficiency depends on the thickness of photoresist, the exposure and development times, and the rotational angle.
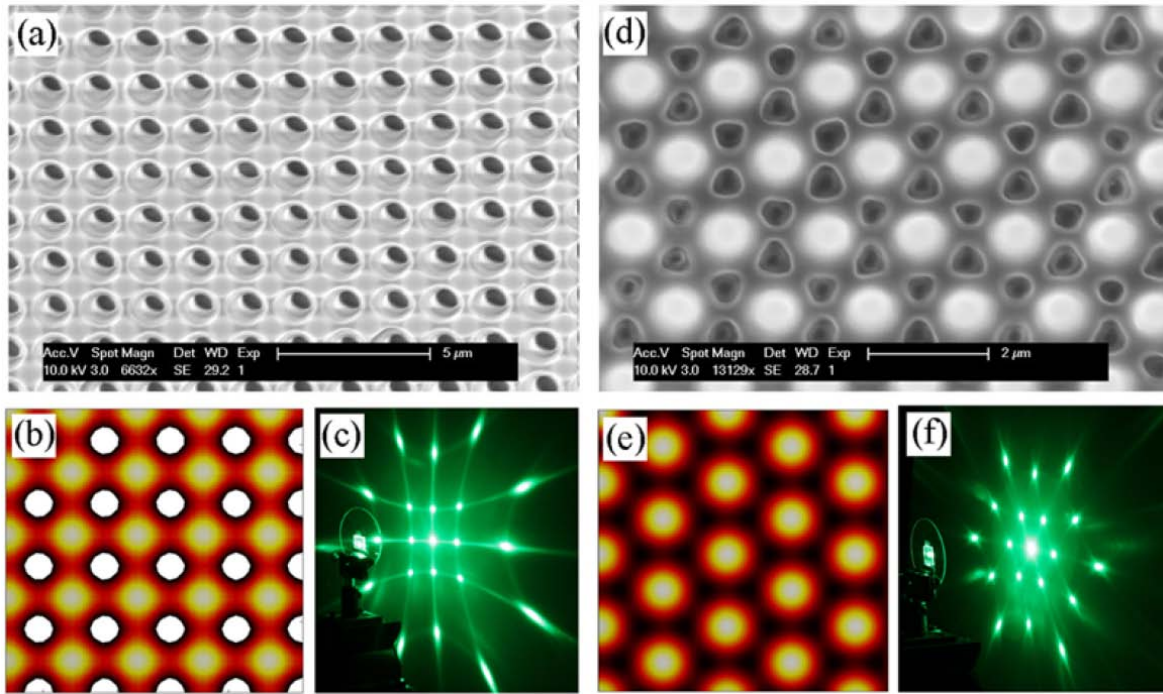
Figure 4.10 The SEM, simulated surface and diffractive pattern of 2D phase masks made by double exposures with rotation angle $\alpha= 90^0$ (a), (b), (c) and by triple exposures with $\alpha= 60^0$ (d), (e), (f).

To produce more complex multiple-beam interference patterns, multiple laser exposures can be used to create a 2D phase mask. Figures 4.10(d) and (e) show SEM and simulated topography resulting from three laser exposures; the sample was rotated by $\alpha=60^o$ each time between exposures. The diffraction pattern produced by this phase mask is shown in Fig. 4.10(f). Its interference pattern produces a face-centered hexagonal structure.

The 2D phase mask we used for photonic crystal fabrication has typically a period of 1.1 μm. It has an orthogonal surface profile ($\alpha=90^o$) and its laser beams diffraction is schematically

shown in Fig. 4.11(a). The diffraction angle and diffraction efficiency of four 1st-order diffraction beams labeled as (1, 0), (-1, 0), (0, 1), (0, -1) were measured to be 20^0 and 10%, respectively. The four second-order diffraction beams (1, 1), (1, -1), (-1, 1), (-1, -1) had much lower diffraction efficiency at 1.5%. The 3rd and higher order beams have negligible intensities. Therefore, only the 0th and 1st order beams were used to determine crystal structures based on iso-intensity surface of the interference pattern [49]. The interference of five-beam produced by the 2D phase mask yields a FCC or FCT structure.
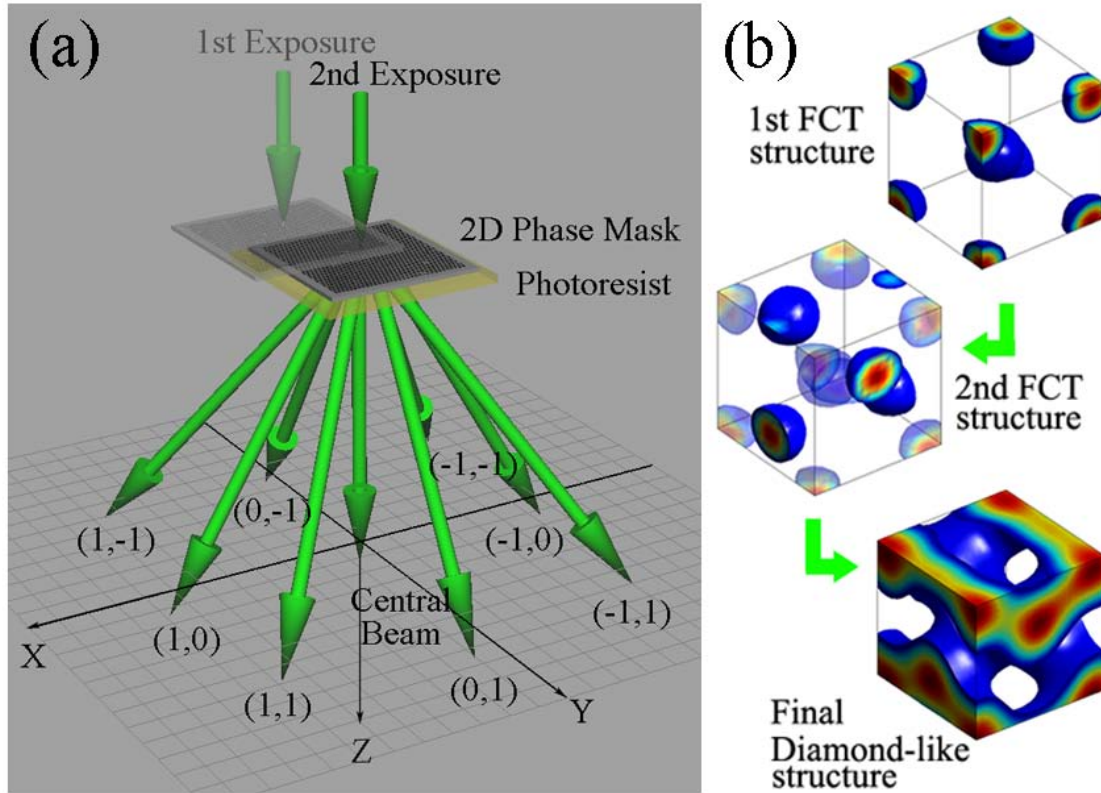
Figure 4.11 (a) Sketch of propagation of light through an orthogonal 2D phase mask. FCT pattern is generated by recording the intensity distribution of five-beam interference in SU8 photoresist. (b) Diamond-like structure constructed by double exposures with one FCT pattern shifted by $\Delta x=0.5a$ and $\Delta z=0.25c$.

4.3.2 3D diamond-like template

Figure 4.11(b) illustrates the path for lattice translation from FCT to diamond-like structures. Theoretically, the diamond-like structures can be viewed as the superposition of two FCT structures with a lattice displacement. This can be achieved by double exposures through the 2D phase mask on the same photoresist sample with phase mask displacement along the [2, 0, 1] direction of Cartesian coordinator system for a quarter diagonal length between exposures. The offsets Δx and Δz (marked in Fig. 4.11(a)) between two exposure patterns inferred from simulation are 0.5a and 0.25c respectively, where a and c are the lattice constants of the FCT structure in x and z direction. These actual precise displacements were performed by three-axis high-precision Newport motorized linear stages. The simulated iso-intensity surfaces of the 1st FCT, 2nd shifted FCT, and final superimposed structures are shown in Fig. 4.11(b).

The 3D template was fabricated in a thick SU8 film sample of 20 μm. The concentration of H-Nu 470 in photoresist solution was increased to 0.5 wt % to accelerate the photoresist cross linking. 20 molar % of Triethylamine was added into the recipe again to increase the contrast ratio of the template during the photoresist development. To avoid reaching the boiling point of Triethylamine of 89.7 ^{0}C, the prebake procedure was adjusted to one step at 65 ^{0}C for 20 min. The laser exposure dose was fixed at 100 mW/cm^{2} for both exposures. Figures 4.12(a) and (b) show SEM top view of diamond-like structures recorded in SU8. The surface feature is consistent with the simulation results of the (0, 0, 1) plane of a diamond-like structure in both inset of Fig. 4.12(a) and (c). The cross-linking between two FCT structures formed by two laser exposures produces a stable 3D template for further inversion processes to create high-index contrast structures.
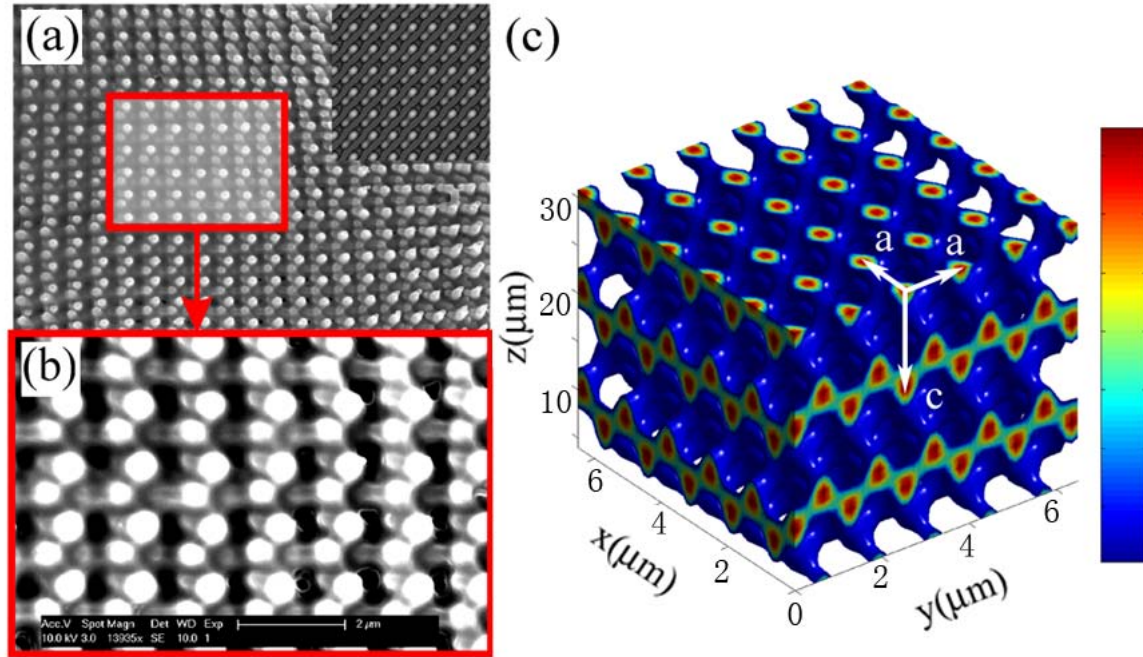
Figure 4.12 (a) SEM top view of the fabricated structure together with inserted surface simulation based on FCT pattern superposition. (b) Enlarged view of the fabricated structure. (c) Simulated interconnected 3D diamond-like structures through double exposures.

4.3.3   Optimal bandgap simulation

The PBG for the silicon inverse structures is calculated and shown in Fig. 4.13 using the MIT Photonic-Bands Package. Figure 4.13(a) shows the photonic band structure for $c/a=1.5$ for the silicon inverse structure where the dielectric constant of 11.9 is used for silicon. The optimal silicon filling fraction for diamond-like structure is approximately 18.4% while 20.5% for a FCT structure. The band structure shows that a full PBG of 27% of the gap center frequency exists between the 2nd and 3rd bands of the optimal diamond-like structure. This is in contrast to the maximal PBG of 3.8% between the 8th and 9th bands of a single FCT inverse structure with the

same c/a value. The gap size is increased by the operation of constructing the diamond-like lattice formed by double laser exposures.
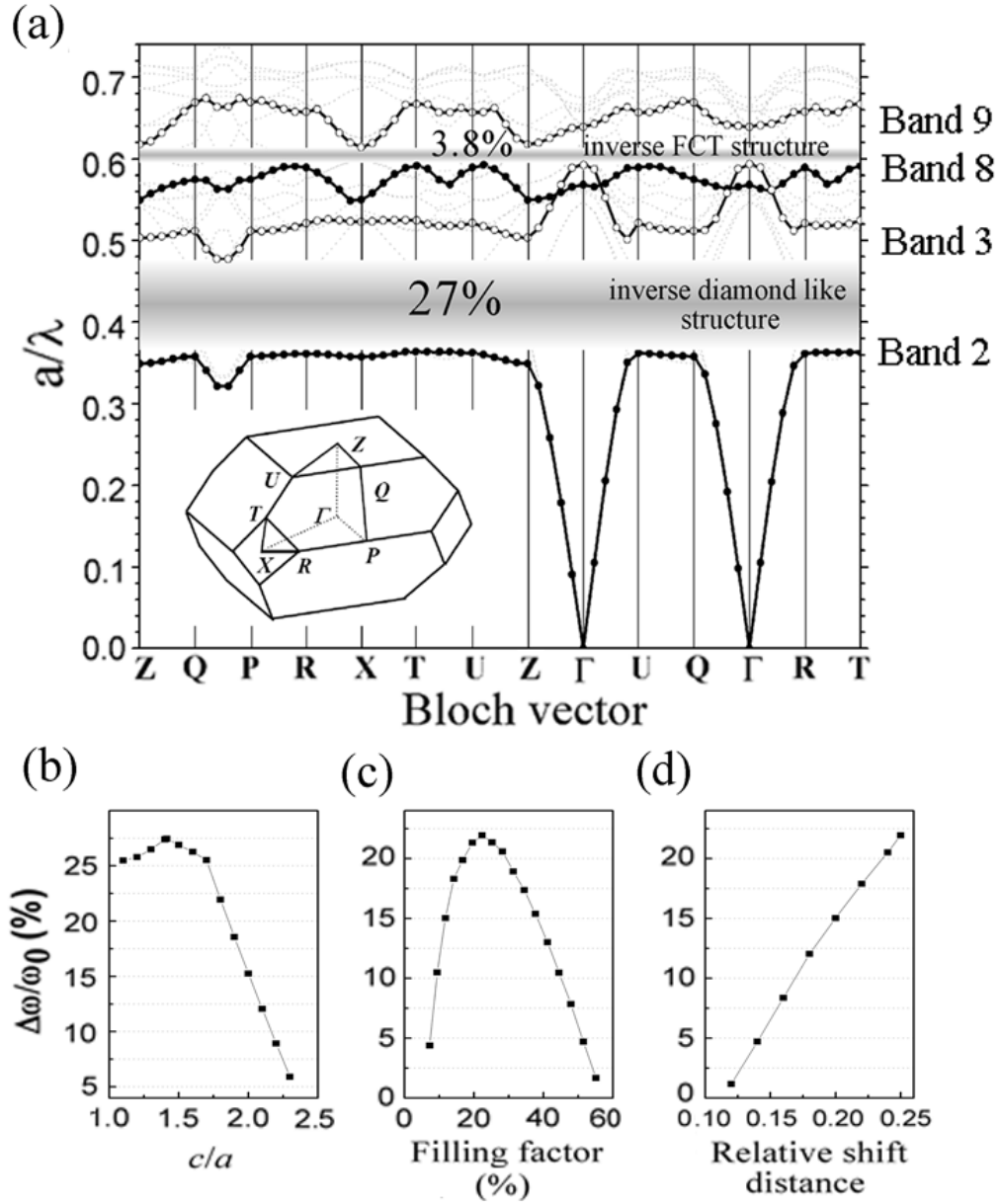
Figure 4.13 (a) Photonic band diagram for the inverse FCT structure and FCT based diamond-like structure. The left inset is the first Brillouin surface. (b), (c), (d) are the gap size as a function of c/a ratio, dielectric filling factor and relative shift distance, respectively.

The bandgap of the fabricated diamond-like structure depends on c/a ratio (the diffractive angle), the filling ratio of the structure (exposure dose) and the relative lattice shift distance. The bandgap size dependence on these fabrication parameters are shown in Fig. 4.13(b)-(d). Figure 4.13(b) indicates a need of larger diffraction angle or a close match between lattice constant c and a. A c/a ratio from 1.0 to 1.7 will maintain a bandgap larger than 20%. The bandgap is closed when the c/a is greater than 2.5. In addition, the filling fraction of the structure also impacts the bandgap, which can be controlled by laser exposure dosage and the photoresist development time. Figure 4.13(c) shows this trend for a diamond-like structure with $c/a=1.8$. The optimal dielectric filling fraction was found to be 23% for the inverse structure. In Fig. 4.13(d) the bandgap size is shown as a function of phase mask translation distance between two exposures. When the second FCT lattice is shifted away the optimum location of $(0.5a, 0, 0.25c)$ toward $(0, 0, 0)$, for the inverse structure with $c/a=1.8$, the bandgap size decreases almost linearly during the transition from the diamond-like structure to the FCT structure.

In summary, we have demonstrated a 2D phase mask approach to generate multiple coherent beams for complex photonic crystal fabrications. Diamond-like photonic crystal templates were fabricated in SU8 by double exposures with lattice superposition using this approach. The utilization of the 2D phase mask simplifies the fabrication configuration in multi-beam HL for complex 3D optical fabrication.

4.4 TWO-LAYER PHASE MASK – DIAMOND-LIKE 3D STRUCTURE

In this section we will introduce a two-layer phase mask, i.e. a mask with phase gratings at two different planes, as the DOE in the consequent HL 3D fabrication. The phase mask is designed with similar holographic fabrication principle as we used before. However, extra step are introduced before the grating development. If designed properly, this single optical element can replace a complex optical setup to generate a desired interference pattern.

Although the adaptation of single DOE has significantly simplified the optical setup to generate three or five interfering laser beams, the formation of diamond-like or woodpile structures requires a well-controlled π-phase difference among diffractive laser beams. Chan, etc. have proposed theoretically to "lock" the required phase shift in the mask by fabricating 1D grating in two layers on the same substrate [62, 63]. The optimized phase shift is determined by the vertical spatial separation between two gratings. Illuminating the phase mask with a normally incident beam produces a five-beam interference pattern which can be used to expose a suitable photoresist and produce a photonic crystal template. One can carefully design the phase mask to manipulate the relations of the interfering beams and thus it can be used to produce photonic crystal templates with diamond-like structures. However no experimental fabrication of such an optical phase mask has been reported to date.

4.4.1 Liquid crystal phase separation approach

The first mask fabrication approach we demonstrate is to make multi-layer phase mask on a single substrate. The fabricated optical phase mask consisting of two orthogonally-oriented

gratings has high diffraction efficiencies and generate five-beam interference pattern with a phase relation among the interfering beams. The photonic crystal template is fabricated by exposing a photoresist to the five-beam interference pattern.

One laser beam was expanded and separated into two beams using a beam-splitter. A parallel fringe is formed when two laser beams overlap. The spacing Λ between the dark (or bright) fringes is determined by the laser wavelength and interference angle θ by the relationship of $\Lambda=\lambda/(2sin\theta)$. When a photoresist is exposed to the interference pattern and developed, it forms a 1D grating on the substrate. In order to protect the grating formed after laser exposure, liquid crystal was employed to mix with the photoresist. Their inherent phase separation characteristic played a key role in the fabrication of the integrated phase mask described as follows.
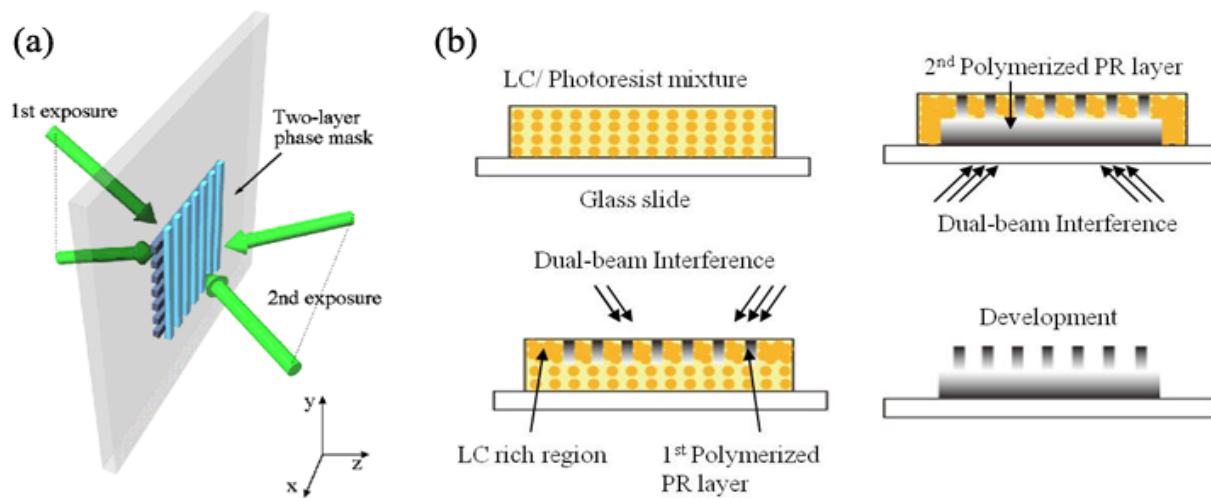
Figure 4.14 Schematic of two beam interference (a) for the formation of optical phase mask consisting of two orthogonally oriented gratings in a photoresist mixed with liquid crystal molecules (b).

The photoresist mixtures were similar to a reported formulation (without fatty acid) containing the following components in the specified weight concentrations: dipentaerythritol penta/hexaacrylate (DPHPA) monomer (Aldrich, 65%), BL111 liquid crystal (EMD Chemicals, 25%), a photo initiator rose bengal (0.3%), co-initiator N-phenyl glycine (NPG, 0.5%), chain

extender N-vinyl pyrrolidinone (NVP, 9.2%). For the phase mask fabrication, the mixture was spin-coated over a transparent glass slide (Corning) with a typical speed of 4000 rpm for the phase mask fabrication. The thickness of the sample is determined by the spin-coating speed. For such a spin-coating speed of 4000 rpm, the typical thickness of the sample is 3 μm. Due to a well-known polymerization-induced phase separation process [64], the laser exposed sample consists of a periodic distribution of liquid crystal-rich domains, corresponding to the dark regions of the interference pattern, and polymer-rich grating structure [65]. Two laser exposures were performed for the fabrication of phase mask. For the first exposure, two interfering laser beams came from the glass slide side as shown in Fig. 4.14 (a, b) and formed the liquid crystal-rich and polymer-rich gratings parallel to the y-direction. The liquid crystal-rich region is much less sensitive to further laser exposure than the polymer-rich region. More laser exposures will induce weak polymerization in the liquid crystal-rich region allowing this region to be washed out during the development. Thus the addition of liquid crystal in the photo-sensitive mixture helps preserve the grating structure produced in the first exposure. The time for first exposure was in the range of 0.5 to 2 s. Because the exposure time is short, only the photoresist near the glass-slide substrate becomes polymerized. Then the same sample was exposed to the laser interference pattern rotated by 90 degrees and coming from the sample side as shown in the figure. After an exposure in the range of 2 to 4 s, a grating parallel to the x-direction is formed. The sample was developed in propylene-glycol-methyl-ether-acetate (PGMEA) for 20 s and rinsed in isopropanol.
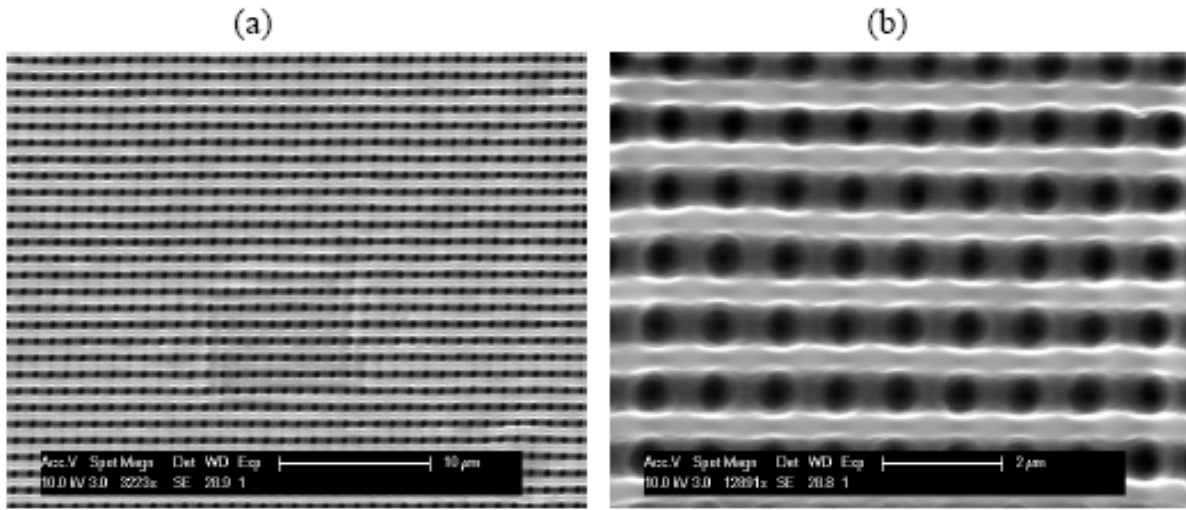
Figure 4.15 SEM of the fabricated phase mask showing two layers of grating structure (a), and the enlarged view (b).

Figure 4.15(a) shows the SEM of the fabricated sample. The SEM shows clearly two layers of grating structures, also shown in the Fig.4.15 (b) as enlarged view. The top layer has a grating in the horizontal direction. The layer beneath has a grating in vertical direction, orthogonal to the top grating structure. When a single beam goes through such a phase mask, it is desirable to have five and only five diffracted beams behind the phase mask, namely the (0,0), (0, ±1) and (±1, 0) beams, as indicted in Fig. 4.16 (a). The next lowest order beams are the (±1, ±1) beams. If the phase mask was designed properly, these four beams vanish. The five low order diffracted beams can be described by:

$$E_{0,0}(r,t) = E_{0,0}\cos(k_{0,0} \bullet r - \omega t + \delta_1)$$
$$E_{1,0}(r,t) = E_{1,0}\cos(k_{1,0} \bullet r - \omega t + \delta_1)$$
$$E_{-1,0}(r,t) = E_{-1,0}\cos(k_{-1,0} \bullet r - \omega t + \delta_1)$$
$$E_{0,1}(r,t) = E_{0,1}\cos(k_{0,1} \bullet r - \omega t + \delta_2)$$
$$E_{0,-1}(r,t) = E_{0,-1}\cos(k_{0,-1} \bullet r - \omega t + \delta_2)$$
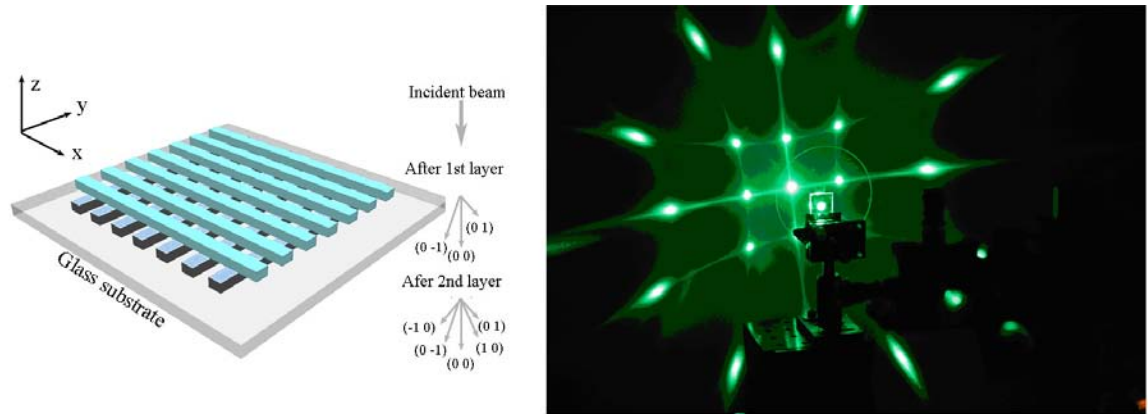
Figure 4.16 (a) Scheme of phase mask and diffracted beams by the top grating; (b) Photo of fabricated phase mask and diffracted beams by the phase mask.

where k and ω are the wave vector and angular frequency of the beam, respectively, E is the constant of electric field strength, and δ is the initial phase of the beam. If the initial phases for five-beam are the same, the generated interference pattern has FCC or FCT symmetry [66]. In this study, the initial phases for beams (0, 1) and (0, -1) are the same, but different from those for beams (0, 0), (1, 0), and (-1, 0), i.e. the δ_1 and δ_2 are different in the above equations. This is a consequence of the optical path difference developed between (0, 0) and (0, 1) (or (0, -1)) when (0, 0) beam goes in straight line while the (0, 1) or (0, -1) travels along a direction with a diffraction angle before further diffracted by second grating, as shown in Fig. 4.16(a).

As shown in Fig. 4.16(b) as an example, when one beam goes through the phase mask, nine diffracted beams can be produced. The beams (1, 0) and (-1, 0) have approximately the same intensity, although the (1, 0) beam spot looks bigger than (-1, 0) caused by a closer distance to the digital camera. Beams (0, 1) and (0, -1) have the same intensity also. The (± 1, ± 1) beams are very weak and their diffraction angles are larger than the (± 1, 0) and (0, ± 1) beams. The

beam intensities for (0, 1) and (0, -1) modes might be different from those for beams (1, 0), and (-1, 0), depending on the diffraction efficiency. As an example, one of the fabricated phase masks generates beam intensities with a ratio of 1: 0.68: 0.38: 0.13 for (0, 0), (1, 0), (0, 1) and (1, 1), respectively. The diffraction efficiency is determined by the cycle, depth, and period of the grating structure, the polarization direction of the laser, and the laser wavelength.

Experimentally the cycle and depth of the grating structure can be controlled through the weight percentage of photo-initiator, the laser exposure time and the sample development time [49]. The period of the grating can be controlled through the interfering angle of the two laser beams. There is a way to compensate the intensity difference during the exposure of the five-beam interference to the photo-sensitive material. If the polarization of the laser is set to be in [1, 0, 0] direction, the diffracted beams (1, 0) and (-1, 0) have polarization directions in xz plane with an angle relative to x-axis same as the diffraction angle. The diffracted beams (0, 0), (0, 1) and (0, -1) have the same polarization as [1, 0, 0]. If we define E(r, t) of each beam has the amplitude containing both the intensity and polarization. Thus intensity difference can be compensated by the selection of a polarization for the interference of above five-beam when calculating the dot product of two beams.

Using a 1D phase mask, two exposures of the sample to the interference pattern were required to produce a 3D photonic crystal. Using a 2D phase mask, one exposure can produce a 3D photonic crystal. With the two-layer phase mask produced in this work, not only can one produce a 3D photonic crystal by a single beam and single exposure, but also can introduce the phase shift of the interfering beams. Incorporation of the phase shift for (0, 1) and (0, -1) beams is necessary for the fabrication of 3D photonic crystals with a large PBG.

The lab-fabricated phase mask was used to generate a 3D photonic crystal template in the photoresist mixture with a similar formulation to that described above except that the liquid crystal was omitted. The DPHPA photoresist mixture was spin-coated on the glass slide substrate at a speed of 1000 rpm. The thickness is approximately 15 μm. The phase mask generated beam intensities with a ratio of 1: 0.68: 0.38: 0.13 for (0, 0), (1, 0), (0, 1) and (1, 1), respectively. The exposure laser has a wavelength of 532 nm with a polarization in the x direction [1, 0, 0]. As shown in Fig. 4.17(a), the photonic crystal template can be fabricated in the photoresist by the single beam and single exposure method using the phase mask. The photoresist was placed in a location where five and only five-beam overlap and generate the interference pattern. The exposure time was 60s. The exposed photoresist was developed in PGMEA. Figure 4.17(b) shows a large-scale SEM of the fabricated photonic crystal template. From the theory, the period of the structure in Fig. 4.17(b) should be the same as the grating period of the phase mask. The measured average period by SEM is approximately 1.02 μm, compared with the measured grating period of 1.06 μm in Fig. 4.17(b).
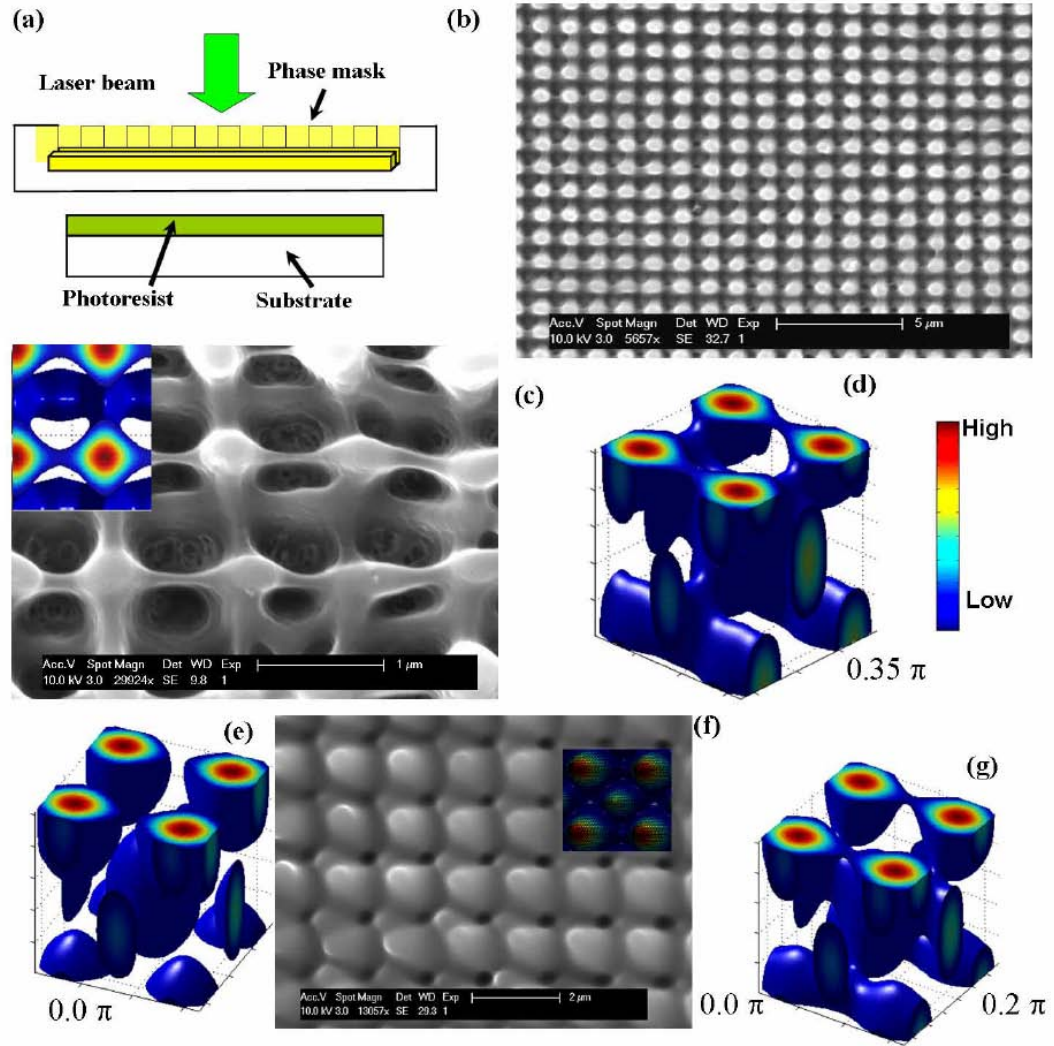
Figure 4.17 (a) Scheme of setup for single beam exposure; (b) SEM of photonic crystal template fabricated using the phase mask through single beam and single exposure method; (c) An enlarged view of SEM. The inset is the simulation of five-beam interference pattern; (d-e) 3D pattern of the five-beam interference with δ_1-δ_2=0.35 π (d) and δ_1-δ_2=0 π (e); (f) Fabricated structure in SU8 with δ_1-δ_2=0 π and simulated intensity pattern as an insert; (g) 3D pattern of the five-beam interference with δ_1-δ_2=0.2 π.

Figure 4.17(c) clearly shows a 3D feature of the fabricated structure. The detailed feature of the SEM can be simulated as shown as an insert in Fig. 4.17(c). The grating period of 1.06 μm was used for the simulation. The beam intensities were set with the values we have measured

66

above, namely, the ratio of beam intensity was set to be 1: 0.68:0.68:0.38:0.38 for (0, 0), (1, 0), (-1, 0), (0, 1), (0, -1) and (1, 1). The polarization of the incident laser was set in the [1, 0, 0] direction. After the diffraction, the polarization for (0, 0), (0, 1) and (0, -1) beams was set in the [1, 0, 0] direction. For (1, 0) and (-1, 0) beams, polarization directions were chosen in xz plane with an angle of 31 degrees relative to x-axis. The maximum phase shift (δ_1-δ_2) was estimated to be *0.47π* based on the sample thickness of 3 μm. A phase shift of *0.35π* (δ_1-δ_2=*0.35π*) between the group of (0, 1) and (0, -1) beams and the group of (0, 0), (1, 0), and (-1, 0) beams can simulate the fabricated structure in Fig. 4.17(c) (see the insert for the simulation). Figure 4.17(d) shows the 3D view of above simulated structure. As we have stated early, the incorporation of the phase shift for (0, 1) and (0, -1) beams is necessary for the fabrication of the diamond-like structure. If the phase shift is zero, the low-intensity iso-surface of the five-beam interference looks like spheroid-type FCC or FCT structure as shown in Fig. 4.17(e). Such a structure is not interconnected and thus is not stable. Under high laser dosage, the structure is interconnected but there is diminished accessibility for the solvent to wash out regions of low intensity exposure. Figure 4.17(f) shows a SEM of a fabricated FCT structure in SU8 photoresist under a high laser dosage with a phase shift of zero (the detail of the fabrication in SU8 will be reported elsewhere). The fabricated structure is in good agreement with a simulated intensity pattern of the interference as shown as an insert in Fig. 4.17(f). Compared Fig. 4.17(c) with Fig. 4.17(f), it is very clear that the fabricated structure through the two layer phase mask is totally different from the fabricated structure with zero phase shift. With a phase shift of 0.2 π, the spheroids start to interconnect and form diamond-like structure as shown in Fig. 4.17(g). The perfect phase shift is 0.5 π. With such a phase shift, the interference pattern has a diamond-like structure as reported in reference.

The fact that the fabricated structure through the two-layer phase mask can be simulated by an interference pattern with a phase shift and is totally different from the fabricated structure with zero phase shift, indicates that there is the phase shift among beams generated by the two-layer phase mask.

The described method solved the optical alignment problem that one has faced using two separate 1D phase masks. Alignment of the two interference patterns in 3D space proved difficult in the production of the wood-pile type photonic crystal. This work solves the previously encountered difficulties, because using two-beam interference for the fabrication of the phase mask, there is no issue of alignment as long as the sample is rotated by 90 degrees for the second exposure. Furthermore optical alignment is no longer a concern for the fabrication of the photonic crystal template using the phase mask through single beam and single exposure HL.

Once the optimal directions, amplitudes, polarizations, and phases are determined, a two-layer phase mask can be designed and fabricated to yield the optimal diffraction condition for the holographic fabrication. The integration of the two-layer phase mask on a single substrate represents a significant improvement toward mass production of 3D photonic structures. Since the two-layer mask can be readily integrated with multiple-layer amplitude mask based integrated circuit (IC) fabrication, the proposed approaches also provide an avenue for chip-scale integration of the 3D photonic devices with other light wave and electronic circuit elements.

4.4.2   PDMS grating mold imprinting approach

The above approach can easily fabrication two-layer integrated phase mask, but such mask is not perfectly applicable to 3D pattern fabrication, which we will discuss about in the next section.

The most crucial thing is it lacks phase tunability. We know that by two beam interference, the interference pattern profile looks like standing wave in sinusoidal form. The aspect ratio of the photoresist grating is determined not only by the expose dose but also by the develop time. However, the expose dose, experimentally, is determined by the output power of the laser and the shutter controlled exposure time, as well as the glass absorption if light incident from the back side. So, in the two layer grating fabrication process, it is not convenient to control the distance between two grating layer. To get the final grating structure interconnected, the two grating layers have to always attach to each other, to be sustained after photoresist development. The distance between two layers is fixed, equal to the thickness of the grating.

Another approach we demonstrate for holographic fabrication of photonic crystal structures with phase control of the diffractive beams. This technique reduces two laser exposures to one exposure and removes the need of the phase mask displacement. The phase mask used in this work is a two layer phase grating. Two phase gratings with desired orientations are separated by a spacer layer. Desired phase changes among different diffractive laser beams can be controlled by the thickness of the spacer layer. By doing so, the need of precise phase mask displacement is eliminated. Interconnected 3D photonic crystal structures such as woodpile structures can be directly fabricated in photoresist using one laser exposure for further processing. This critical improvement enables the fabrication of complex 3D photonic structures by a single laser exposure through a single optical element.
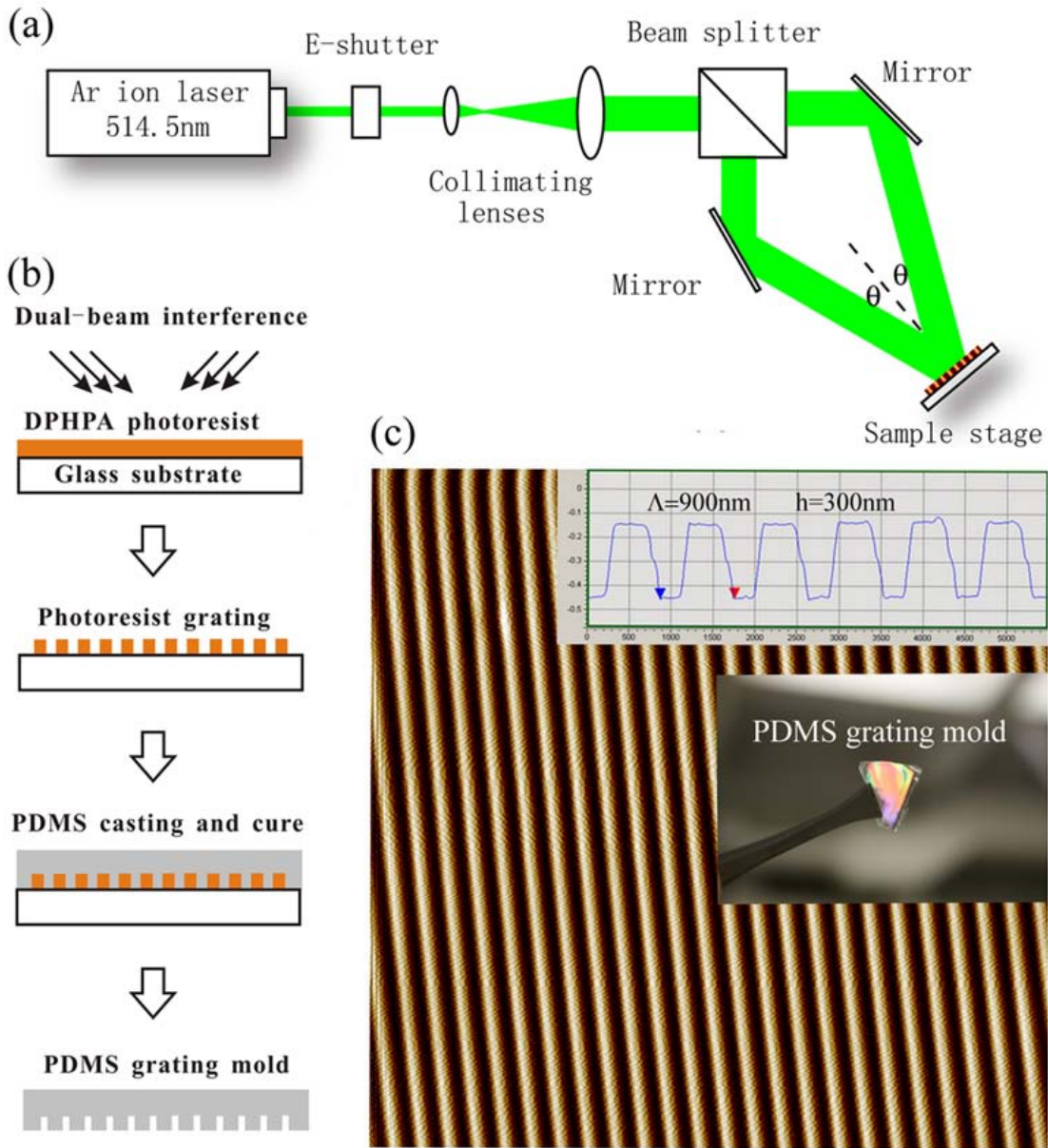
Figure 4.18 (a) Experiment setup phase grating holographic fabrication (b) PDMS grating mold inversion process. (c) AFM topography of the 10μm thick PDMS grating mold. Insets are the PDMS grating mode and the cross-section view of its sinusoidal profile.

The fabrication of two-layer phase gratings demonstrated here is a two-step procedure: the fabrication of mold in PDMS and the imprinting of two layer gratings in SU8. The mother

mold of the phase mask was fabricated in DPHPA photoresist using two-beam interference, according to the principle of Mach-Zehnder interferometer. A collimated, vertically polarized (out of the paper plane) laser beam was split by a 50:50 non-polarized beam splitter. The two resulting arm beams are reflected by mirrors and symmetrically projected on the photoresist sample surface, as shown in Fig.4.18 (a). Figure 4.18(a) shows the laser holographic fabrication process to produce the PDMS mold. The mother mold of the phase mask is fabricated in DPHPA photoresist (0.2 wt% Rose Benegal photo-initiator, 0.8 wt% NPG co-initiator, 10 wt% NVP solvent, 89 wt% DPHPA) using the approach of dual-beam laser interference HL. A short photoresist development time (1-5 s) was used to reduce the surface erosion. According to the diffraction formula $\Lambda = \lambda/(2n \sin \theta)$, the angle 2θ of the two interfering beams determines the grating period Λ in DPHPA. In this work $\theta = 30^{o}$ was chosen to produce a 900nm grating with about 5:1 0th/1st diffraction ratio. A subsequent pattern inversion transfers the grating into a daughter PDMS grating mold as shown in Fig. 4.18 (b). A pre-polymer solution of PDMS (Dow Corning® Sylgard 184; base: curing agent=10:1) was then poured onto the master. Then the sample is cured in an isothermal oven at 65°C for 1 hour and followed by a second cure at 100°C for 1 hour. The cured PDMS mold with a thickness about 10μm is peeled off from the master after cooling and bonded to a glass side. A surface treatment by oxygen plasma is applied to enhance the adhesion between the glass substrate and the PDMS grating. Fig.4.18(c) shows an atomic force microscope (AFM) image of the top and lateral views of the grating mold, which shows a uniform sine trapezoidal grating profile with 900nm period, 350nm ridge, and 250nm land and 300nm height. This mold is then used to imprint two-layer phase masks in SU8 photoresist.

Since the grating is designed to provide multiple coherent beams, the intensity and polarization of the diffractive beams are critical. Our purpose is to have five diffractive beams (0th and 1st orders) output and symmetrically allocate the most transmitted energy into those beams. Higher order diffractive beams can be minimized by optimal design the gratings lateral profile. Fig. 4.19 (a) shows the designed grating in a sine trapezoidal shape based on the actual AFM measured dimensions. Fig. 4.19(b) is the calculated diffractive efficiencies of the 1st order and 2nd order efficiency for a normal incident light with different polarizations. The solid lines are corresponding to the first layer grating and dot line for the second layer gratings. To have uniform 1st order diffractive beams, a quarter waveplate for 514.5nm is used to change our linear polarization laser beam in to circular. The diffractive efficiency ratio of 0th: 1st: 2nd order beams is 0.659:0.135:0.021 for single grating with a 22° diffractive angle. This indicates after two-layer gratings, if the absorption ignored, the ratio between (0, 0): (0, ±1) or (±1, 0): (±1, ±1) are 1: 0.205: 0.042. (Higher order beams are negligibly small).

The 5:1 0th to 1st diffraction ratio is important for a later fabrication process of 3D interference pattern, by 5 beam configuration. This ratio will determine the 3D structure's contrast ratio since background light may influent the crystal quality if 0th order has much larger intensity than 1st order beams; on the other way, if 0th and 1st order get comparable value, higher order (±1,±1) diffraction beams will be generated. 9 beam interference pattern will replace 5 beam one which spoil the symmetry of a FCT structure.
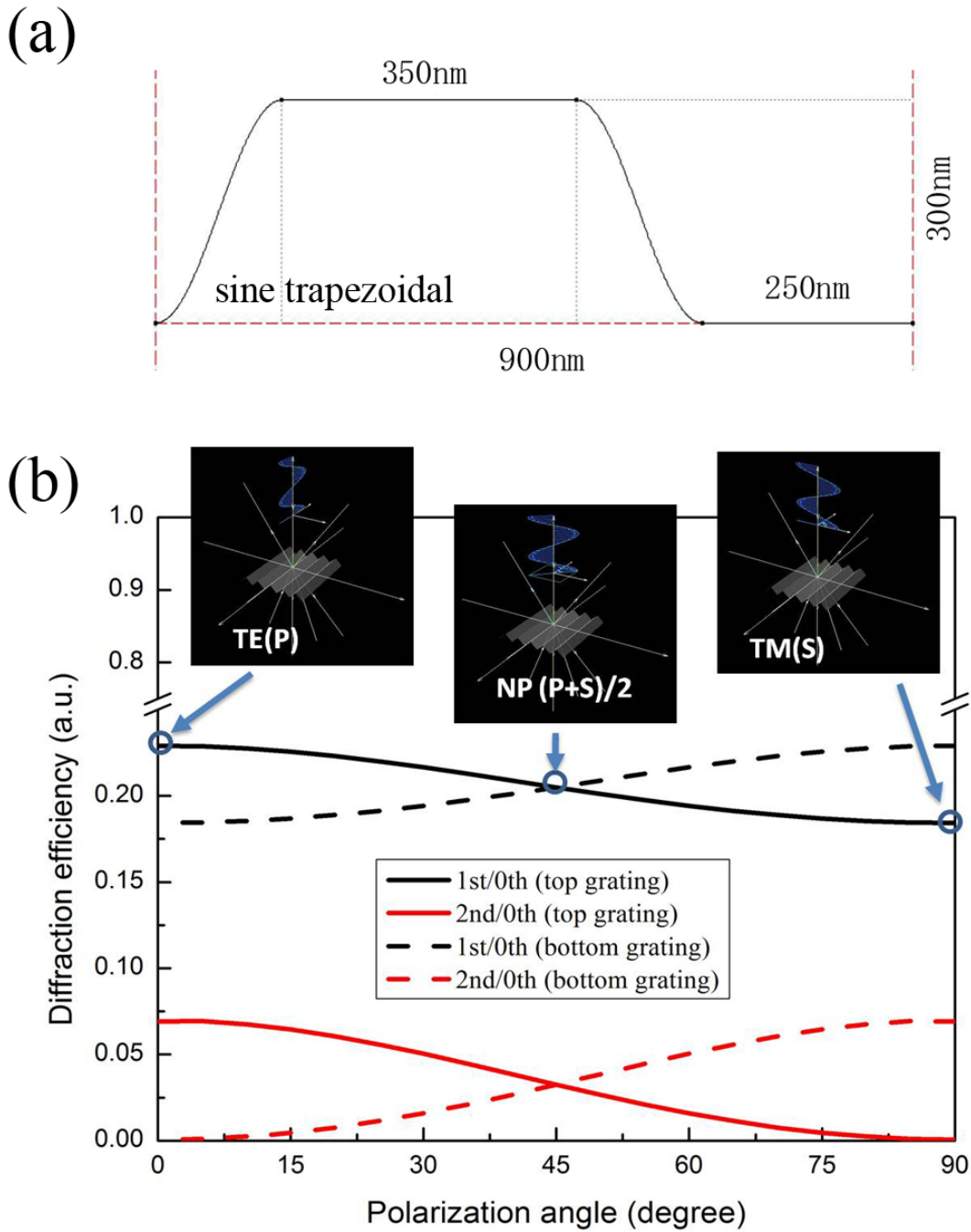
Figure 4.19 (a) Designed surface profile of the imprinting grating mold; (b) grating diffraction efficiency simulation for 1st order and 2nd order beams according to different polarized incident beam. To propagate through a two-layer orthogonal oriented grating, incident light with 45° linear or circular polarization can have equal diffractive outputs.

SU8 photoresist has been extensively used as building materials for MEMS and micro optic elements, thanks to its mechanic robustness, good thermal and chemical stabilities, and excellent optical transparency at visible wavelengths [67]. Figure 4.20 (a) depicts the two layer phase grating fabrication process in SU8. The PDMS grating mold was first used to imprint grating patterns on pure SU8-2035 photoresist (MicroChem Inc.) coated on a glass slide under a flood UV irradiation source (UL500P, Hoya-Schott Co.) for 1min. The exposed SU8 was partially polymerized by post-baking at 65°C for 10min. The PDMS mold is then peeled off from the SU8.
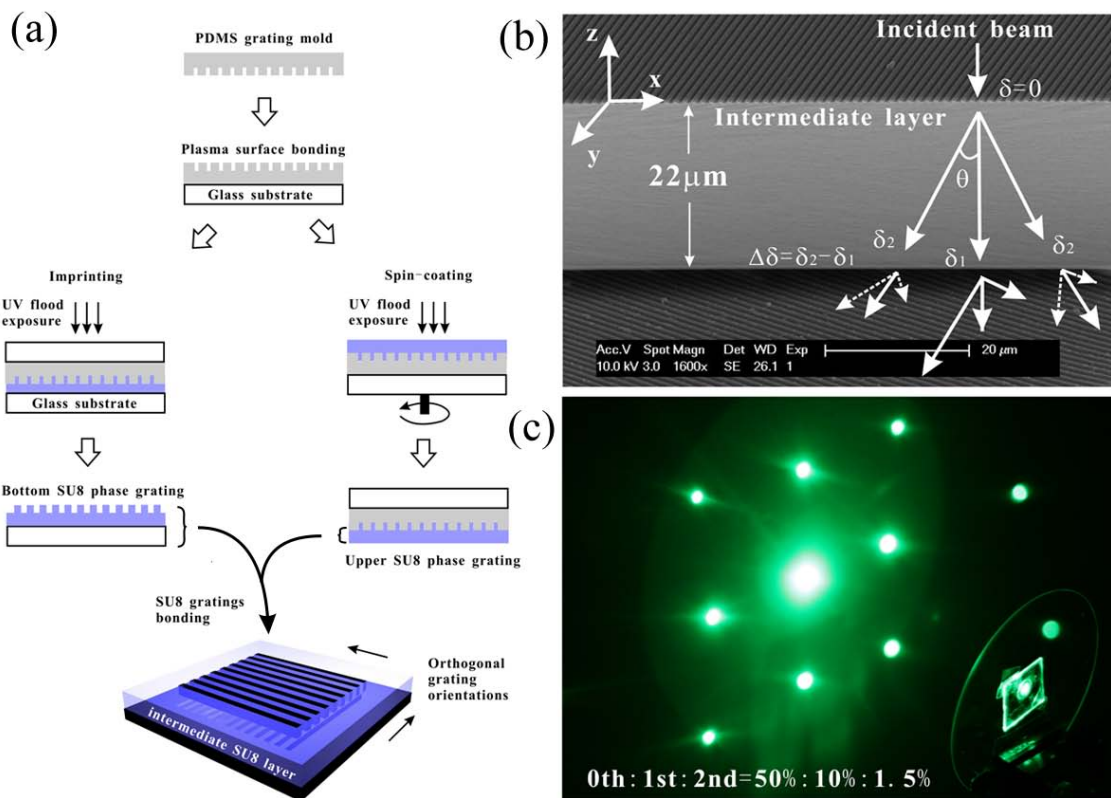
Figure 4.20 (a) Fabrication processes of the two-layer phase mask. (b) SEM image of bonded SU8 two-layer mask with orthogonal grating orientations. (c) Diffraction pattern of the two-layer phase mask.

To produce the second grating layer, a SU8 thin film was coated directly on the PDMS mold by a spin-coating process as shown in Fig. 4.20(a). The spin speed determines the film thickness which is important to the "built-in" phase delay of the mask. After the 2nd laser exposure on the SU8 film coated on the PDMS mold, both SU8 layers are brought into contact to form a two-layer structure. The two-layer mask was bonded at 95$^{\text{o}}$C for 20 min under 50 kPa pressure [68]. The mask was further hardened by a hard-baking process at 200$^{\text{o}}$C for another 20 minutes. The intermediate layer between two gratings is about 22 μm thick, which is produced by the spin-coating process at 2000 rpm. An SEM image of a bound two-layer phase mask is shown in Fig. 4.20 (b). A two-layer grating with orthogonal orientations is clearly visible with a spacer layer.

When a single beam goes through the first layer of grating, it produces diffractive beams in x-z plane as shown in Fig. 4.20 (b) labeled as (0, 0), (1, 0), and (-1, 0) orders. The (0, 0) beam incurs a different phase from (±1, 0) beams through the intermediate layer due to the propagation path difference. The second layer of grating further diffracts beams in the y-z plane to form 9 diffractive beams labeled as (0, 0), (0, ±1), (±1, 0), and (±1, ±1) beams, respectively. Fig. 4.20 (c) shows a diffraction pattern of the grating. Uniform diffractive beams are found and the intensity ratios were measured as 50%: 10%: 1.5% for (0, 0) order: (±1, 0) and (0, ±1) orders: (±1, ±1) orders, respectively, which is consistent with the simulation result perfectly.

The highest order beams (±1, ±1) have much weaker intensity as measured and therefore have negligible effects on interference patterns. Therefore, the two-layer phase masks will produce five-beam interference patterns by (0, 0), (±1, 0), and (0, ±1) beams. When a plane wave propagating through the top layer of the phase mask, phases for beams (0, 0) and (0, ±1) are $\delta_1 = \frac{2\pi}{\lambda}nd$ and $\delta_2 = \frac{\delta_1}{\cos\theta}$, respectively, where n and d are the index of refraction and the thickness

75

of the spacer layer, respectively. The (0, 0) order beam was further split (0, 0) and (0, ±1) beams upon the incident on the second layer of the phase mask. Since periods for both layers of grating are identical, the phase difference between (0, ±1) beams and (0, 0), (±1, 0) beams remain $\Delta\delta = \delta_2 - \delta_1$ after the second layer of the phase mask.

This two-layer phase mask is then used to produce 3D photonic crystal templates in DPHPA photoresist through one laser exposure. The phase difference between (0, ±1) beams and (0, 0), (±1, 0) beams is critical for the formation of interconnect 3D photonic crystal structures. If the "built-in" phase delay $\Delta\delta$ for five beams are zero or integral multiples of π, the generated interference pattern has FCT symmetry, as shown in the 3D simulation in the insets of Fig.4.21 (a). When $\Delta\delta$ are odd integral multiples of $\pi/2$,10 the 3D template will evolve into interconnected woodpile structures as shown in the 3D simulation in the inlet of Fig. 4.21(b).
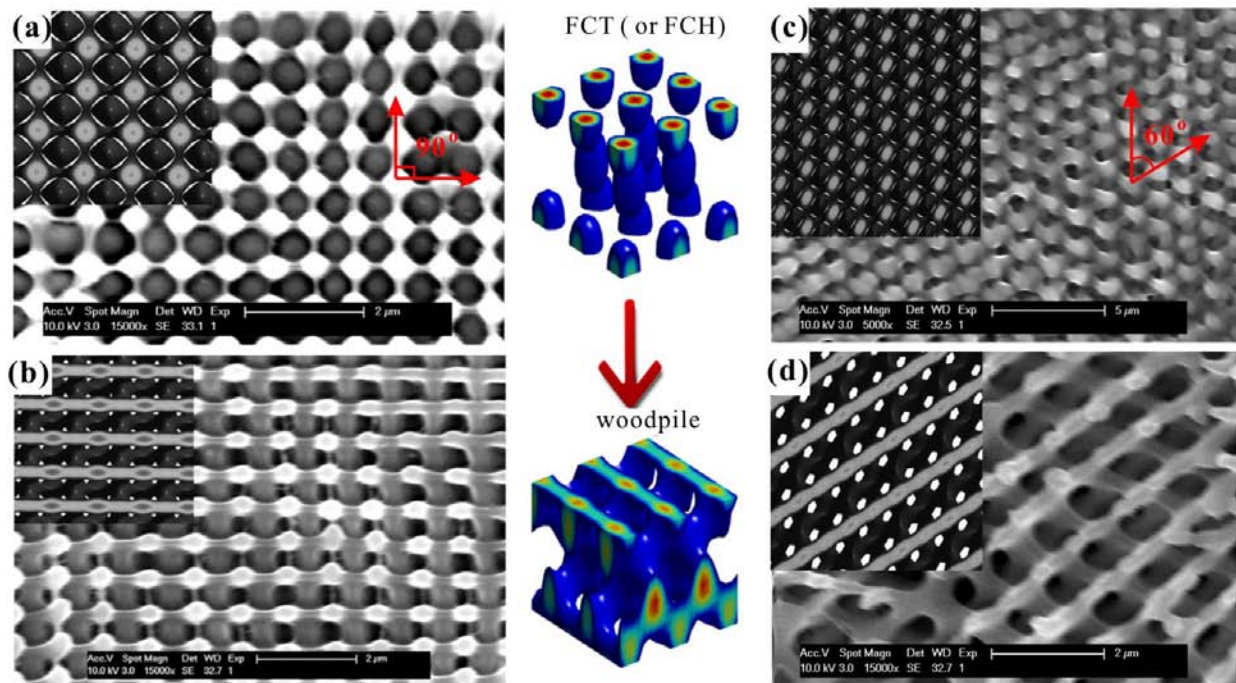
Figure 4.21 SEM pictures of fabricated structures in the photoresist through an orthogonal two-layer phase mask with symmetries of (a) FCT and (b) woodpile structure. Insets are the simulation structure for comparison with parameter setting (a) $\Delta\delta=0$ and (b) $\Delta\delta=\pi/2$; And structure fabricated through a 60-degree

two-layer phase mask with symmetries of (c) Face Centered Hexagonal and (d) 3D hexagonal piled structure. Insets are the simulated structures with (c) $\Delta\delta=0.1\pi$ and (d) $\Delta\delta=\pi/2$.

The phase shift of $\pi/2$ is corresponding to a thickness change of $(\lambda/4n) / ((1/\cos\theta - 1))$, i.e. 498 nm, given the period of the phase mask. To yield optimal 3D structures, a thermal tuning was used to adjust the phase delay induced by the as-fabricated two-layer phase mask. The thermal expansion coefficients of the hard-baked SU8 samples (n=1.67 at 514.5nm) were reported as 102 ppm/$^{\circ}$C for in-plane and 253 ppm/ $^{\circ}$C for out-of plane (thickness direction) [68]. Thus, for a 22 μm thick intermediate layer, the phase delay can be tuned by raising temperature at a rate of 0.011rad/ $^{\circ}$C.

The phase mask was mounted by a metal frame holder on a hot plate. The ambient temperature of the phase mask was raised by every 30 degree from room temperature to 240 $^{\circ}$C, which is close to $\pi/8$ phase change for every 30°C temperature increment. Once the temperature of the phase mask is stabilized, the DPHPA photoresist samples were placed in a close proximity of the phase mask for laser exposure. The laser exposure time was between 1-2 s and the samples were taken off rapidly after exposure.

Fig. 4.21 (a) and (b) shows SEM pictures of the 3D photonic crystal by using the thermal controlled two-layer phase mask. Fig 4.21(a) reveals FCT structures when the phase delay $\Delta\delta= \delta_2-\delta_1$ was not well-controlled. Since FCT structures are not interconnected, only one layer of period structures were left on the glass slide after the photoresist development. The fabricated structures match the simulated structure with zero phase delay $\Delta\delta= \delta_2-\delta_1=0$. When the phase delay are close to odd integral multiples of $\pi/2$, thicker and interconnect 3D structures started to develop. Fig. 4.21(b) shows a woodpile-like 3D multi-layer structure. The surface morphology closely match the simulation results shown in the inlet with a phase delay $\Delta\delta= \delta_2-\delta_1= \pi/2$.

The flexible fabrication approach of the two-layer phase mask can be extended to two-layer grating with other orientations. Fig.4.21 (c) and (d) shows the SEM pictures for 3D structures produced by a two-layer phase mask with 60° angle orientation respect to each other. The phase mask was prepared in the same way as described in Fig. 1 and 2 with a 22 µm thick spacer layer. 3D photonic crystal structures demonstrated in Fig.4.21 (c) and (d) match simulation structure with the phase delay $\Delta\delta = \delta_2 - \delta_1$ of 0.1π and $\pi/2$, respectively.

Theoretically, the interconnected 60° woodpile-like 3D structure shown in Fig.4.22 (b) could produce a larger bandgap than that in the orthogonal woodpile-like structures if followed-up pattern inversion process was taken [6]. Moreover, the mask fabrication approach further enable hybrid combinations of micro-molding and lithographic processing, such as multi-layer phase mask for quasicrystal fabrication , to fabricate complex micro-optics that are difficult to realize using conventional techniques.

In summary, we have developed of an integrated two-layer phase mask to produce five diffractive laser beams with a thermal controlled phase delay. Interconnected 3D woodpile photonic crystal template can be produced through this single optical element by only one laser exposure. This simple manufacturing process has potential to be integrated into existing photolithography-based fabrication approach used for 3D optoelectronic circuit manufacturing.

5.0   PHASE TUNING APPORACHES IN HOLOGRAPHY LITHOGRAPHY

This chapter demonstrates a phase tunable holographic fabrication of 3D photonic lattice structures using a single optical element. A top-cut four-side prism is employed to generate five-beam 3D interference patterns. A silica glass slide is inserted into the optical path to adjust the phase of one interfering beam relative to other four beams [8]. The phase control of the interfering laser beam renders the lattice of the interference pattern from a face-center tetragonal symmetry into a high contrast, interconnecting diamond-like symmetry [69]. This method provides a flexible approach to fabricating 3D photonic lattices with improved photonic band structures.

5.1   PHASE TUNING WITH A TOP-CUT PRISM SETUP

In this chapter we will demonstrate a phase tunable holographic fabrication of 3D photonic lattice structures using a single optical element. A top-cut four-side prism is employed to generate five-beam 3D interference patterns. A silica glass slide is inserted into the optical path to adjust the phase of one interfering beam relative to other four beams. The phase control of the interfering laser beam renders the lattice of the interference pattern from FCT symmetry into a high contrast, interconnecting diamond-like symmetry. This method provides a flexible approach to fabricating 3D photonic lattices with improved photonic band structures.

79

Technically, it is relatively easy to produce multiple coherent laser beams with precise interference angles by a single optical element. However, HL techniques using a single optical element presented so far, lack precise phase control of the interfering beams. Precise phase control of interfering laser beams is critical to the fabrication of complex, highly symmetric photonic structures such as the diamond-like structures which possess large PBGs. The technique demonstrated following provides a simple approach to finely tune and optimize photonic band structures with large PBG width.
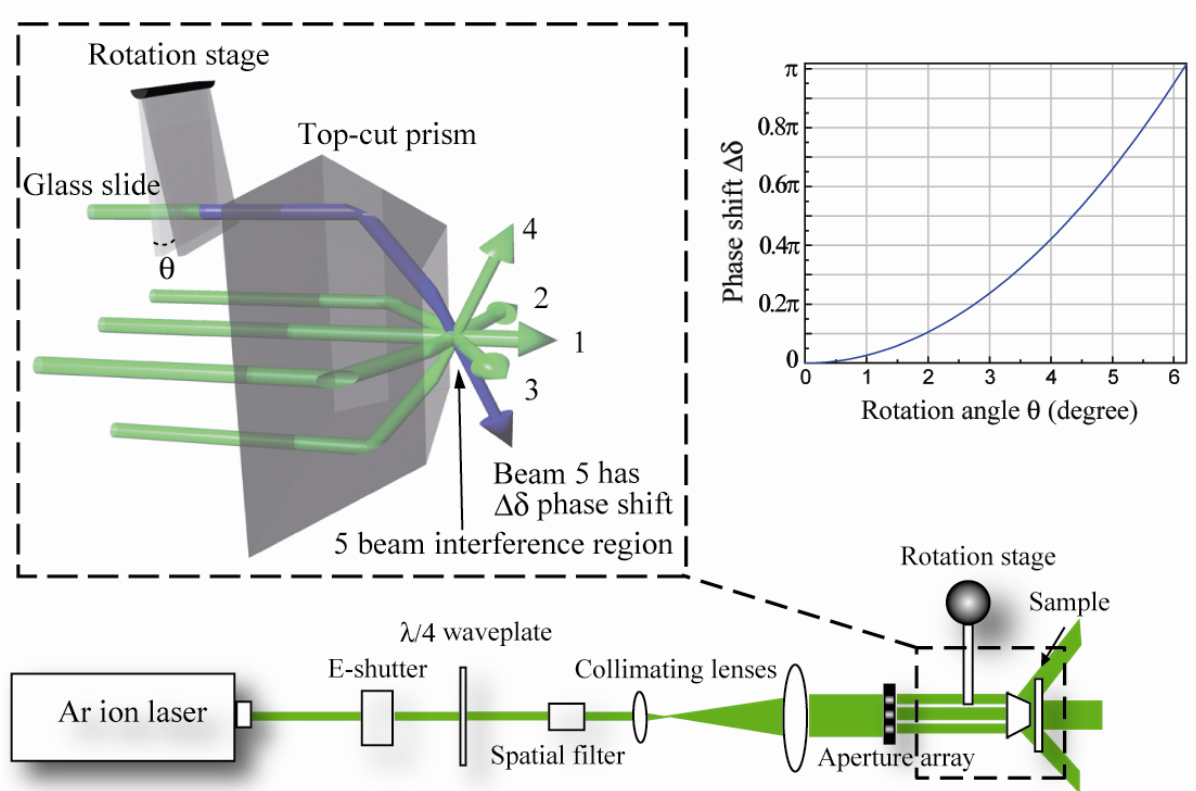
Figure 5.1 Experiment setup of the five-beam interference with one beam modulated by a glass slide. Inset: phase modulation $\Delta\delta$ as a function of the glass slide rotational angle θ.

The single optical element used to construct the five-beam interference pattern is a top-cut, four-side prism. Five-beam are selected by a set of apertures from one incoming collimate beam. The use of the apertures prevents laser beams from hitting corners and edges of the prism. As shown in the inlet of Fig.5.1, all five laser beams are incident from the bottom side of the prism. After total internally reflected at four lateral surfaces of the prism, Beam 2-5 refract through the top surface of the prism and recombine with Beam 1 to form interference patterns. To perform the phase modulation, a thin microscope glass cover slide with a uniform thickness (Corning, BK7 glass, d=130μm, n=1.52) is inserted into one of five-beam used to form interference patterns (labeled as Beam 5 in Fig.5.1). By rotating the glass slide, the phase of the Beam 5 can be adjusted continuously.
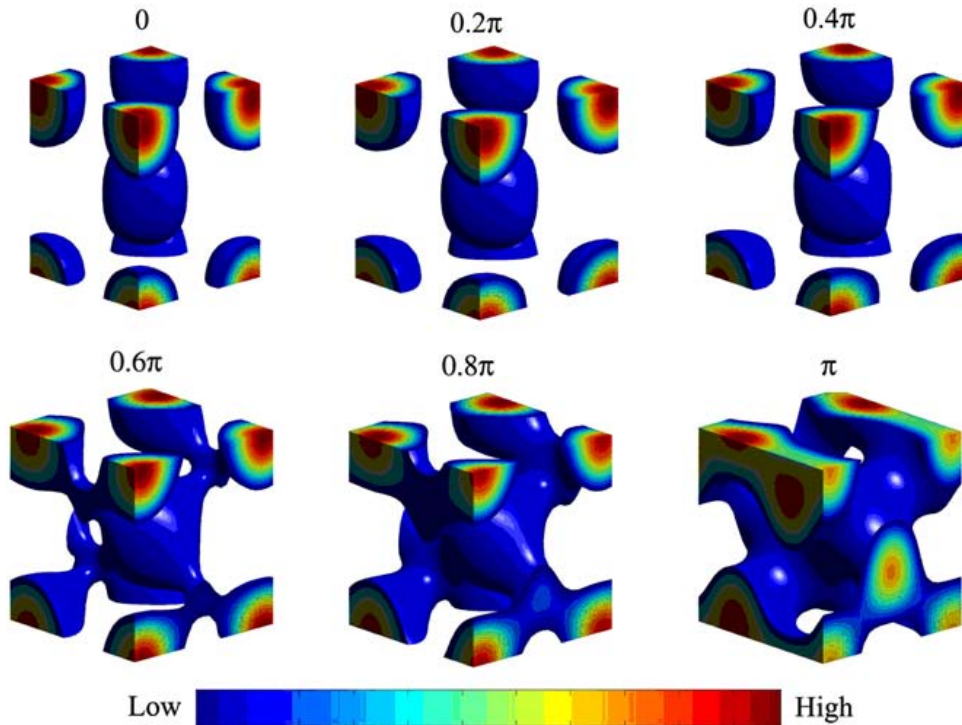
Figure 5.2 Isosurface of the unit cells of the phase modulated five-beam interference pattern, I_{mod}. The phase change $\Delta\delta$ varies from 0 to π with 0.2π increment.

The rationale of the phase control of one interfering beam can be briefly described as the following. The intensity profile of the five-beam interference pattern can be calculated as,

$$I = \left\langle \sum_{i=1}^{5} E_i^2 \right\rangle + \sum_{i<j}^{5} E_i \cdot E_j \cos\left[(k_i - k_j)r + \Delta\delta_{ij}\right], \tag{5.1}$$

where E_i is electric field strength and k_i is wave number. The insertion of the phase control glass slide in the Beam 5 induces an additional phase modulation $\Delta\delta$, which only affects on the last term of Eq. (5.1) and we can rewrite Eq.(5.1) as,

$$I_{\text{mod}} = I_{non-\text{mod}} + \sum_{i=1}^{5} E_i \cdot E_5 \cos\left[(k_i - k_5)r + \Delta\delta\right] \tag{5.2}$$

where I_{mod} and $I_{non-\text{mod}}$ denote the isosurface of the intensity pattern related to and not related to the phase modulation, respectively. The additional phase modulation $\Delta\delta$ as a function of the glass slide rotation angle θ can be described as,

$$\Delta\delta(\theta) = \frac{2\pi}{\lambda}\left\{ \frac{d}{\cos\alpha}[n_{glass} - n_{air}\cos(\theta - \alpha)] - (n_{glass} - n_{air})d \right\} \tag{5.3}$$

where $\alpha = \arcsin(\sin\theta/n_{glass})$ and λ is the incident wavelength. Fig.5.1 inset illustrates the relation between the phase change $\Delta\delta$ and the rotation angle θ from Eq. (5.3). From this curve, we can see that 6.1 degree of rotation of the glass slide is enough to produce a π phase retardation using the current setup. Fig.5.2 shows the variation of unit cell lattices for the five-beam interference pattern as the phase change $\Delta\delta$ evolves from 0 to π with a 0.2π increment. The evolution of the phase change $\Delta\delta$ renders the interference pattern (or holographic photonic crystal) from FCC or FCT structure into interconnected structures. When the phase modulation reaching the optimal value $\Delta\delta = \pi$, a diamond-like network is formed.

To experimentally validate the phase tuning and structure controlling, 3D photonic crystal templates were fabricated in a negative-toned DPHPA photoresist mixture. The mixture

was spin-coated on glass slides at 2000 rpm for 2 min. No prebake procedure was used before receiving exposure.

A 514.5nm circularly polarized laser beam from Ar ion laser (Coherent Inc.) was cleaned, expanded, and collimated by spatial filter and collimating lens. The BK7 microscope slide used for phase tuning was mounted on a rotational stage. The exposure dose in use is tested in the range of 100-1000 mJ/cm^2. After exposure, the photoresist samples were developed directly in propylene glycol methyl ether acetate for 20s, followed by rinsing in isopropanol for 10s and then left to dry in air.
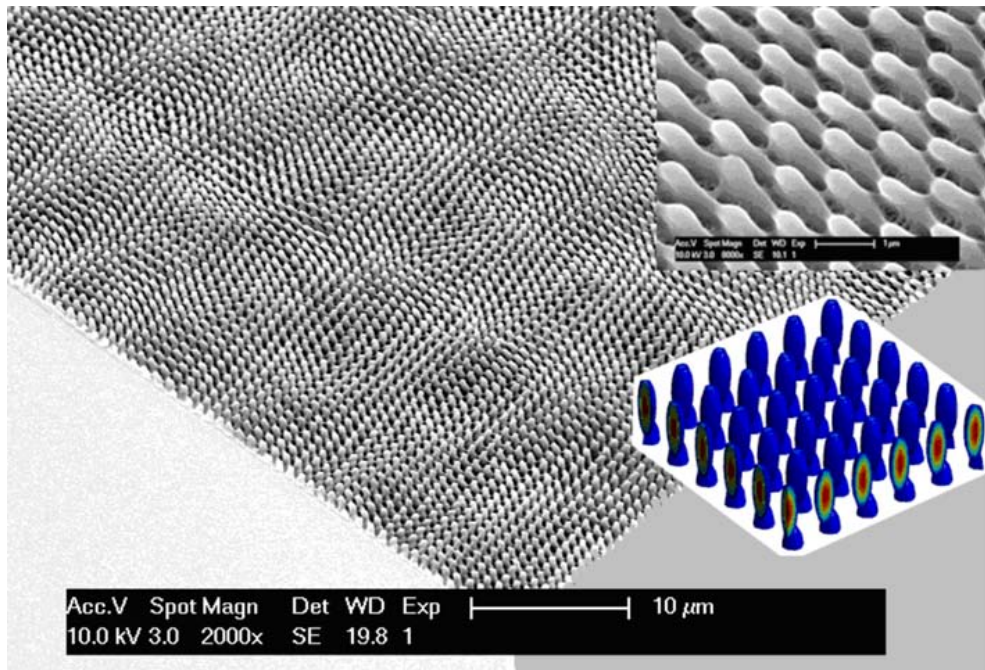
Figure 5.3 SEM pictures of fabricated structures in the photoresist through the five-beam interference without a phase modulation; inset are the zoom in view of the bottom layer and a simulation for a comparison.

Fig.5.3 shows the SEM pictures for the recorded five-beam interference pattern in the photoresist. In this case, the glass slide for phase modulation was not used. Without the phase modulation, the developed photoresist did not form interconnected networks. Only one layer of developed photoresist was left on the glass slide. 2D structures shown in the SEM is in good agreement with the simulated one (see insert in Fig.5.3).
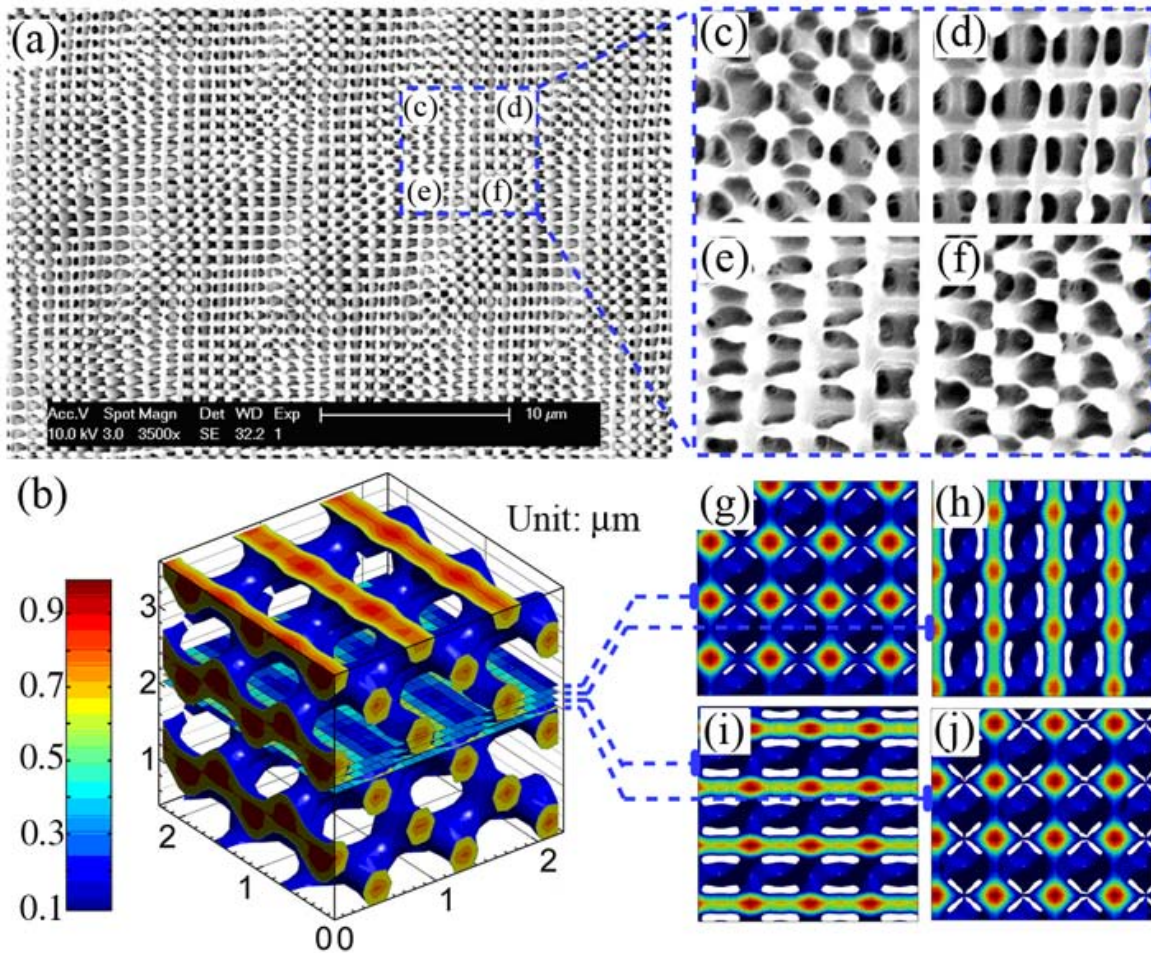
Figure 5.4 (a) SEM pictures for the photoresist templates of the interconnecting diamond-like structure, produced by the five-beam interference with phase retardation; (b) Computed five-beam interference pattern and its selected cross-section planes along height (z) direction; (c-f) Structure variation described by the zoom-in SEM views of the diamond-like template and their corresponding simulation planes from (b).

In a sharp contrast, the introduction of a phase tuning mechanism in the five-beam HL using the prism yields overlapping diamond-like structures. Figure 5.4(a) shows the SEM image for the photonic crystal template formed in photoresist with diamond-like structures, which were achieved by the phase tuning of the Beam 5. As predicted by the simulation in Fig. 5.4(b), the fine phase tuning transforms the photonic crystal template from the FCT symmetry to diamond-like symmetry. The interference pattern locked in photoresist clearly shows interlaced structures with diamond-like symmetries in Fig. 5.4. The period of diamond-like structure in the Fig. 5.4(a) in x (or y) direction is measured to be 0.85 µm, in good agreement with a theoretic prediction of 0. 84 µm with an interference angle of 37.5 degrees and a period of 0.82 µm in Fig. 5.3 for the fabricated one-layer structure.

A detail examination of the SEM photo shows that various interlaced structures were produced periodically on the surface of the photoresist with a period of around 8.6 µm, which is approximately 10 times as large as the diamond-like lattice period. Zoom-in SEM pictures, as shown in Fig. 5.4(c)-(f), present detailed features of various interlaced structures in the developed photoresist. These structural variations could be attributed to a slight mis-alignment of the sample. The surface of the photoresist film is not completely perpendicular to the normal incident laser beam, but cut through the (0, 0, 1) surface of the diamond-like structure at a small angle. This will result in surface topology representing diamond-like structures at different depth. The comparison between the simulation and the experiment showed in Fig. 5.4 confirms this speculation. Fig.5.4(g)-(j) shows the computed five-beam interference pattern where one beam has a phase retardation of π relative to other four beams, and its selected cross-section planes along height (z) direction. The fabricated topographic images shown in Fig.5.4(c)-(f) match well with those simulation planes.

It should be pointed out that the PBG properties of the photonic crystal can be improved by such phase modulation. Theoretical simulation predicts that the photonic structure templates duplicated from the five-beam interference patterns can have complete bandgap if the templates or their inverse replica structures are translated into high-index materials. Such inversion processes have been well-documented. If the template structure shown in Fig. 5.4 is translated into a 3D photonic structure consisting of air filled voids and high refractive index dielectric materials such as Si, the phase modulation $\Delta\delta$ from 0 to π will lead to an improvement of PBG width (bandgap width/bandgap central frequency) from 3.8% to 25%, with a change of bandgap location from band 8-9 to band 2-3.

Up to now, we have demonstrated phase tunable holography fabrication of 3D diamond-like photonic crystal templates using a top-cut prism as a refractive optical element and a glass slide as a phase modulator. The phase modulation can transfer the template from FCT structure to diamond-like structure, as confirmed though SEM images. This approach provides a simple and versatile way to control holographic interference patterns to fabricate photonic crystal with optimized optical properties.

5.2 **PHASE TUNING WITH A SPECIALLY DESIGNED PHASE MASK SETUP**

The prism setup can have good 3D pattern by single exposure. However, the bulk volume of this beam-splitting optical element makes it less compatible to other optical components, which typical have size at micron or smaller scales. So, we are switching to design an optical element to replace the beam-splitting prism and at same time with at least one critical dimension in micro size.

86

5.2.1 Design a coplanar phase mask

The single DOE is produced by recording gratings in a photosensitive photoresist mixture. In order to obtain right grating depth and grating cycle for high diffraction efficiency, low power laser is used so that laser exposure time is extended and used as a control of exposure condition. Thus Coherent Compass laser (532 nm, 60 mW) is used for the exposure of the photoresist mixture. One laser beam was expanded to a size of 4 mm and separated into two by using a 50:50 beam splitter. Parallel fringes are formed when two laser beams overlap. The laser polarization is set in parallel with fringes. The DPHPA photoresist mixture is spin-coated on a glass slide (25 mm x 25 mm) with a speed of 3000 rpm for 2 min. The glass slide is mounted on a rotation stage combined with a linear motion stage (Thorlabs Inc.). The location of the glass slide is initially adjusted with two beams overlapped in the rotational center, then moved away from the center by 5.1 mm. After the photoresist mixture receives the first exposure, the glass slide is rotated by 90 degree for the second exposure. Totally four-gratings are produced for the entire grating writing process as shown in Fig. 5.5(a). The exposure time is 2 s for each exposure. After exposure, the photoresist mixture is developed directly in PGMEA for 20s, followed by rinsing in isopropanol for 10s and air drying. Figure 5.5(b) shows the SEM pictures of fabricated gratings in the thin polymer on the glass slide. The period of the grating is approximately 0.78 μm. Thus the fabricated DOE consists of the central opening surrounded by four diffraction gratings orientated four-fold symmetrically with size of 4 mm in diameter and period of 0.78 μm.

$$\Lambda \cdot \sin \alpha = m\lambda$$
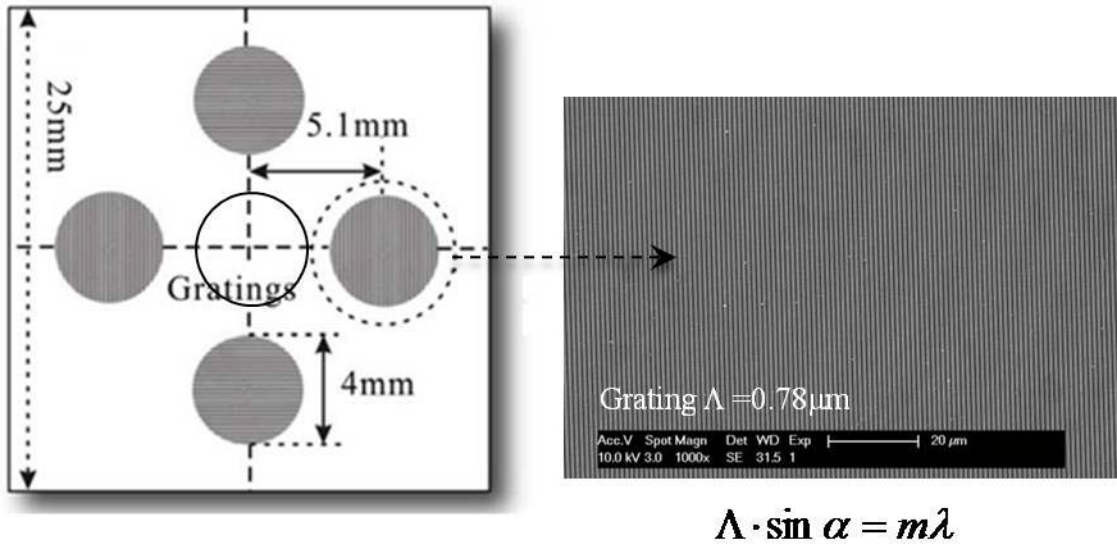
Figure 5.5 (a) Scheme of single DOE consisting of one central hole and four side gratings. (b) SEM of fabricated grating in a polymer.

5.2.2 Fabrication of 3D structure using the DOE

Fig.5.6 shows the optical setup for the holographic fabrication of 3D photonic crystal template. For the five-beam HL, a high power laser is needed. Thus a 514.5nm laser beam from a Sabre Ar ion laser (Coherent Inc.) is circularly polarized, cleaned, expanded, and collimated by spatial filter and collimating lens. Five-beam are selected by an aperture array from one incoming beam. When the beams go through the single diffraction element, four first-order diffracted beams overlap with the central beam passing through the central opening (labeled as beam 1 in Fig. 5.6). The four beams are arranged symmetrically around the central one and tilted at the same angle. The first-order diffraction efficiency of the gratings is approximately between 24% and 28% of the incident beams 2, 3 and 4. The diffraction efficiency of the grating for beam 5 is 30%. The phase of the beam 5 is delayed by inserting a thin microscope glass cover slide with a uniform thickness (BK7 glass, d=130μm, n=1.52).

88

By rotating the glass slide through a rotation stage, the phase delay of beam 5 can be adjusted continuously and precisely.
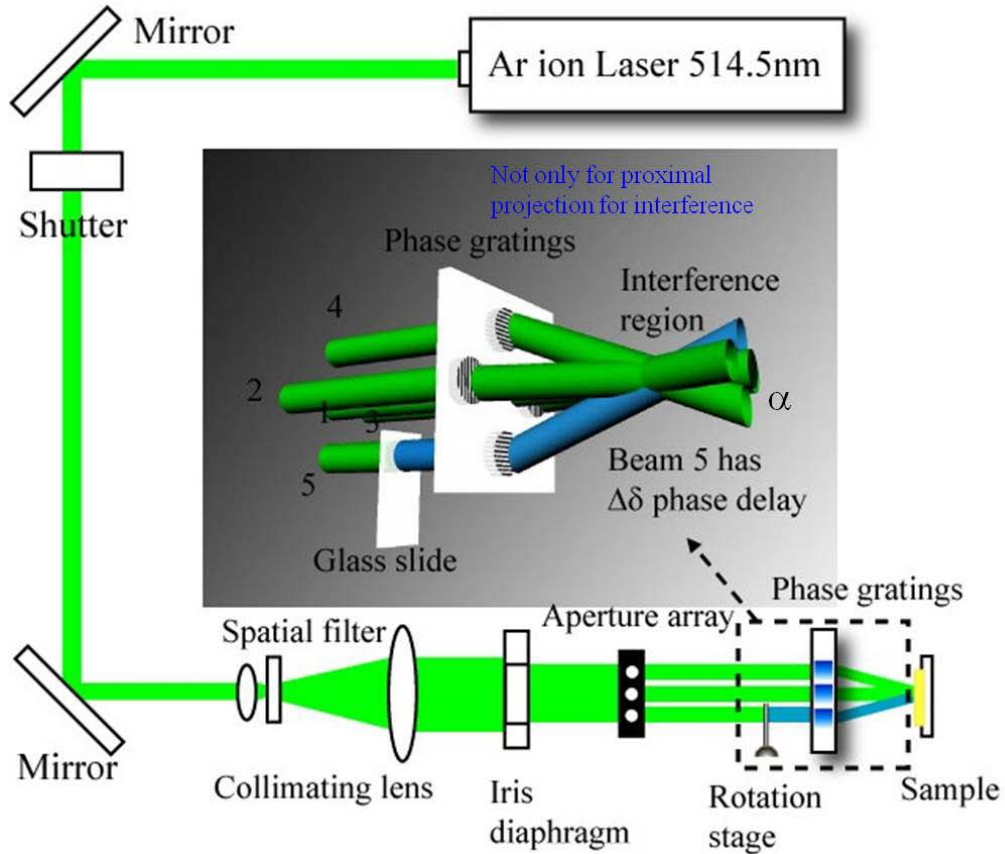
Figure 5.6 Experimental setup of the five-beam holographic fabrication using the single diffractive element with one beam phase-delayed by a glass slide.

The insertion of the glass cover slide introduces a large phase delay for beam 5. However the interference pattern with a phase delay of $\Delta\delta_{5i}$ is the same as the one with a phase delay of $\Delta\delta_{5i} + 2n\pi$ (n is an integral) because of the periodicity of the cosine function. A phase delay of $\pi+\Delta\delta_{5i}$ produces the same pattern with a phase delay of $\pi-\Delta\delta_{5i}$. Thus we can simulate the five-beam interference pattern related to the phase delay by changing $\Delta\delta_{5i}$ from 0 to π.
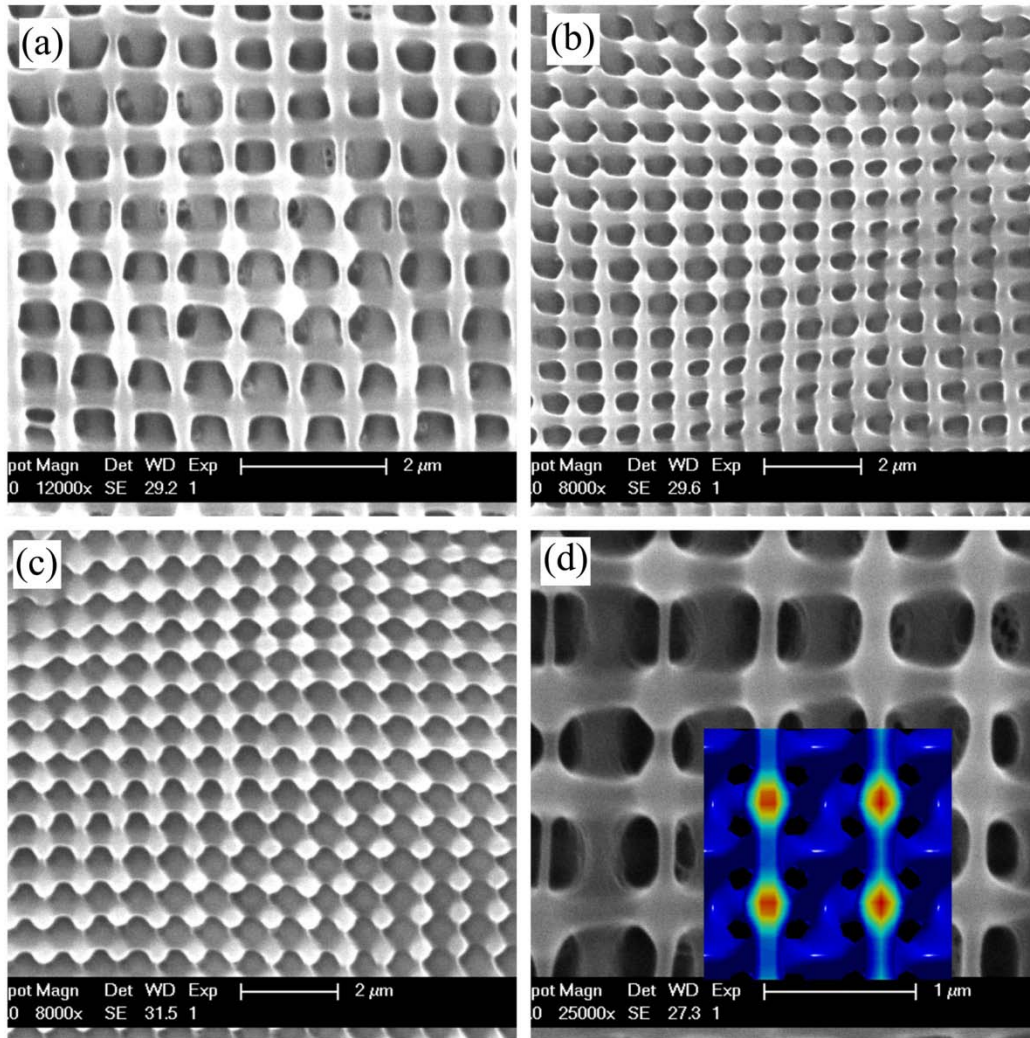
Figure 5.7 SEM of recorded five-beam interference pattern in photoresist polymer. (a-c) The photonic structure fabricated with the glass slide rotation angle of 2, 4, and 6 degrees, respectively. (d) Enlarged view of the SEM (a) and the inserted simulation of structure with a phase delay of π.

The same photoresist mixture as the one used for the grating is used to record the 3D interference pattern. The photoresist mixture is spun onto the glass substrate at 2000 rpm for 2 min. A laser power of 750 mW is used. After going through the diffraction grating, the first-order diffraction beam has power between 4 and 5 mW. The central non-diffracted beam has a power of 17 mW. The photoresist is exposed to the interference pattern for 10 s. After exposure, the photoresist mixture is

developed in PGMEA for 5 min, rinsed by in isopropanol for 1 min and left in air to dry. After development, a colorful sample with a size of around 4 mm is obtained.

Figure 5.7 shows SEM images of fabricated 3D photonic structures in polymer using the single diffraction element. Figures 5.7 (a-c) are the structures fabricated with the inserted glass slide rotated by 2, 4 and 6 degrees, respectively. A woodpile-like (or diamond-like) structure is clearly seen in Fig. 5.7(a), indicating a phase delay $\Delta\delta_{5i}$ close to π. From Fig. 5.7(c), we can see that the spheroid is sitting in the lattice of FCT structure, similar to the simulated structures in Fig. 5.2 with a small phase shift. Fig. 5.7 (b) has a structure with a phase delay between above two phase delays. From these figures, it is clear that the optical setup using the phase tunable single diffraction optical element can be used to fabricate 3D structures with well-controlled features. From the calculations $\Delta\delta_{5i}$(4 degrees)- $\Delta\delta_{5i}$(2 degrees)=0.32π, $\Delta\delta_{5i}$(6 degrees)- $\Delta\delta_{5i}$(2 degrees)=0.85π and by comparing the Fig. 5.7 with Fig. 5.2, Figs. 5.7 (a-c) can be corresponded with simulated structures with a phase delay of π, 0.68π, and 0.15π, respectively. Figure 5.7(d) shows the enlarged view of the structure in Fig. 5.7(a) and the inserted simulation with a phase shift of π. The agreement between the SEM and the simulated structure is very good. The period of diamond-like structure in Fig. 5.7(a, d) is measured to be 0.78 μm, in agreement with the period of grating shown in Fig. 5.5.

5.2.3 Simultaneous fabrication of line defects and 3D structure
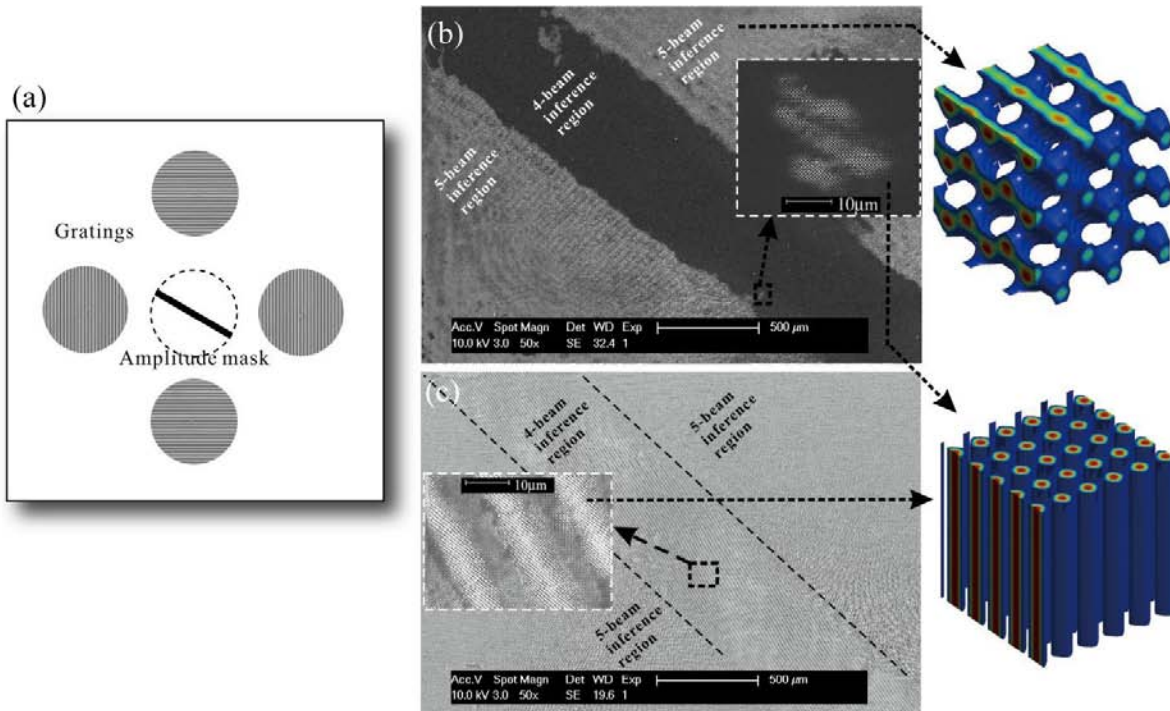
Figure 5.8 (a) Scheme of single diffractive optical element setup consisting of four gratings and an amplitude mask. (b) and (c) shows SEM pictures of the fabricated 3D photonic crystal structures with a line defect, introduced by the amplitude mask. The exposure dose can be chosen to be either between the threshold sustaining-values of 4-beam patterns and 5-beams patterns (b) or above both values (c).

In addition to the phase tunability in the demonstrated method, the single diffractive optical approach can be further extended to produce 3D photonic crystals with functional defects. As shown in Fig 5.8 (a), in order to insert a line defect in photonic crystal structures, an amplitude mask is placed in the central region of the optical element. The amplitude mask casts a shadow of the central beam on the photoresist. In the shadow region, four side-beams overlap and forms interference patterns in cylinder shape, compare to the woodpile-like pattern by five-beam overlap. However the power of the side beam is more than 3 times smaller than that of the central beam. The intensity of the four-beam interference in the shadow region is less than the threshold needed for photo-polymerization in

92

the photoresist. Or in the other words, the threshold value to have a sustaining structure for 4-beam interference pattern is much higher than the one of 5-beam interference pattern. After exposure, the shadow region can be washed away if we choose a proper amount of develop time and exposure dose. As a proof-of-concept, we put a bar in the central opening as an amplitude mask to fabricate a line defect in 3D photonic crystal template. Using the same experimental conditions as none-amplitude mask case, we fabricate a line defect with a width of approximate 500 μm as shown in Fig. 5.8 (b). Fig.5.8 (c) demonstrate the structures with both 5-beam and 4-beam interference patterns sustained, which corresponds a longer exposure time. Further studies are needed on the diffraction effect of the amplitude mask if small feature sizes of defect shapes are employed in the amplitude mask. Nevertheless this is the first demonstration, to author's best knowledge, of simultaneous fabrication of line defects and 3D photonic crystal template using the one-step HL.

5.2.4 Summary

From the base of bulk top-cut prism setup, in this chapter we have successfully developed a phase tunable five-beam holographic fabrication of 3D photonic crystal template using a single DOE. The mask is designed by fabricated four co-plane diffraction gratings surrounding the opening center. A glass slide is inserted and rotated graduated as a phase modulator for one interfering beam. The fabricated 3D photonic crystal template shows a clear transition of structures from FCT to diamond-like lattice through the phase tuning, as confirmed though SEM images. The demonstrated mask method is compatible with traditional photolithography process used for the optoelectronic chip fabrication and provides a simple way to control holographic interference patterns to fabricate photonic crystal with optimized optical properties.

6.0   3D PHOTONIC QUASI-CRYSTAL TEMPLATES HOLOGRAPHY

FABRICAITON

Large-area 3D Penrose-type photonic quasi-crystals are fabricated through a HL method using a lab-made DOE and a single laser exposure. The DOE consists of five polymer gratings symmetrically orientated around a central opening. The fabricated Penrose-type photonic quasi-crystal shows ten-fold rotational symmetry. The Laue diffraction pattern from the photonic quasi-crystal is observed to be similar to that of the traditional alloy quasi-crystal. A golden ratio of 1.618 is also observed for the radii of diffraction rings.

6.1   INTRODUCTION

In traditional photonic crystals, two-, three-, four- and six-fold rotational symmetries are allowed, however, five-, seven- and higher-fold rotational symmetries are forbidden. It has been shown that photonic quasi-periodic crystals (or called quasi-crystals) have higher rotational symmetries (five, seven, and all high-fold symmetry) and thus more isotropic PBGs leading to more interesting wave propagation properties than traditional photonic crystals. It has been demonstrated experimentally that a complete PBG can be realized in quasi-periodic lattices of small air holes in materials of low

refractive index such as silicon nitride and even glass. This property can enable coupling of light from quasi-crystal device to optical fiber with low optical coupling loss.

In the last decade, several elegant techniques have succeeded in fabricating 3D photonic crystals, such as conventional multilayer stacking of woodpile structures using semiconductor fabrication processes, colloidal self-assembly, multi-photon direct laser writing, and HL. However, some traditional fabrication techniques, such as self-assembly of microspheres [70] and layer-by-layer fabrication [71], are prohibitive for the fabrication of photonic quasi-crystals. Multi-photon lithography and stereo lithography have demonstrated capabilities in the fabrication of 3D icosahedral quasi-crystal but are limited by the large processing time required [72, 73]. HL has been very successful in fabricating photonic crystal templates through multi-beam interference controlled by the number of interfering laser beams, their interfering angle and relative phases. HL has also been used for the fabrication of photonic quasi-crystals [74-78]. 3D icosahedral photonic quasi-crystals are formed via seven-beam interference with five beams five-fold-symmetrically surrounding two oppositely-propagating beams. The single optical element (such as prism or phase mask) based HL has greatly reduced the optics setup complexity and improved the mechanical stability for the micro/nano-fabrication of photonic structures. Through the HL, the interference pattern is usually recorded in a photo-sensitive resist which has a low index of refraction. The photonic quasi-crystal template in polymer can be converted into high refractive index materials such as silicon to have a PBG in crystal. The template can be infiltrated at room temperature with SiO_2 and burned away, leaving behind a daughter "inverse" template. Then, the daughter template is inverted by infiltration with silicon and selective etching of the SiO_2.

In this paper, we demonstrate the laser holographic fabrication of 3D Penrose-type photonic quasi-crystal templates using a lab-made DOE with five gratings oriented five-fold symmetrically.

95

The adaptation of a single DOE to HL drastically reduces the fabrication complexity. The Laue diffraction pattern from the fabricated photonic crystal shows a pentagon-shaped ghost-face like pattern and a golden ratio of 1.618, which have not been observed before in 3D artificial photonic quasi-crystals.

6.2   LAB-MADE DOE BY HOLOGRAPHIC FABRICATION
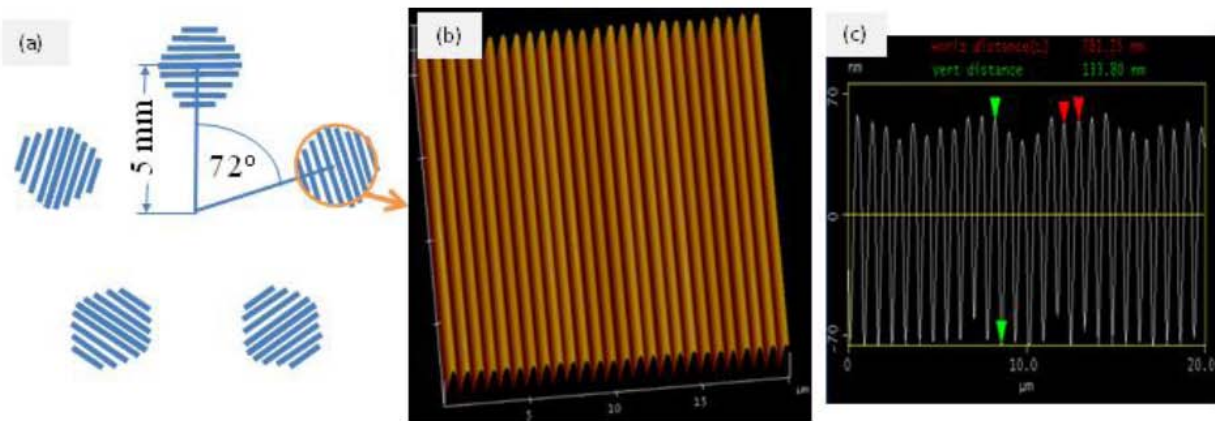
Figure 6.1 (a) the scheme for the lab-made DOE. Each of the five oriented gratings has the structure as imaged by AFM in (b) with a periodicity of 0.781 μm as measured by the section analysis (c).

Figure 6.1(a) shows a scheme of a single DOE consisting of five gratings produced by recording gratings in a photosensitive mixture. A low power laser (Coherent Compass, 532 nm, 60 mW) was used in order to control the exposure condition and thus to obtain high diffraction efficiency. The laser beam was expanded to a size of 5 mm and separated into two by using a 50:50 beam splitter. Two laser beams overlap and form grating in the mixture. The photoresist mixture consists of DPHPA monomer (88.5%), photo initiator rose bengal (0.2%), co-initiator N-phenyl glycine (0.8%)

and chain extender N-vinyl pyrrolidinone (10.5%). The mixture was spin-coated on a microscope glass slide with a speed of 3000 rpm for 2 minutes to produce a thin film. The glass slide was mounted on a rotation stage. The rotation stage was mounted such that the overlapped beams that make up the exposure spot were 5 mm away from the rotation center. The glass slide was rotated by 72 degrees for each successive exposure until a total five gratings were produced. The exposure time was 2s for each exposure. After exposure, the photoresist mixture was developed directly in PGMEA for 20s, followed by rinsing in isopropanol for 10s and air drying. The size of single fabricated grating is approximately 5mm in diameter and the grating shows uniform colors under a white light.

Figure 6.1(b) shows AFM of the fabricated grating in the thin polymer. Figure 6.1(c) shows the section analysis of the measured AFM topography. From the Figs. 6.1(b) and (c), the period of the grating is measured to be 0.781 μm. Thus the fabricated DOE consists of the central opening surrounded by five diffraction gratings orientated five-fold symmetrically. The DOE is mounted in the expanded laser beam and five beams are diffracted by the DOE as shown in Fig. 6.2.

The central beam and five first-order diffracted beams overlap and form 3D interference patterns. The intensity profile of the 6-beam interference pattern can be calculated as

$$I = \left\langle \sum_{i=1}^{6} E_i^2 \right\rangle + \sum_{i<j}^{6} E_i \cdot E_j \cos\left[\left(k_i - k_j\right)r + \Delta\delta_{ij}\right] \tag{6.1}$$

where E and δ are the electric field and initial phase for wave vector k. The wave vector in the Eq. (6.1) can be described by Eqs. (6.2, 6.3),

$$k_0 = K(0, 0, 1) \tag{6.2}$$

$$k_n = K(\sin\alpha\cos\frac{(4n+1)\pi}{10}, \sin\alpha\sin\frac{(4n+1)\pi}{10}, \cos\alpha), \text{ for n} = 1\text{-}5 \tag{6.3}$$

The wave vector difference Δk can be considered as reciprocal vectors of holographically formed structures. The Δk between the five side beams can be described in Eq. (6.4) as

$$\Delta k_n = k_{n-1} - k_{n-2} = 2K \sin \alpha \, \cos(\frac{3\pi}{10})(\cos \frac{2n\pi}{5}, \sin \frac{2n\pi}{5}, 0) \qquad (6.4)$$

This Δk_n is the reciprocal vector for the Penrose quasi-crystal in the x-y plane. After considering k_0, these six beams form 3D structures while the periodicity in z-direction is determined by $k_0 - k_n$.
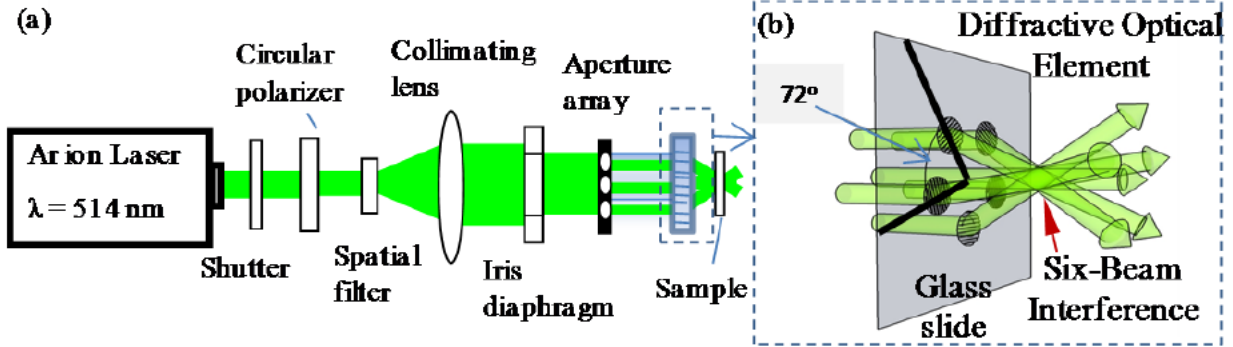
Figure 6.2 (a) Laser experimental setup for the HL; (b) Enlarged view of the lab-made DOE and beam propagation for generating the six-beam interference region for the holographic fabrication of photonic quasi-crystals.

6.3   EXPERIMENTAL RESULTS AND DISCUSSION

As shown in Fig. 6.2(a), the 514.5nm laser beam from an Innova Sabre Ar ion laser (Coherent Inc.) was circularly polarized by a quarter wave-plate, spatially filtered, expanded and collimated. The DOE was mounted before the sample. The DOE produced six-beam interference for the holographic fabrication of the quasi-crystal as shown in Fig. 6.2(b). The five gratings have a first-order diffraction efficiency of 34.9%, 36.9%, 35.1%, 37.1% and 35.0%, respectively. The same photosensitive

mixture as the one in previous section was used. The spin-coating speed was 1000 rpm and the sample thickness was around 10 μm. A laser power of 500 mW was used with an exposure time of several seconds. After the exposure, the sample was developed in PGMEA for six minutes, typically. A magnetic bar with a speed of 60 rpm was used to stir the PGMEA developer. Finally the sample was washed with isopropanol for 20s and left to dry in ambient air. The developed sample had a size of approximately 4.5 mm in diameter. The edge of the sample was thinner than the central area as observed under an optical microscope. The central area with a size of around 3.5 mm in diameter was homogeneous as determined by scanning the 532 nm laser cross the sample and observing the diffraction pattern from the sample. The diffraction pattern from the central area of the sample showed not only high rotation symmetry but also detailed fine structures as discussed later in the section. The diffraction from the edge part of the sample did show the high rotational symmetry however detailed fine structure disappeared.

Figure 6.3(a) shows an SEM of photonic quasi-crystal fabricated by exposing the photosensitive mixture to the six-beam interference. A simulation is overlaid in the SEM for comparison and fits the SEM very well. Local five-fold symmetry is clearly observed as there are many pentagons in the SEM. For eye guidance, four pentagons were drawn in the figure with two of them around a common vertex. This five-fold symmetry is incompatible with translational crystallography. Surface undulations are apparent in Fig. 6.3(a), which might be caused by uneven laser beam intensities diffracted from gratings with different heights in Fig. 6.1(c). Figure 6.3(b) shows an enlarged SEM view of the photonic quasi-crystal fabricated through the six-beam interference. 3D structures and ten-fold symmetry are obvious.
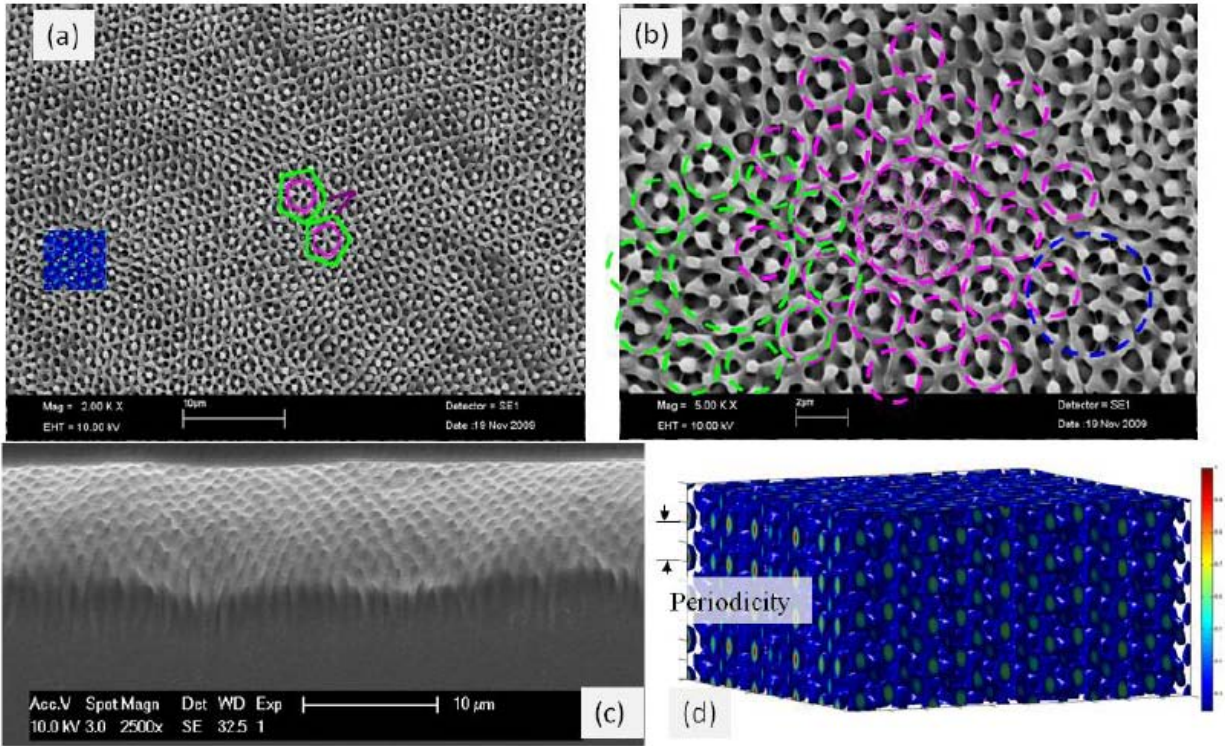
Figure 6.3 (a, b) SEM image of the holographically formed photonic quasi-crystal at both large (a) and small (b) scales. (a) Inserts are simulation on the right side and eye-guidance pentagons in the middle. (b) Overlay geometries provide eye-guidance in establishing the symmetry and tiling. (c) SEM image of cross-section of the holographically formed photonic quasi-crystal and (d) the simulation of formed 3D structures.

The large-area SEM structures can be constructed 10-fold symmetrically by a small block with five-fold symmetry (represented by a small circle for simplicity). Ten magenta light-line circles can represent structures inside the large magenta circle. Outside the large magenta circle, ten small magenta circles can represent the structure next to the large circle. The diameter of the small circle is measured to be approximately 1 μm. The refractive index of the photosensitive mixture is estimated to be 1.5. The size of the circle due to the first order reciprocal vector Δk_n is calculated to be 0.997 μm, which is very close to the measured value. SEM cross-section view of the fabricated photonic quasi-crystal is shown in Fig. 6.3(c) and theoretic simulation is shown in Fig. 6.3(d). The SEM in Fig.

6.3(c) was taken in a flip-over sample with photonic structures developed through 10 μm thickness down to the glass substrate. The sample close to the substrate looks over-exposed due to the back-reflection of laser beams from the glass substrate surfaces. Photonic structures in z-direction are determined by k_0-k_n and periodic in z-direction as shown in Fig. 6.3(d). The periodicity is $\lambda/(1-\cos\alpha)$ and is calculated to 2.08 μm. The measurement is performed in areas which appear to be in vertical direction to the surface in Fig. 6.3(c). The measured periodicity is 1.99 μm. The smaller measured value than that calculated might be due to the shrinkage of the sample.
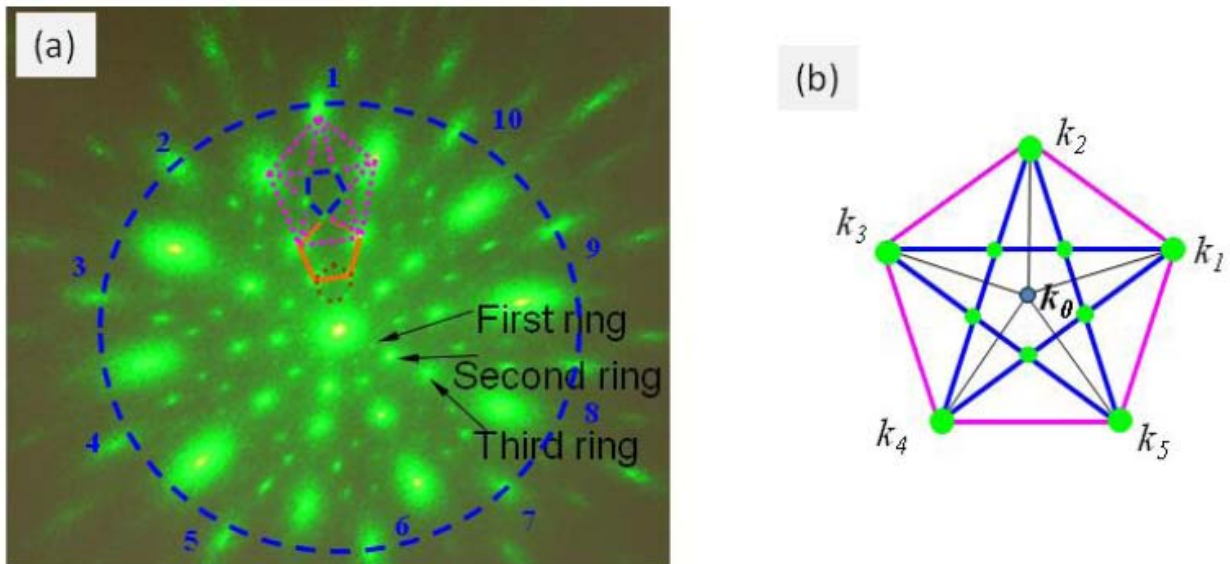
Figure 6.4 (a) Laue diffraction pattern from the photonic quasicrystal using 532nm laser. The diffraction spots are connected using pentagon and form ghost-face like pattern. (b) Projections of the wave vectors (black) on the plane perpendicular to the k0 direction. The first and second order reciprocal vectors are represented by pink lines and blue lines, respectively.

Figure 6.4(a) shows the Laue diffraction pattern from the photonic quasi-crystals in wholly patterned samples on the glass substrate, using the Coherent Compass 532 nm laser. The diffraction pattern is formed on a white paper behind the quasi-crystal and the digital image is taken behind the

white paper. The size of the spot is a measure of the diffraction intensity. The ten-fold symmetry is clearly shown in the diffraction pattern, which is typical for Penrose or icosahedral quasi-crystals. The diffraction pattern can be explained by the first and second order reciprocal vectors as drawn in Fig. 6.4(b). The five wave-vectors for the five side beams are arranged five-fold symmetrically around the central wave-vector k_0. Several pentagons have been drawn in Fig. 6.4(a) for eye-guidance and, actually, are similar to the pentagon arrangement in Fig. 6.4(b). The high-intensity diffraction spots are formed due to the first order reciprocal vectors such as k_1-k_2. Five low-intensity diffraction spots are surrounded by the high-intensity spots and form pentagons (see ghost-face in Fig. 6.4(a)), due to the second order reciprocal vectors such as k_1-k_3 and k_2-k_4 (see Fig. 6.4(b)). The diffraction pattern from the fabricated photonic quasi-crystal is similar to the one obtained in quenched alloy quasi-crystals with icosahedral structure [79, 80], and also in agreement with the calculated diffraction pattern from the icosahedral photonic quasi-crystal, although the structure is formed through six-beam interference instead of seven-beams. Their diffraction intensity distributions are also similar [80]. Seen away from the zero-th order diffraction, there are ten spots forming first, second and third rings, respectively. The ratio of radii of the third and second rings to the first ring is measured to be 2.6 and 1.6, respectively, which are very close to the ratio of $1 + 1.618$ and 1.618 where 1.618 is golden ratio. The golden ratio is a characteristic of Penrose or icosahedral quasi-crystals and thus the observation of a golden ratio demonstrates the high-quality of fabricated photonic quasi-crystal.

6.4   SUMMARY

In summary, we demonstrated a holographic fabrication of a large-area 3D Penrose-type photonic quasi-crystal using the lab-made DOE. The DOE was fabricated through two-beam interference in a polymer and consisted of five polymer gratings rotationally orientated symmetrically around a central opening on a glass slide substrate. The five first-order diffracted beams and the central beam formed the interference pattern for a single-exposure based recording of the photonic quasi-crystal in a polymer. The use of the DOE for the HL has greatly improved the optics alignment accuracy and mechanical stability. High quality 3D photonic quasi-crystals have been fabricated with ten-fold symmetry in the x-y plane, similar to a Penrose quasi-crystal. The Laue diffraction pattern from the 3D photonic quasi-crystal was observed to be similar to the traditional alloy quasi-crystal and a golden ratio of 1.618 was also observed for the diffraction rings, which have not been observed before in 3D artificial photonic quasi-crystals. The photonic quasi-crystal in polymer can be double inverted to silicon structure for the opening of the PBG.

7.0   3D PHOTONIC CRYSTAL WITH DEFECT STRUCTURES

This chapter presents the capability of direct laser writing of complex defect structures in holographically formed 3D photonic crystals in DPHPA monomers mixed with photo-initiators. The 3D photonic crystal template was fabricated through single optical element-based HL. Waveguide and letter structures are fabricated through the two-photon polymerization excited by a femtosecond laser oscillator. The strengths of two optical lithographic techniques are combined with HL providing a rapid and large area micro-fabrication and two-photon lithography (TPL) providing flexible defect structure fabrication. The optical fabrication process is simplified in the negative tone DPHPA without pre-bake and post-exposure bake. Similar to SU8, DPHPA also demonstrates a capability for constructing 3D structures with high aspect ratio and small feature.

7.1   INTRODUCTION

The semiconductor processing techniques provide advanced tools for building structure layer-by-layer and incorporating defects at any depth. Most of the direct laser writing was based on two-photon polymerization of photosensitive resins. When a high-intensity light shines on a material, the probability for two-photon absorption is proportional to the square of the optical field

intensity, and thus is greatest at the center of a Gaussian laser beam. When tightly focused into the volume of a photosensitive resin, the polymerization process can be initiated by nonlinear absorption of near infrared femtosecond laser pulses within the focal volume. By moving the laser focus three-dimensionally through the resin, the two-photon polymerization happens at the focus points. 3D structures and defects such as missing rod in woodpile structure can be fabricated by a computer-aided sample stage control [81]. The photonic crystal structures fabricated by above two approaches are dedicated but the process are time-consuming. Fabrication of defects in self-assembled opal photonic crystal has made headway by surface modification followed by overgrowth of opal [82] or laser direct writing of defect structures within the opal [83, 84]. However, opal photonic crystals were limited to FCC structures with a relative small photonic bandgap.

Multi-beam interference-based HL has been successful for fabricating 3D photonic crystals by exposing a photoresist or polymerizable resin to interference patterns of laser beams. In the case of positive resist, the overexposed material is then dissolved away in the post-exposure processing. The underexposed region forms a periodic network and acts as a 3D photonic crystal template. For negative photoresists, the underexposed regions can then be selectively removed using a developer while overexposed region becomes polymerized and forms a periodic network for photonic crystal template. Furthermore, HL has demonstrated functionality to fabricate complex photonic structures such as woodpile, spiral and diamond photonic crystals. Multiple-beam HL was complicated when it was based on multiple bulk optical elements such as mirrors and beam splitters. Recently the optical setup for HL has been simplified by using a single optical element such as flat-top prism or a phase mask. Multi-layer phase masks have been demonstrated for the fabrication of photonic crystal templates by

introducing a phase difference among the diffracted beams through changing the distance between two orthogonally oriented gratings. These single-beam and single-exposure processes using the multi-layer mask in HL have drastically reduced the fabrication complexity. The disadvantage is that a change in wavelength is required in order to obtain a different lattice period, which can also compromise the resist photochemistry. On the other hand, Meisel et al. have demonstrated that a simple cubic photonic crystal, with a wide variety of lattice spacing, can be fabricated with a single free-space beam splitter, using three separate two-beam exposures, with no change in wavelength [85]. To be useful for optoelectronics applications, the incorporation of engineered defects must be realized in photonic crystal. A significant advance has been achieved on the simultaneous fabrication of functional defects in photonic crystal templates by using a multi-beam phase-controlled one-step HL and by combining the amplitude mask with the phase mask. However, the process still needs to be improved to increase the functionality of the photonic crystal devices.

The strength of HL and TPL can be combined by using the HL for a rapid and flexible fabrication of 3D host photonic crystals and using TPL for creating desired defects in photonic crystals, which in principle, can be placed in any depth with any shape. Two-photon ablation or polymerization was used to create defects in photonic crystal template in SU8, which were created through HL, by three research groups in 2005, 2006and 2008. Sun et al. demonstrated the hybrid holographic and direct-writing method in a two-dimensionally periodic structure while Scrimgeour et al. described the creation of a buried waveguide structure that is commensurate with the photonic crystal matrix. The other group fabricated and developed polymer-air photonic crystals in SU8 via HL and the photonic crystals were infiltrated with trimethylol propane triacrylate (TMPTA) and a two-photon sensitive photoinitiator for the direct writing of defects

via ultrafast laser. Nice defects with a size of several lattice constants were demonstrated. These three groups used SU8 photoresist for the holographic fabrication. The SU8 usually requires pre-bake and post-exposure bake although it is an excellent resist for fabricating nano/mcro-structures with high aspect ratio.

In this chapter we use a different photosensitive mixture of DPHPA and photoinitiator for the hybrid HL and TPL without pre-bake and post-exposure bake. A phase-tunable single optical element is used for the holographic fabrication of large-area woodpile-type photonic crystal template in order to reduce the optics setup complexity. The TPL is demonstrated in the same photosensitive mixture without an infiltration of other photosensitive mixture. We create complex defect structures including letters and waveguide through direct-writing in the 3D holographically formed photonic crystal template.
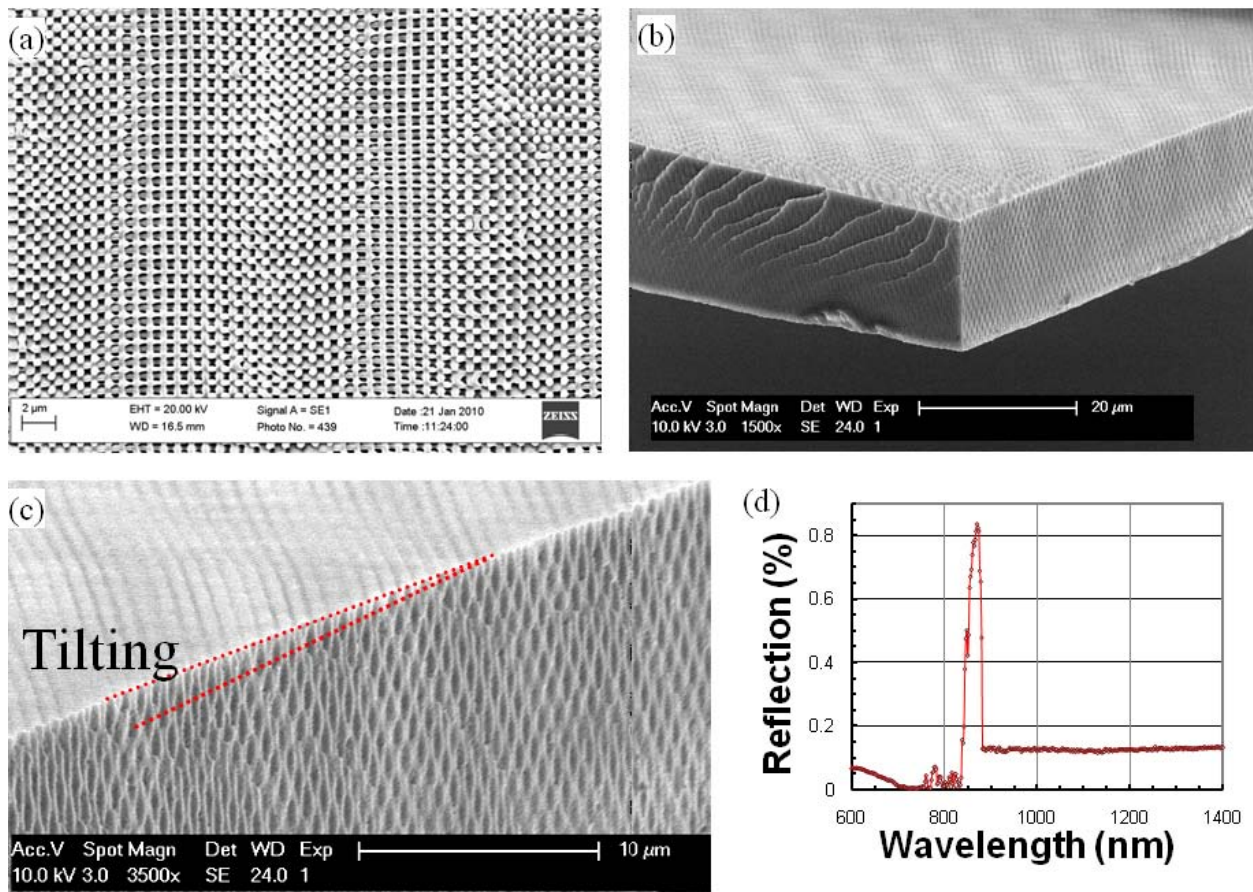
Figure 7.1 (a) SEM of fabricated 3D photonic crystal template through HL; (b) Cross-section SEM image of the fabricated photonic crystal; (c) Enlarged view of the cross-section; (d) The reflection spectrum from the fabricated photonic crystal measured by ellipsometery.

7.2   3D PHOTONIC STRUCTURES HOLOGRAPHIC FABRICATION

A 514.5nm laser beam from a Sabre Ar ion laser (Coherent Inc.) was used for the five-beam interference based holography lithography. The laser beam was circularly polarized, cleaned, expanded and collimated by spatial filter and collimating lens set. A phase-tunable single optical

element (top-cut four-side-prism) was used to construct five-beam interference pattern as described in reference 26. 3D photonic crystals were fabricated holographically in a negative tone photosensitive mixture mainly monomer DPHPA and photoinitiator Rose Bengal. The photosensitive mixture was spin-coated as a thin film on a cut glass-slide. The spin-coating speed was between 800 and 2000 rpm and the sample thickness was between 6 and 18 μm. A laser power around 250 mW was used. The exposure time was around 15 seconds. After the exposure, the photoresist was developed in propylene glycol methyl ether acetate for several hours and then washed by isopropanol for 20 seconds and left to dry in ambient air. The developed holographic sample has a surface area of 3.5x3.5 mm^2.

Figure 7.1(a) shows an SEM image of photonic structures developed in the photoresist, showing the quality of woodpile structure fabricated through HL. The cross-section of the fabricated sample is shown in Fig. 7.1(b) and an enlarged view is shown in Fig. 7.1(c). The photonic structure is determined by the wave vector k of the five beams as described by Eq. (7.1) and (7.2),

$$k_0 = K(0, 0, 1) \tag{7.2}$$

$$k_n = K(\sin \alpha \cos \frac{4n\pi}{8}, \sin \alpha \sin \frac{4n\pi}{8}, \cos \alpha), \text{ for n} = 1\text{-}4, \tag{7.3}$$

where is the interference angle between the side-beam k_n and the central-beam k_0. The wave vector difference k can be considered as reciprocal vectors of holographically formed structures. The periodicity in x or y direction is λ/sinα which is calculated to 0.84μm for α=37.5^o. The periodicity is measured to be 0.83μm averaged over several SEMs. The periodicity in z-direction is $\lambda_m/(1-\cos\alpha_m)$=4.21 μm assuming the refractive index is 1.58 for the photoresist (subscript m for value inside the mixture). The measured value is 3.96 μm which is smaller than theoretic one. The difference might be due to the sample shrinkage. The wavelike long period banding in the

surface of the structure in Fig. 7.1(a) and (b) is caused by a small sample tilt as illustrated in Fig. 7.1(c).

Fig. 7.1(d) shows the reflection spectrum from the fabricated photonic crystal measured by ellipsometery with incident angle of 70o. There is a strong reflection peak around 870 nm. A reflection peak around 940 nm due to stop-band was reported for photonic crystal with lattice parameters of 763 nm in plane and 789 nm out of plane by Shir et al. [20]. For the photonic crystal shown in Fig. 7.1, there are 4 layers structures in one period in z-direction. Considering that the distance between the layers is 0.99 μm and lattice parameter in plane is 0.83 μm which are similar to these values reported by Shir et al. [20], it is reasonable to assign the peak in Fig. 7.1(d) as the reflection due to the stop-band in the photonic crystal.
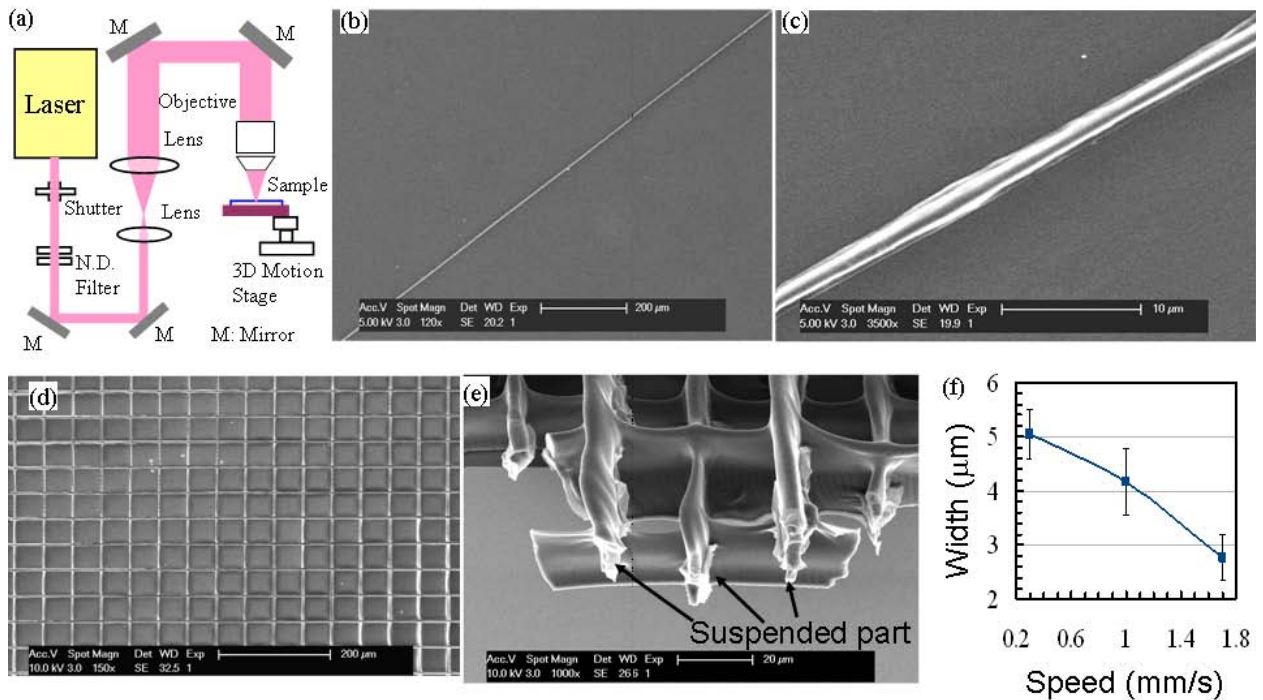
Figure 7.2 (a) Experimental setup for TPL. (b) Large area SEM image of the two-photon polymerization induced waveguide on glass substrate; (c) Enlarged SEM view of the waveguide on glass substrate; (d) SEM of woodpile structure constructed by arranging the waveguide into several layers; (e) SEM of suspended waveguides by cutting the woodpile structure; (f) Line width of structures fabricated at three scanning speeds.

7.3   TWO-PHOTO POLYMERIZATION THROUGH LASER DIRECT WRITING

Figure 7.2(a) shows the laser direct writing setup. A tunable Ti: Sapphire femtosecond laser oscillator (Chameleon, Coherent Inc.) was used with a repetition rate of 80 MHz and pulse width of 140 fs. The laser operation wavelength is 720 nm. The laser beam was controlled through an external shutter and the laser power was attenuated through neutral density filters. The laser beam was expanded and then focused inside the photoresist using a 0.55 NA aspheric lens (Thorlabs). The laser power was 150 mW as measured before the aspheric lens. The photoresist was spin-coated on a glass slide and the slide was mounted on a three axial motion stage (Newport) which was controlled with a computer and translated with a constant speed of 2.4 mm/s. The same photoresist mixture and spin-coating on the glass slide were used as described in the above section. After the laser direct writing, the photoresist was developed in propylene glycol methyl ether acetate and then washed by isopropanol. Fig. 7.2(b) shows a large area SEM image of the direct laser written waveguide standing on the glass slide substrate generated using the TPL method. It is clearly shown that the two-photon polymerization can be realized in the DPHPA mixture by the Ti: sapphire oscillator instead of an expensive ultrafast laser amplifier system. Fig. 7.2(c) shows an enlarged SEM image of the fabricated waveguide on the glass substrate. From the figure, we can see that the waveguide has clean surface and a width of 2.3 μm.

In order to measure the true aspect ratio, defect lines are arranged in the form of woodpile for several layers as shown in Fig. 7.2(d). Then we cut the woodpile and measure the size and

aspect ratio of defect lines for suspended part (see Fig. 7.2(e)). The aspect ratio is measured to be approximately 4. It demonstrates that DPHPA can be used for constructing microstructure with high aspect ratio. On the other hand, the aspect ratio can be reduced through laser beam shaping and controlling beam scanning direction. Fig. 7.2(f) shows the line width changes for three scanning speeds. As the scanning speed increases, the line width decreases. Further detailed studies will be performed for line width as a function of laser pulse energy, wavelength and scanning speed.
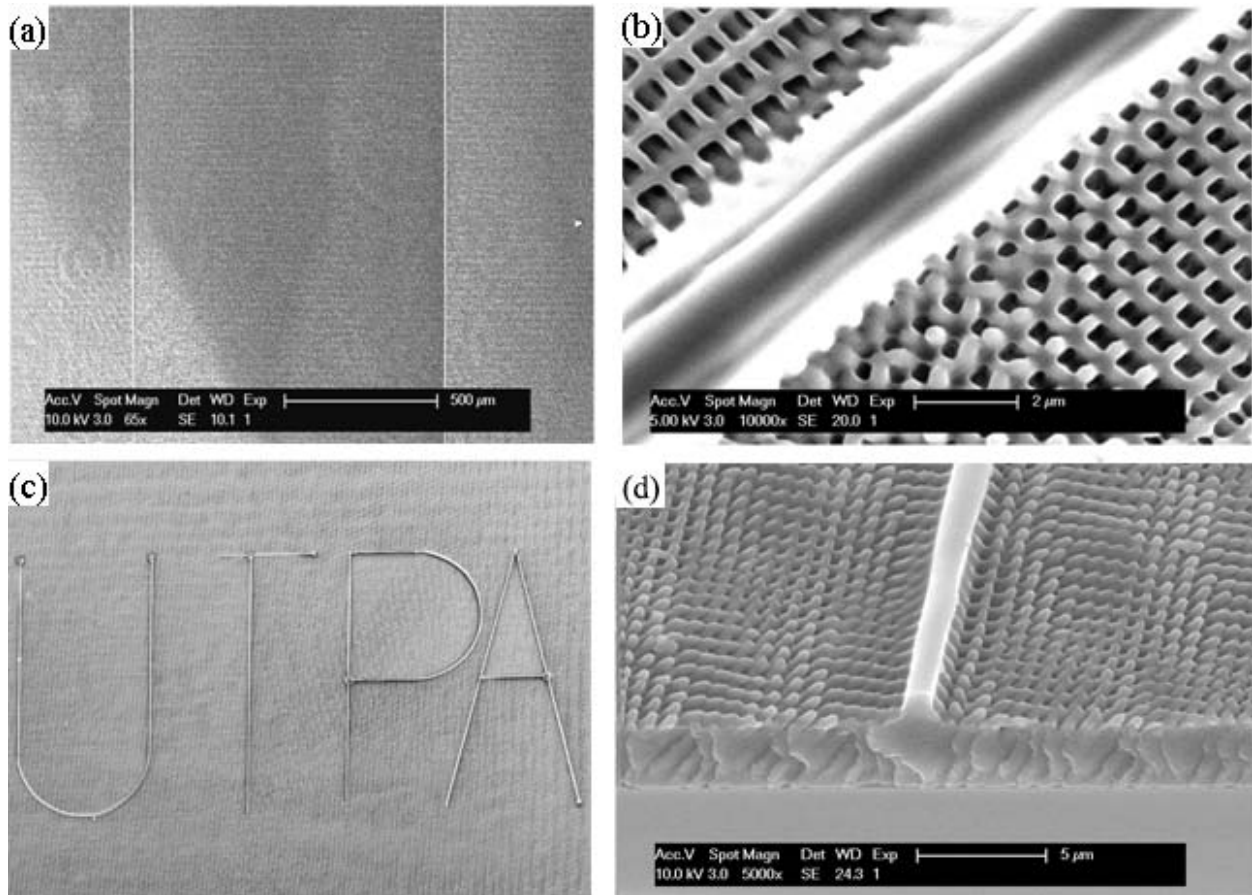
Figure 7.3 (a) Large area SEM image of waveguides fabricated in holographic photonic crystal template; (b) An enlarged view of SEM image of waveguide in 3D photonic crystal template; (c) Defect structures in UTPA letters are fabricated in 3D photonic crystal template; (d) SEM cross-section of a sample fabricated through hybrid holographic and TPL methods.

7.4   DEFECT STRUCTURES IN 3D PHOTONIC CRYSTAL

The strength of above optical lithography techniques can be utilized for the fabrication of 3D photonic crystals with defects. As a demonstration, Fig. 7.3 shows defect structures fabricated in the 3D photonic crystal template by combining the above two optical-lithography methods. The spin-coated photoresist film was firstly exposed to the Ar ion laser for the HL. After initial exposure, the glass slide is then mounted on the computer controlled motion stage. Then the femtosecond laser pulses were focused inside the previously holographically exposed resist. The motion stage was controlled such that the focal point moves across the undeveloped photonic crystal region. The same motion speed of 2.4 mm/s was used. After exposure, the photoresist was developed in propylene glycol methyl ether acetate for six minutes and then washed with isopropanol for 20 seconds and left to dry in ambient air. Fig. 7.3(a) shows the large scale uniformity while Fig. 7.3(b) shows the interfacial quality of the two lithography processes. The width of the waveguide is approximately 3 μm. Although the waveguide is not in alignment with the lattice, it might be not essential because theoretic simulations have demonstrated an existence of guide mode for zig-zag defects in photonic crystal.

A complicated structure can also be fabricated with the TPL. Fig. 7.3(c) shows defect structures of UTPA letters fabricated in the 3D photonic crystal template, which clearly demonstrates the capability of direct laser of complex structure through the TPL in holographic structure. The fabrication of completely buried waveguide in photonic crystal has been performed. Fig. 7.3(d) shows SEM of one sample fabricated through hybrid holography and

direct-writing method. Further characterization can be done through optical fiber butt coupling and CCD imaging or by adding fluorescent dye into the photosensitive mixture for imaging.

7.5   SUMMARY

In summary, this chapter demonstrated the capability of optical fabrications of photonic crystals with defect structures in DPHPA instead of SU8 through a simplified lithographic process without pre-bake and post-exposure bake. The flat-top four-side prism-based HL was used for the rapid fabrication of large area 3D photonic crystal templates with woodpile-type structure. TPL was capable to write complex defect structures in the holographically formed 3D photonic crystals in DPHPA with a clear interfacial connection. Thus DPHPA can be used for HL, laser direct-writing, hybrid holographic and TPL and constructing nano/micro-structures with high aspect ratio.

8.0   CONCLUSION

In this dissertation we provide design approaches of holographic fabrication 3D photonic crystal templates by using sequential phase masks as the DOE tools. The structure and symmetry of the photonic crystal formed can be controlled by modulation of the rotational angle, elongation in lattice length or the phase difference of the interfering beams.

First of all, we report the fabrication of both orthorhombic and tetragonal woodpile photonic crystal using a 1D phase mask technique. 3D photonic crystal structures were formed by a double exposure process. Secondly, we also demonstrate holographic fabrication of 3D diamond-like photonic crystal template using a single 2D lab-made phase mask. The superposition of two interference FCC or FCT patterns through double exposure yields diamond-like structure. Thirdly, based on the 2D phase mask fabrication technique, we introduce an integrated two-layer phase mask to reduce the required times of exposure. A 3D photonic crystal template was fabricated by only single exposure through the two-layer phase mask and without further spatial operations. At last, we introduce new phase tuning ability to our optical elements. A simultaneous fabrication of the line defect and 3D photonic crystal templates is also demonstrated by combining the amplitude mask with the phase mask, using the one-step HL.

The utilization of the DOE simplifies the fabrication configuration of 3D photonic crystals and is amendable for massive lithography production. The demonstrated approaches are compatible with traditional photolithography processes used for chip-scale optoelectronic integration.

APPENDIX

MATLAB SIMULATION FOR FIVE-BEAM INTERFERENCE PATTERN

VIRTULIZATION

```matlab
%Five-beam interference pattern with phase shift
clear all
clc
clf

shift=0;

firstorder = 42.8; %angle 19.8 of first order diffraction in SU-8 mixture
using n = 1.67

lamb = 0.5145e-6; %free space wavelength

angle = 90;

%%%%%%%%%%%%%%%%%%%%%%%%%%%%%%%%%%%%%%%%%%%%%%%%%%%%%%%%%%%%%%%%%%%%%%

xs=0.;
x = (xs:0.2:xs+8)*1e-6;
ys=0;
y = (ys:0.2:ys+8)*1e-6;
zs=4;
z = (zs:0.3:zs+3)*1e-6;

k1 = 2*pi/lamb; k2 = k1; k3 = k1; k5 = k1; k6=k1;
k1x = 0; k1y = 0; k1z = k1;

%%%%%%%%%%%%%%%%%%%%%%%%%%%%%%%%%%%%%%%%%%%%%%%%%%%%%%%%%%%%%%%%%%%%%%%%%


% diffraction intensities setup

E1o=sqrt(5); % central beam
E2o=1;
E3o=1;
E5o=1;
```

```matlab
E6o=1;


%%%%%%%%%%%%%%%%%%%%%%%%%%%%%%%%%%%%%%%%%%%%%%%%%%%%%%%%%%%%%%%%%%%%%%%%%
%k-vector geometry for k2
theta = (shift)*pi/180;
phi = (90-firstorder)*pi/180;
%the function sph2cart converts from spherical to cartesian
% returning its coresponding x y z components
[k2x,k2y,k2z] = sph2cart(theta,phi,k2);

%k-vector geomety for k3
theta = (shift)*pi/180;
phi = (90+firstorder)*pi/180;
[k3x,k3y,k3z] = sph2cart(theta,phi,k3);
%%%%%%%%%%%%%%%%%%%%%%%%%%%%%%%%%%%%%%%%%%%%%%%%%%%%%%%%%%%%%%%%%%%%%%%%%
%k-vector geometry for k5
theta = (shift+angle)*pi/180;
phi = (90-firstorder)*pi/180;
[k5x,k5y,k5z] = sph2cart(theta,phi,k5);

%k-vector geometry for k6
theta = (shift+angle)*pi/180;
phi = (90+firstorder)*pi/180;
[k6x,k6y,k6z] = sph2cart(theta,phi,k6);
%%%%%%%%%%%%%%%%%%%%%%%%%%%%%%%%%%%%%%%%%%%%%%%%%%%%%%%%%%%%%%%%%%%%%%%%%%

phase_retard=1*180;  % <-----  here is the phase shift

polar_angle1=45;
polar_angle2=45;

%%%%%%%%%%%%%%%%%%%%%%%%%%%%%%%%%%%%%%%%%%%%%%%%%%%%%%%%%%%%%%%%%%%%%%%%%%

for j = 1:length(x)
   for v = 1:length(y)
      for l=1:length(z)
            E1(j,v,l) =
cosd(polar_angle1)*E1o*exp(i*((k1x*x(j)+k1y*y(v)+k1z*z(l))));  % center beam
            E2(j,v,l) =
cosd(polar_angle1)*E2o*exp(i*((k2x*x(j)+k2y*y(v)+k2z*z(l))+phase_retard*pi/18
0)); % side -left
            E3(j,v,l) =
cosd(polar_angle1)*E3o*exp(i*((k3x*x(j)+k3y*y(v)+k3z*z(l))));      % side  -
right
            E5(j,v,l) =
cosd(polar_angle2)*E5o*exp(i*((k5x*x(j)+k5y*y(v)+k5z*z(l))));      % top
            E6(j,v,l) =
cosd(polar_angle2)*E6o*exp(i*((k6x*x(j)+k6y*y(v)+k6z*z(l))));      % bottom


      end
   end
end


%%%%%%%%%%%%%%%%%%%%%%%%%%%%%%%%%%%%%%%%%%%%%%%%%%%%%%%%%%%%%%%%%%%%%%%%%%
```

```matlab
Et =(E1+E2+E3+E5+E6);

It = abs(Et).^2;
It = It./max(max(max(It)));
Iti=1-It;

level=0.5; % exposure threshold value




figure(1)
data = smooth3(It,'box',1);
p1 = patch(isosurface(x,y,z,data,level), ...
    'FaceColor','blue','EdgeColor','none');
p2 = patch(isocaps(x,y,z,data,level), ...
     'FaceColor','interp','EdgeColor','none');
isonormals(x,y,z,data,p1);

view(3); axis equal; axis off; %tight vis3d; axis off;
%title('/D/d=0\pi','FontName','Times New Roman','FontSize',24);

camlight; lighting phong; material shiny;
```

BIBLIOGRAPHY

[1]   Keyes, R.W., *Fundamental limits of silicon technology.* Proceedings of the IEEE, **89**(3): p. 227-239. 2001.

[2]   John, S., *Strong localization of photons in certain disordered dielectric superlattices* Phys. Rev. Lett., **58**(23): p. 2486. 1987.

[3]   Yablonovitch, E., *Inhibited Spontaneous Emission in Solid-State Physics and Electronics.* Phys. Rev. Lett., **58**(20): p. 2062. 1987.

[4]   Joannopoulos, J.D., P.R. Villeneuve, and S.H. Fan, *Photonic crystals: Putting a new twist on light (vol 386, pg 143, 1997).* Nature, **387**(6635): p. 830-830. 1997.

[5]   Divliansky, I., et al., *Fabrication of three-dimensional polymer photonic crystal structures using single diffraction element interference lithography.* Applied Physics Letters, **82**(11): p. 1667-1669. 2003.

[6]   Poole, Z., et al., *Holographic fabrication of three-dimensional orthorhombic and tetragonal photonic crystal templates using a diffractive optical element.* Appl. Phys. Lett., **91**(25): p. -. 2007.

[7]   Lin, Y.K., et al., *Five beam holographic lithography for simultaneous fabrication of three dimensional photonic crystal templates and line defects using phase tunable diffractive optical element.* Optics Express, **17**(19): p. 16625-16631. 2009.

[8]   Xu, D., et al., *Phase tunable holographic fabrication for three-dimensional photonic crystal templates by using a single optical element.* Applied Physics Letters, **94**(23): p. -. 2009.

[9]   Chan, T.Y.M., O. Toader, and S. John, *Photonic band gap templating using optical interference lithography.* Physical Review E, **71**(4): p. -. 2005.

[10] Campbell, M., et al., *Fabrication of photonic crystals for the visible spectrum by holographic lithography.* Nature, **404**(6773): p. 53-56. 2000.

[11] Lin, Y.K., D. Rivera, and K.P. Chen, *Woodpile-type photonic crystals with orthorhombic or tetragonal symmetry formed through phase mask techniques.* Optics Express, **14**(2): p. 887-892. 2006.

[12] Joannopoulos, J.D., *Photonic Crystals*: Princeton Press. 1995.

[13] Satoh, H., N. Yoshida, and Y. Miyanaga, *Analysis of polarization plane rotation characteristic in 2D photonic crystal waveguide with chiral medium by condensed node spatial network.* Electrical Engineering in Japan, **152**(1): p. 7-14. 2005.

[14] Shi, S.Y., C.H. Chen, and D.W. Prather, *Plane-wave expansion method for calculating band structure of photonic crystal slabs with perfectly matched layers.* Journal of the Optical Society of America a-Optics Image Science and Vision, **21**(9): p. 1769-1775. 2004.

[15] Qiu, M. and S.L. He, *A nonorthogonal finite-difference time-domain method for computing the band structure of a two-dimensional photonic crystal with dielectric and metallic inclusions.* Journal of Applied Physics, **87**(12): p. 8268-8275. 2000.

[16] Hess, O., C. Hermann, and A. Klaedtke, *Finite-Difference Time-Domain simulations of photonic crystal defect structures.* Physica Status Solidi a-Applied Research, **197**(3): p. 605-619. 2003.

[17] Wu, L. and S.L. He, *Revised finite-difference time-domain algorithm in a nonorthogonal coordinate system and its application to the computation of the band structure of a photonic crystal.* Journal of Applied Physics, **91**(10): p. 6499-6506. 2002.

[18] Yee, K.S., *Numerical solution of initial boundary value problems involving Maxwell's equations in isotropic media.* IEEE Trans. Antennas Propagat., **14**. 1966.

[19] Li, M., et al., *Higher-order incidence transfer matrix method used in three-dimensional photonic crystal coupled-resonator array simulation.* Optics Letters, **31**(23): p. 3498-3500. 2006.

[20] Li, Z.Y. and K.M. Ho, *Application of structural symmetries in the plane-wave-based transfer-matrix method for three-dimensional photonic crystal waveguides.* Physical Review B, **68**(24): p. -. 2003.

[21] Brechet, F., et al., *Complete analysis of the characteristics of propagation into photonic crystal fibers, by the finite element method.* Optical Fiber Technology, **6**(2): p. 181-191. 2000.

[22] Xiao, S.S., L.F. Shen, and S.L. He, *A plane-wave expansion method based on the effective medium theory for calculating the band structure of a two-dimensional photonic crystal.* Physics Letters A, **313**(1-2): p. 132-138. 2003.

[23] Joannopoulos, J.D., *MIT Photonic-Bands (MPB) package.*

[24] Povey, I.M., et al., *Photonic crystal thin films of GaAs prepared by atomic layer deposition.* Applied Physics Letters, **89**(10): p. -. 2006.

[25] Knight, J.C., et al., *All-silica single-mode optical fiber with photonic crystal cladding.* Optics Letters, **21**(19): p. 1547-1549. 1996.

[26] Nishimura, N., Y. Awatsuji, and T. Kubota, *Two-dimensional arrangement of spatial patterns representing numerical data in input images for effective use of hardware resources in digital optical computing system based on optical array logic.* Journal of Parallel and Distributed Computing, **64**(9): p. 1027-1040. 2004.

[27] Adibi, A., et al., *Design of photonic crystal optical waveguides with singlemode propagation in the photonic bandgap.* Electronics Letters, **36**(16): p. 1376-1378. 2000.

[28] Lin, S.Y., et al., *Experimental demonstration of guiding and bending of electromagnetic waves in a photonic crystal.* Science, **282**(5387): p. 274-276. 1998.

[29] Schonbrun, E., et al., *Polarization beam splitter based on a photonic crystal heterostructure.* Optics Letters, **31**(21): p. 3104-3106. 2006.

[30] Liu, T., et al., *Design of a compact photonic-crystal-based polarizing beam splitter.* Ieee Photonics Technology Letters, **17**(7): p. 1435-1437. 2005.

[31] Douay, M., et al., *Formation of Bragg Gratings in Germanium Doped Optical Fibers Using a Prism Interferometer.* Journal De Physique Iv, **1**(C7): p. 529-532. 1991.

[32] Akahane, Y., et al., *High-Q photonic nanocavity in a two-dimensional photonic crystal.* Nature, **425**(6961): p. 944-947. 2003.

[33] Yanik, M.F., et al., *All-optical transistor action with bistable switching in a photonic crystal cross-waveguide geometry.* Optics Letters, **28**(24): p. 2506-2508. 2003.

[34] Wu, X., et al., *Ultraviolet photonic crystal laser.* Applied Physics Letters, **85**(17): p. 3657-3659. 2004.

[35] Wu, L.J., et al., *Superprism phenomena in planar photonic crystals.* Ieee Journal of Quantum Electronics, **38**(7): p. 915-918. 2002.

[36] Zhang, X., *Absolute negative refraction and imaging of unpolarized electromagnetic waves by two-dimensional photonic crystals.* Physical Review B, **70**(20): p. -. 2004.

[37] Braun, P.V. and P. Wiltzius, *Macroporous materials - electrochemically grown photonic crystals.* Current Opinion in Colloid & Interface Science, **7**(1-2): p. 116-123. 2002.

[38] Wierer, J.J., et al., *InGaN/GaN quantum-well heterostructure light-emitting diodes employing photonic crystal structures.* Applied Physics Letters, **84**(19): p. 3885-3887. 2004.

[39] Sugimoto, Y., et al., *Fabrication and characterization of different types of two-dimensional AlGaAs photonic crystal slabs.* Journal of Applied Physics, **91**(3): p. 922-929. 2002.

[40] Painter, O., et al., *Two-dimensional photonic band-gap defect mode laser.* Science, **284**(5421): p. 1819-1821. 1999.

[41] Lin, S.Y., et al., *A three-dimensional photonic crystal operating at infrared wavelengths.* Nature, **394**(6690): p. 251-253. 1998.

[42] Deubel, M., et al., *Direct laser writing of three-dimensional photonic-crystal templates for telecommunications.* Nature Materials, **3**(7): p. 444-447. 2004.

[43] Sharp, D.N., A.J. Turberfield, and R.G. Denning, *Holographic photonic crystals with diamond symmetry.* Phys. Rev. B, **68**(20): p. -. 2003.

[44] Joannopoulos, J.D., *Self-assembly lights up.* Nature, **414**(6861): p. 257-258. 2001.

[45] Maldovan, M. and E.L. Thomas, *Diamond-structured photonic crystals.* Nature Materials, **3**(9): p. 593-600. 2004.

[46] Takahashi, S., et al., *Direct creation of three-dimensional photonic crystals by a top-down approach.* Nature Materials, **8**(9): p. 721-725. 2009.

[47] Tetreault, N., et al., *New route to three-dimensional photonic bandgap materials: Silicon double inversion of polymer templates.* Advanced Materials, **18**(4): p. 457-+. 2006.

[48] Yang, S., et al., *Creating periodic three-dimensional structures by multibeam interference of visible laser.* Chemistry of Materials, **14**(7): p. 2831-+. 2002.

[49] Xu, D., et al., *Holographic fabrication of diamondlike photonic crystal template using two-dimensional diffractive optical elements.* Applied Physics Letters, **93**(3): p. -. 2008.

[50] Lin, Y., P.R. Herman, and E.L. Abolghasemi, *Proposed single-exposure holographic fabrication of microsphere-type photonic crystals through phase-mask techniques.* J. Appl. Phys., **97**(9): p. -. 2005.

[51] Bita, I., et al., *Large-area 3D nanostructures with octagonal quasicrystalline symmetry via phase-mask lithography.* Advanced Materials, **19**(10): p. 1403-+. 2007.

[52] Wu, L.J., et al., *Fabrication of large area two- and three-dimensional polymer photonic crystals using single refracting prism holographic lithography.* Applied Physics Letters, **86**(24): p. -. 2005.

[53] Chen, J.Q., et al., *Holographic three-dimensional polymeric photonic crystals operating in the 1550 nm window.* Applied Physics Letters, **90**(9): p. -. 2007.

[54] Miklyaev, Y.V., et al., *Three-dimensional face-centered-cubic photonic crystal templates by laser holography: fabrication, optical characterization, and band-structure calculations.* Applied Physics Letters, **82**(8): p. 1284-1286. 2003.

[55] Hattori, T., et al., *Photonic Dispersion-Relation in a One-Dimensional Quasi-Crystal.* Physical Review B, **50**(6): p. 4220-4223. 1994.

[56] Jiang, H.J., et al., *Single-step fabrication of diffraction gratings on hybrid sol-gel glass using holographic interference lithography.* Optics Communications, **185**(1-3): p. 19-24. 2000.

[57] Wikipedia, *Fiber Bragg grating.*

[58] Hill, K.O. and G. Meltz, *Fiber Bragg grating technology fundamentals and overview.* Journal of Lightwave Technology, **15**(8): p. 1263-1276. 1997.

[59] Hill, K.O., et al., *Bragg Gratings Fabricated in Monomode Photosensitive Optical-Fiber by Uv Exposure through a Phase Mask (Vol 62, Pg 1035, 1993).* Applied Physics Letters, **63**(3): p. 424-424. 1993.

[60] Wikipedia, *Tablot effect.*

[61] Moon, J.H., J. Ford, and S. Yang, *Fabricating three-dimensional polymeric photonic structures by multi-beam interference lithography.* Polymers for Advanced Technologies, **17**(2): p. 83-93. 2006.

[62] Chan, T.Y.M., O. Toader, and S. John, *Photonic band-gap formation by optical-phase-mask lithography.* Physical Review E, **73**(4): p. -. 2006.

[63] Chanda, D. and P.R. Herman, *Phase tunable multilevel diffractive optical element based single laser exposure fabrication of three-dimensional photonic crystal templates.* Applied Physics Letters, **91**(6): p. -. 2007.

[64] Sutherland, R.L., et al., *Switchable orthorhombic F photonic crystals formed by holographic polymerization-induced phase separation of liquid crystal.* Optics Express, **10**(20): p. 1074-1082. 2002.

[65] Xu, D. and G.G. Xiong, *Transmission spectra investigation on tunable bandgap of liquid crystal infiltrated photonic crystal.* Journal of Materials Science, **39**(2): p. 679-681. 2004.

[66] Y. Lin, D.R., Z. poole and K. P. Chen, *Five-beam interference pattern controlled through phases and wavevectors for diamondlike photonic crystal.* Appl. Optics, **45**: p. 7971. 2006.

[67] Lorenz, H., et al., *SU-8: a low-cost negative resist for MEMS.* Journal of Micromechanics and Microengineering, **7**(3): p. 121-124. 1997.

[68] Agirregabiria, M., et al., *Fabrication of SU-8 multilayer microstructures based on successive CMOS compatible adhesive bonding and releasing steps.* Lab on a Chip, **5**(5): p. 545-552. 2005.

[69] Toader, O., T.Y.M. Chan, and S. John, *Diamond photonic band gap synthesis by umbrella holographic lithography.* Applied Physics Letters, **89**(10): p. -. 2006.

[70] Wijnhoven, J.E.G.J. and W.L. Vos, *Preparation of photonic crystals made of air spheres in titania.* Science, **281**(5378): p. 802-804. 1998.

[71] Sigalas, M.M., et al., *Metallic Photonic Band-Gap Materials.* Physical Review B, **52**(16): p. 11744-11751. 1995.

[72] Ledermann, A., et al., *Three-dimensional silicon inverse photonic quasicrystals for infrared wavelengths.* Nature Materials, **5**(12): p. 942-945. 2006.

[73] Man, W.N., et al., *Experimental measurement of the photonic properties of icosahedral quasicrystals.* Nature, **436**(7053): p. 993-996. 2005.

[74] Gorkhali, S.P., J. Qi, and G.P. Crawford, *Electrically switchable mesoscale Penrose quasicrystal structure.* Applied Physics Letters, **86**(1): p. -. 2005.

[75] Wang, X., et al., *Large-area two-dimensional mesoscale quasi-crystals.* Advanced Materials, **15**(18): p. 1526-+. 2003.

[76] Wang, X., et al., *Realization of optical periodic quasicrystals using holographic lithography.* Applied Physics Letters, **88**(5): p. -. 2006.

[77] Tam, W.Y., *Icosahedral quasicrystals by optical interference holography.* Applied Physics Letters, **89**(25): p. -. 2006.

[78] Xu, J., et al., *Icosahedral quasicrystals for visible wavelengths by optical interference holography.* Optics Express, **15**(7): p. 4287-4295. 2007.

[79] D. Shechtman, I.B., D. Gratias and J. W. Cahn, *Metallic phase with long range orientational order and no translational symmetry.* Phys. Rev. Lett., **53**(20): p. 1951-1953. 1984.

[80] Steinhardt, D.L.a.P.J., *Quasicrystal: a new class of ordered structures.* Phys. Rev. Lett., **53**(26): p. 2477-2480. 1984.

[81] Sun, H.B., et al., *Microcavities in polymeric photonic crystals.* Applied Physics Letters, **79**(1): p. 1-3. 2001.

[82] Vekris, E., et al., *Buried linear extrinsic defects in colloidal photonic crystals.* Advanced Materials, **17**(10): p. 1269-+. 2005.

[83] Pruzinsky, S.A. and P.V. Braun, *Fabrication and characterization of two-photon polymerized features in colloidal crystals.* Advanced Functional Materials, **15**(12): p. 1995-2004. 2005.

[84] Jun, Y., C.A. Leatherdale, and D.J. Norris, *Tailoring air defects in self-assembled photonic bandgap crystals.* Advanced Materials, **17**(15): p. 1908-+. 2005.

[85] Meisel, D.C., et al., *Shrinkage precompensation of holographic three-dimensional photonic-crystal templates.* Advanced Materials, **18**(22): p. 2964-+. 2006.